DIRECT NUMERICAL SIMULATION OF TWO-PHASE STRATIFIED FLOWS IN THE PRIMARY COOLANT OF A NUCLEAR REACTOR

A MSc. Thesis report

in partial fulfillment of the requirements for the degree of
Master of Science
in Applied Mathematics (COSSE)
at the Delft University of Technology,
to be defended on November 17th, 2021 at 09:00

by

Gopalan Gopalan Jayashankar

Student Number:	5374766	
Project Duration:	November,2020 – November, 2021	
Thesis Committee :	Prof.dr.ir. C.Vuik	Supervisor, TU Delft
	Prof.dr.ir. D.Toshniwal	Supervisor, TU Delft
	Dr.ir. E.M.A.Frederix	Supervisor, NRG
	Prof.dr. H.M. Schuttelaars	External Committee, TU Delft

TU Delft Delft University of Technology

NRG

CONTENTS

SUMMARY

Multiphase flows are very common in many Nuclear engineering applications. During high pressurized conditions there are possibilities of high thermal loads on the pressure vessel, leading to pipe ruptures. As part of breakdown measures, the emergency core cooling system is activated and the coolant is mixed with the fluid in the cold leg, giving rise to multiphase turbulent flow. These regimes can comprise of large scale interfaces, leading to stratified flows. These postulated accidents or events need to be identified and understood to improve nuclear reactor safety. Computational fluid dynamics can serve as an excellent tool to model these scenarios, contributes towards reactor safety. Coarse models which are widely used in industries such as RANS are known to over-predict turbulent producing unphysical gradients. Thus the turbulent mass and momentum are not yet fully understood. Using high resolution tools such as Direct Numerical Simulations (DNS), can potentially avoid these over-prediction and could model these large scale interfaces accurately. As a long term goal, the data sets generated from these simulations can be used to train such coarse models or simply support for validation.

Placing the focus on a configuration where two fluids are in a stratified scenario, this graduation thesis will show a systematic approach towards the development and modelling of air and water moving in both co-current and counter-current direction, wherein simulations are performed in RK-Basilisk. Primarily, the work starts with studying a single phase turbulent channel flow to form a basis of understanding of concepts and code. The model of [31], who use realistic properties of air-water is chosen to be implemented in RK-Basilisk. It is realised that, implementing this is in RK-Basilisk is not straightforward and thus the constraints are identified and a general mathematical framework is developed to resolve this.

One of the main objectives in this thesis is to model and understand the turbulent behaviour near the interface of both air and water. To do so, the physical mechanisms which govern the generation and decay of turbulence called the *TKE Budgets* is studied by modelling the individual terms that complete it. The budgets are modelled and validated against [31]. Interesting conclusions are drawn which depict the trends of budget terms and the kinetic energy, giving a good picture of the underlying interfacial turbulent mechanisms. The same mathematical framework, along with some additional modelling lead to an extension of this study to counter-current flows, wherein another set of conclusions are drawn.

PREFACE

Thank you for showing interest and taking the time to read my project. Somehow, this has been the largest work that I have put through. I feel very fortunate to have worked on something that I wanted to, for a long time. I would like to thank Dr.Kees Vuik (TU Delft), Dr.Reinhard Nabben (TU Berlin) and Dr.Michael Hanke (KTH) for accepting me into to this Masters and showing me the door to the world of Applied Mathematics. It was quite a hard transition from Mechanical Engineering, but I found my way through their invaluable guidance.

My research on this work of turbulent multiphase flows started approximately 9 months ago at the Reactor Analyses and Operational Support (RAS) team at The Nuclear Research and Consultancy Group (NRG) at Petten. I would like to thank my manager Ed Komen who gave me this opportunity to intern within a very friendly team. Throughout my work, I had invaluable guidance from my supervisors Kees Vuik and Deepesh Toshniwal at TU Delft. Healthy discussions and their constructive criticism motivated me to always do better. I would be failing if I don't thank my daily supervisor and mentor Edo Frederix. I would like to extend my heartfelt gratitude towards him for inspiring me, guiding me through all difficulties that I faced at times.

I am very proud of the COSSE/Cauchy/Cozy friends I have made in these two years in Berlin and Delft. I would also like to thank my friends back at home for giving me the emotional support I needed and for keeping me sane, despite the distance.

Maybe this is a bit unconventional, but I am proud of myself to have come this far. I have never given myself the credit that I deserved. Although this work wouldn't be perfection, I never thought I was able to do what I did. I am very happy to have learnt and gained so much experience from working on this thesis. I would like to acknowledge that right from this moment.

Last but not the least, I am eternally thankful to 'Ma' and 'Pa' for the love and support they have showed me. Despite having a little idea of what I was doing, they never stopped encouraging me and always asked me to keep my head up. I owe it all to them.

Gopalan Gopalan Jayashankar
Delft, November 2021.

1

INTRODUCTION

1.1. COMPUTATIONAL FLUID DYNAMICS

Computational Fluid Dynamics or CFD is the analysis of systems involving fluid flow, heat transfer and associated phenomena by means of a computer based simulation [57]. This approach, of solving the physics of fluids with the help of a computer, has proved to be an efficient way to tackle complex flow phenomena. The developer/user could easily play around with the code to alter or infer different results according to the requirements. Moreover, it has proved worthy to have reduced lead times and cost cutting when it comes to research and development. Often, these revolve around the numerical algorithms, modelling and implementation techniques to solve flow problems. The two equations of conservation of momentum and continuity are considered to be the most important equations of fluid dynamics. And they (in conservative form) are -

$$\frac{\partial}{\partial t}(\rho \mathbf{u}) + \nabla \cdot (\rho \mathbf{u} \otimes \mathbf{u}) = -\nabla p + \nabla \cdot \boldsymbol{\tau} + \rho \mathbf{g} \tag{1.1}$$

and

$$\frac{\partial \rho}{\partial t} + \nabla \cdot (\rho \mathbf{u}) = 0$$

where, ρ is the density of the fluid, $\mathbf{u}$ is the fluid velocity vector in $\mathbb{R}^n$, p is the pressure, τ is the stress tensor and finally, t being the time. To simplify these equations, we need to make quite a few assumptions and consider few properties. For Newtonian fluids, Incompressible flows, the equations are -

$$\frac{\partial \rho \mathbf{u}}{\partial t} + (\rho \mathbf{u} \cdot \nabla \mathbf{u}) = -\nabla p + \mu \nabla^2 \mathbf{u} + \rho \mathbf{f} \tag{1.2}$$

and

$$\nabla \cdot \mathbf{u} = 0$$

1

Which are essentially the Incompressible Navier-Stokes equation which would be the primary partial differential equation aimed to tackle in this thesis. But, it's not too hard to see that these equations talk about Newtons second law and mass conservation which gives rise to an initial boundary value problem. Each of the terms are -

- $\frac{\partial \rho \mathbf{u}}{\partial t}$ talks about the rate of change of velocity with respect to time
- $(\mathbf{u} \cdot \nabla \mathbf{u})$ is the inertial acceleration in the fluid
- $-\nabla p$ is the pressure forces
- $\mu \nabla^2 \mathbf{u}$ are the viscous forces
- $\rho \mathbf{f}$ are the external body forces. This can be $\mathbf{g}$ i.e,$(0, 0, \mathbf{g})$ in case there are no external forces but just gravity.

Although these equations characterize the role and the importance of each and every term, it is also very interesting to interpret these equations in a different way. These equations, in dimensionless form give rise to different dimensionless parameters (if we consider to make few assumptions) which can be readily be interpreted and linked to the physical phenomena occurring in the flow. Moreover, these dimensionless parameters give us an idea for scaling the model appropriately so that it can give a bigger picture for predicting the performance in large scale [24]. Few notable dimensionless parameters derived from the non-dimensionalisation of Navier-Stokes are -

- Reynold's Number, Re = $\frac{\rho U L}{\mu}$
- Froude Number, Fr = $\frac{U^2}{gL}$

Re talks about the ratio of inertial and viscous forces, Fr talks about the ratio of inertial and gravitational forces. Another interesting dimensionless number is the Weber Number, We = $\frac{\rho U^2 L}{\gamma}$ and is the ratio of inertial forces and surface tension.

These dimensionless parameters helps us to understand the contribution of each of the terms since these are ratios of different forces on the fluid. For example, if we were to examine the Reynolds's number carefully, it could be easy to interpret that for a flow with low Re (Re $\ll 1$), the viscous forces would be the most dominating and for a flow with high Re (Re $\gg 1$), the inertial forces would be dominating. As a starting point, this could be interesting to predict whether the flow would enhance mixing characteristics or would be diffusive in nature.

Now that we know what to solve, it is obviously necessary to think about how to solve these equations. A general solution to the Navier-Stokes is limited to the case of two dimensions and is not yet extended to a three dimensional setting. Instead, it could be a nice idea to solve them in a computer with numerical algorithm. We also need to consider where and when exactly (at different time steps) these equations are to be solved. Hence, it is also really important to choose the spatial and temporal discretization wisely as this defines how accurate the solution is in space and time.

For the choice of spatial discretization, some of the most common techniques are finite differences, finite element method, finite volume method and spectral methods. Much information could be extracted if the problem is solved on more number of finite cells in the domain. But it is not practically possible to solve the equations on each and every single point. Instead, we try to maximize and refine the mesh quality in the region of interest.

For the choice of temporal discretization, there are wide class of algorithms. Explicit and implicit solvers, where the discretized equations are integrated in time in either ways. But the implicit solvers have always proved to be very efficient and unconditionally stable. However, these are expensive to compute and also difficult to implement[59][63].

But to solve the Navier Stokes, it is essential to consider how the pressure-velocity coupling is solved. The system can be either can be solved together (Eg, Crank-Nicholson) which would make it difficult, or decoupled to solve the pressure and velocity separately (Eg, Chorin, SIMPLE, SIMPLEC/R, PISO - considering we have a staggered grid configuration)[59][63][57]. Sometimes, different schemes like Crank-Nicholson and Adams-Bashforth schemes could be implemented for the viscous and convective terms respectively which are both second order accurate[31].

After the non linear PDE is discretized with one of the above mentioned spatial discretization method, these reduced to a linear system of matrix-vector equations which could be solved with either direct or iterative Methods. However a class of iterative methods like jacobi, gauss-seidel and conjugate gradient methods have proved to achieve faster convergence rates.

In order to solve this system more accurately and faster, high performance computing techniques can also be implemented. These entire domain is partitioned into a number of sub-domains and each of the sub-domains are solved on a specific process. Owing to the capabilities of DNS to resolve all scales of turbulence, more effort is gone to modelling and developing meshes according to the smallest scales. Hence state of the art HPC techniques become necessary for efficient and fast calculations[10].

After solving the system of equations, we could use various platforms (ParaView, ANSYS Post etc) to visualise the obtained results and infer results on various parameters .

This on whole, is the process of CFD. This entire process could be performed in open source CFD packages/solvers or commercial CFD softwares. Open source CFD packages provide the freedom to manipulate the underlying code so that we could play around but however this requires much effort and knowledge to set up the problem. Some examples of these open source CFD softwares are OpenFOAM[42], Basilisk[2], PHASTA [10] etc.

1

1.2. MULTIPHASE FLOWS

As we can find as much as different categories of flows, one interesting classification would be to find out the different phases existing in the domain of interest and how the behaviour and the coupling would look like. The field could contain fluids of the different phase with different thermal conditions (adiabatic and diabatic flows - condensation and vaporization). Next, we could also think of it as two different fluids, but of the same state (oil and water). These, often are also referred to as multifluids. As far as the scope of this project is concerned, the case of gas-liquid flow is simulated. With this, it could be easy to define what multiphase flows are with the idea built. Multiphase characterizes situations where several different phases - liquids, gases, solids are flowing simultaneously[61]. A single phase flow would be somewhat easier to model and implement whereas more effort needs to go in for the case of multiphase flows (interface modelling etc).

In the bigger picture, two main topologies of multiphase flows are - dispersed and stratified Flows. Dispersed flows are where one of the phases is completely dispersed (enclosed by, loosely speaking) another phase. One simple example for this would be the case of formation of steam bubbles when boiling water. In the same fashion, if a long elongated vertical duct is considered, as time evolves, these bubbles would gather up and lead to form Taylor bubbles and this phenomenon is widely existent in many industrial applications. On the other side, *Stratified* (segregated, separated) flows are where, different phases are separated due to the difference in the densities and are arranged in a parallel fashion due to the effect of gravity. For simplicity, we could think of a long horizontal duct carrying steam and water, which are stratified due to the density difference.

To get a visual understanding, Figure 1.1 shows different types flow regimes for a horizontal duct which are also explained in the following paragraph [61]. Yellow being one phase and blue, the other.

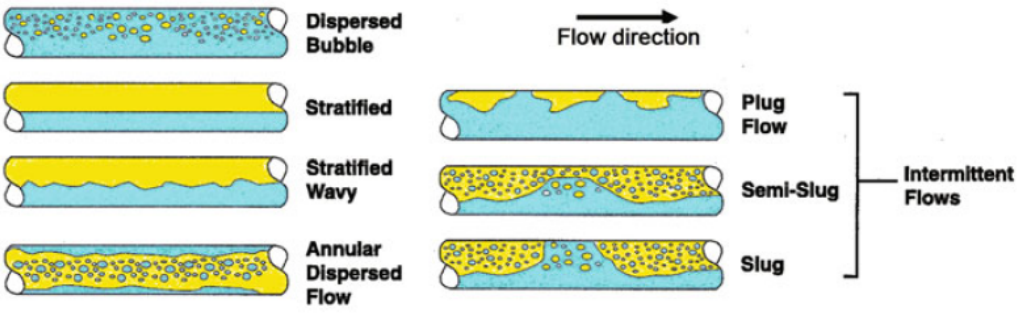

Figure 1.1: Types of Horizontal two-phase flows [61]

Bubbly flows are dispersed in the liquid in a continuous fashion and their concentration tend to be higher in the upper part of the tube and the factor of gravity is not so impor-

tant at higher velocities.

Annular flows are generally existent when the gas-velocity is much higher and the heavier phase tend to form a film around the edges of the pipe with varying thickness.

Plug Flow are existent in low and moderate flow rates and form a discontinuous pattern of the lighter phase on the upper part of the duct.

With the same configuration, if the velocity of the lighter phase if increased, visible slugs are formed and contains some small bubbles which traverse along the pipe. The flow is somewhat chaotic and the interface is generally hard to track.

Stratified Flows occurs when two fluids are separated with a higher dense liquid on the bottom and the liquid which is less dense stratifies at the top. The interface between the two faces might be flat or wavy. When the velocity of either of the two phases is increased, this give rise to the wavy interface of varying amplitudes. In [6], Open-FOAM CFD simulations are carried out for different type of multiphase flows (Stratified, Wavy, Slug, Plug) and it is found that, the results are in good agreement with the experimental data.

In this thesis, all of the work done would be for a configuration of two-phase (gas - liquid) stratified flow. Gas-liquid stratified flows exist in most of the industrial applications. Vapour generation systems in conventional and nuclear Power plants make use of this configure for the production and transport of steam for various parts across the Power plant. Most of the process technology applications such as chemical production, food production, oil and gas production require this type of configuration for different aspects. Pipelines in large factories such as in petrochemical industries, process plants and also in power generation require this kind of flow regime.

With these applications to the configuration, there comes a necessity to predict and model the flow beforehand. For example, in a stratified flow if the interface is not flat anymore, large wave amplitudes could have different effects on both fluids. The wavy interface could have added effects to the turbulent field, and also maybe alter momentum exchange between the two fluids[14].

In Nuclear Power plants, when there is a rupture in the main reactor pressure vessel, the primary coolant may leak into the reactor hall. This is often referred to as Loss of Coolant Accident (LOCA). During these scenarios, the coolant may mix with the fluid inside the reactor hall which is already hot due to high pressure and this leads to a rapid and more turbulent mixing of the fluids. With the already existing steam which (maybe) flows in the opposite direction, this gives rise to a stratified flow configuration. The difference in the properties makes the entire configuration complex leads to heat, mass and momentum transfer which not yet fully understood. This requires us to develop some (mathematical) models to ensure that the complex physics of the turbulent stratified flows are fully understood.

1

2

LITERATURE STUDY

2.1. TURBULENCE

Most of the flows which we encounter in real life or in most of the engineering applications are not smooth i.e, they are not always laminar. Turbulent flows are unavoidable, hence this is not only of theoretical interest. There is a point where the flow is not laminar anymore and it becomes unsteady and chaotic. This unsteadiness gives rise to random fluctuations to each of the flow properties which vary in time. Due to the fluctuations, the conventional equations are altered and gives rise to additional stresses in the flow[54].

Above a certain Reynolds number, i.e, a critical Re (depending on internal/external flows), the flow becomes unstable and the flow properties vary in a random way with respect to time. This random nature makes the economical prediction of flow properties close to impossible. Instead, a stochastic description is made. The time varying velocity is decomposed into a mean and a fluctuating component.

$$u(t) = U + u'(t) \tag{2.1}$$

This is called as the *Reynolds decomposition*. So, a complete description of a turbulent flow is given mean properties (U, V, W, P) and statistical properties (u', v', w', p').

Good visualisation of turbulent motions reveals a picture of turbulent eddies. Eddies, also called as vortices are structures of a fluid continuum swirling around due to the turbulent nature of a flow. Due to the eddying nature of flow, random particles of the fluid which are separated by some distance are also bought together/closer which as a part of effective mixing and vortex stretching. As a consequence, the diffusion coefficient is high and enhances mixing. Due to the presence of mean velocity gradients, different layers are sheared at different rates and leads to distortion of the existing eddies. The eddies then break-up/stretched into smaller eddies and consequently, the energy from the big eddies are transferred to the smaller ones in a progressive nature and this is called energy

cascade.

The small/(sub-) micro scales eddies are dominated by the effect of viscosity. Hence a complete depiction of length, time and velocity can be given by the so called Kolmogorov Microscales and they are called the Kolmogorov time, length and velocity. The larger or the largest eddies can be characterised by the Integral scales. Unlike Kolmogorov scales, these scales strongly depend of the domain geometry and boundary conditions of the model, hence they are anisotropic. Since the turbulent quantities, in the given neighborhood are (maybe) not independent of each other, these scales can be computed from the two point correlation function in space or time [54].

2.1.1. DESCRIPTORS OF TURBULENT FLOWS

TIME AVERAGE OR MEAN

The Reynolds decomposition for a flow quantity, $\varphi(t)$, can be given by

$$\varphi(t) = \Phi + \varphi'(t)$$

The mean Φ is defined as,

$$\Phi = \frac{1}{\Delta t}\int_0^{\Delta t} \varphi(t)\,dt$$

This definition makes sense if the flow is steady and does not change over time. But for time varying flows, the mean of the flow at time t, is considered to be the average of instantaneous value over a number of similar experiments, i.e, the so called ensemble average. Theoretically, it makes sense if we consider $\Delta t \to \infty$, but the equation gives a meaningful depiction for time averaged quantity if $\Delta t >$ the smallest time scales.

VARIANCE, R.M.S AND TKE

Variance and r.m.s values tell us about the spread of the fluctuations over the mean flow.

$$\overline{(\varphi')^2} = \frac{1}{\Delta t}\int_0^{\Delta t} (\varphi')^2\,dt$$

$$\varphi_{rms} = \sqrt{\overline{(\varphi')^2}} = \sqrt{\frac{1}{\Delta t}\int_0^{\Delta t} (\varphi')^2\,dt}$$

The r.m.s fluctuations are easily measured and tell us the average magnitude of the fluctuations. In particular, when we work with the Navier Stokes equations, the variance of velocity components $\overline{u'^2}, \overline{v'^2}, \overline{w'^2}$ are proportional to the momentum fluxes and cause stresses which are experienced additionally by the turbulent flow. One half of the sum of these variances, gives a rise to the **Kinetic Energy (TKE)** which is the amount of kinetic energy present per unit mass k a given point [57] and is given by

$$k = \frac{1}{2}(\overline{u'^2} + \overline{v'^2} + \overline{w'^2})$$

2.1.2. TURBULENCE IN WALL BOUNDED CHANNEL FLOWS

Since this thesis would be tackling the flow inside a channel, it would be a good idea to discuss about the (turbulent) Boundary layer and also the structures. A Reynolds Number relative to the distance from the wall, could tell how important the inertial/viscous forces are as a function of distance from the wall. $Re_y = \frac{Uy}{\nu}$, based on the distance 'y' from the wall. Its is now evident that, for points far away from the wall, the inertial forces would be the most dominating and for points close to the wall, the viscous forces would be dominating. There are also a point where the forces are equal ($Re_y = 1$). From this distance, to the wall the viscous forces dominate and on the other side, the inertial forces dominate. Thus mean flow velocity could be too depicted as a function of 'y', $U = f(y, \rho, \mu, \tau_w)$. With this, we could get a new dimensionless parameter u^+, defined as

$$u^+ = \frac{U}{u_\tau} = f\left(\frac{\rho u_\tau y}{\mu}\right) = f(y^+) \tag{2.2}$$

where $u_\tau = \frac{\sqrt{\tau_w}}{\rho}$ is the friction velocity. Far from the wall, there is a point up to which the are additional viscous effects apart from the viscosity itself and this is experienced by the wall shear stress and can be characterized by u_τ. The appropriate length scale where this is effective is called the *turbulent boundary layer*, δ. [54]. This gives us the rough estimate of the Dimensionless Turbulent velocity u^+ from the wall at a distance y^+. With this, it can be interesting to classify the regions of the flow based on law of the wall. There are three distinct regions within which each of the inertial and the viscous forces are important (i.e, region specific dominant force) called the linear or the viscous sub-layer, log-law layer and outer layer.

LINEAR OR VISCOUS SUB-LAYER

As we all know, at the wall, the shear stress at the wall is effectively zero. Hence, motion due to turbulent eddies should also "stop" at the wall, for a no-slip (i.e, U = 0) condition. But close to the wall, i.e, $y^+ < 5$, it is seen that the viscous stresses are almost equal to the wall shear τ and is constant. With this, we could establish a linear relationship between the mean velocity and the shear.

$$\tau(y) = \mu \frac{\partial U}{\partial y} \approx \tau_w$$

Hence,

$$U = \frac{\tau_w y}{\mu}$$

With this, we can establish that, $u^+ = y^+$. Because of this linear relationship, between the distance and the velocity, this is known as linear or viscous-sub layer.

LOG-LAW LAYER

From the viscous sub-layer, if we move away from the wall, there is a region ($30 < y^+ < 500$) where the viscous and the inertial effects are both important. Considering the mean flow is parallel to the wall, the turbulent velocity varies logarithmically as a function of

wall distance. The velocity follows the logarithmic curve and hence it is called as the log-law layer.

$$u^+ = \frac{1}{\kappa} ln(y^+) + B = \frac{1}{\kappa} ln(Ey^+) \tag{2.3}$$

where, κ is the Von Karman constant, $\kappa \approx 0.4$

OUTER LAYER

This is the region far away from the wall. Consequently, the pressure gradient and convective terms are more dominant and free from the effects of viscosity. This is sometimes referred to as the law of the wake layer.
By using these wall functions, we can model the flow near the wall. This becomes important as we need to study the behaviour near the wall. If the mesh is not well resolved near the wall, a high Reynolds Number flow would result in inaccuracies without modelling near wall characteristics. With well implemented wall functions and resolved mesh near walls, the turbulent boundary layer is well captured and the near wall characteristics are studied better.

2.1.3. TURBULENCE MODELS

Upon time averaging for the momentum equations, it results in :

$$\frac{\partial U}{\partial t} + \mathbf{U_i} \frac{\partial U_i}{\partial x_j} = -\frac{\partial P}{\partial x_i} + \nu \frac{\partial}{\partial x_j} \left(\frac{\partial U_i}{\partial x_i} \right) + \rho \mathbf{f} - \frac{\partial \overline{u_i' u_j'}}{\partial x_j} \tag{2.4}$$

The last term new and is called as the *Reynolds Stress tensor*, R_{ij}. The diagonal components of this tensor gives us the additional normal stresses experienced by the fluid and the other off-diagonal components which has the second moments of velocities tell us the additional shear stresses acting on the fluid. These turbulent shear stresses are very large when compared to the viscous shear stresses experienced by the fluid. Due to the convective transport of eddies, there is a net momentum exchange, wherein a fast moving shear layer is decelerated, hence the fluid experiences additional turbulent shear stresses, which is eventually characterized by the Reynolds stress tensor, R_{ij}. Due to these additional unknowns, the NSE becomes a closure problem and therefore requires additional modelling effort in order to full resolve the fluid flow.

While Direct Numerical Simulations and Large Eddy Simulations provide satisfactory results [27], they become high unsuited because of the realistic macroscopic industrial applications mainly due to the high computational cost. Hence most of the turbulent flows come down to coarse models such as RANS.

The problem with RANS is that, they produce unphysical results near interface of stratified flows [12] [34]. RANS models lose the ability to predict high velocity gradients near interface. In [47], the author has simulated a two equation model for a flat interface and reported some uncertainty. [48] used the $k-\omega$ model the same scenario and indicated that the interfacial conditions need to further studied to implement in such a model in order to understand it better for a wavy flow. The main discrepancy is that turbulent

characteristics is over predicted near interface region. Hence [9] suggested to introduce a damping function close to the interface region and the results were pretty satisfactory. This was further studied in [27] as well and reported to produce results close to DNS data.

However, to stick to the scope of this thesis neither of the two approaches are taken, but the entire problem is resolved by a Direct Numerical Simulation (DNS). The Navier-Stokes equation directly solved without accounting for any filtered functions or time averaged flow quantities. The main idea of RANS or LES was to model the large and small scale eddies of various length and time scales without having to put the major emphasis on grid resolution to be the best. Such an effort comes along in DNS[38]. Due to the absence of modelling and direct computing, the spatial grids have to be resolved to small scales of turbulence and small time steps in order to capture the smallest eddies and the fastest fluctuations.

2.1.4. COMPUTATIONAL COST OF DNS

By the virtue of turbulence, it's effects are over all length and time scales. For high Re, the inertial terms become more dominant and hence the convection in the flow becomes dominant which mainly transports the momentum from large eddies. In this case, the smallest scale should be solved until the viscous forces dominate.

The smallest scale, as indicated previously is the Kolmogorov Scale. The length scale is given by

$$\eta = (\nu^3/\epsilon)^{\frac{1}{4}}$$

and

$$\tau_\eta = (\nu/\epsilon)^{\frac{1}{2}}$$

where, ν is the viscosity and ϵ is the dissipation rate. Contrasting to small scales, the biggest scales, "Integral Scales" are represented by L and τ_0 as length and time scales. The ratio of the smallest to the largest length scales could be represented as

$$\frac{\eta}{L} = (Re)^{-\frac{3}{4}}$$

Hence, in other words, the number of grid points required per integral scales to solve all kolmogorov scales would be [60]

$$N_h = \frac{L}{\eta} \approx Re^{\frac{3}{4}}$$

and the required time steps would be N_t as this could be the Kolmogorov scale. So the total cost of computing the DNS would be (in 3 dimensions)

$$N_h \cdot N_t = Re^{\frac{9}{4}} \tag{2.5}$$

It can be verified that for a relatively small Reynolds number, the computational cost would be very high. Hence, simulating it for realistic industrial applications would not be practical. Hence, it makes sense to simulate it for rather simpler situations and emphasize more on developing more coarse models based on DNS data.

2.2. LITERATURE SURVEY OF STRATIFIED FLOWS

In this chapter, the state of the art simulations of stratified flows are investigated. A large collection of resources helps in identifying the evolution and developments of the numerical simulations over the years. An advantage of this study would help to get a bigger picture of what the overall aspects of these simulation and experiments are. A successful identification of the bigger picture would help to zoom in or look into the specifics which essentially would drive us towards the goal of this literature study, to formulation a successful research question.

2.2.1. DIRECT NUMERICAL SIMULATIONS

Direct numerical simulations of turbulent flows have been of major interest for a few decades now. Especially, when it comes to simulations in the field on nuclear engineering, turbulent flows are inherent. In particular, multiphase flows are very common. For the case of single phase flows, results of the coarse models are satisfactory. But when multiphase flows are simulated using coarse models, especially for stratified flows, the results present unphysical gradients because of the non-stationary interface. Hence, at these situations direct numerical simulations would be the best to consult with, but at an expense of high computation costs.

SINGLE PHASE FLOWS

Since one of the tasks of the upcoming thesis is to validate the single-phase turbulent channel flow, it would be helpful to also review some literature based on the same. This could be considered as a first-step towards two-phase DNS, making it more approachable for the case of stratified flows. Many works have been carried out for the case of single phase turbulent flows. For example, in the review of Lahey Jr [26], direct numerical simulations have been performed in PHASTA which is based on the finite element method, for a horizontal channel flow. The velocity fields are in good accordance and also seem to obey the Law of the wall rule. The anisotropic nature of turbulence is also verified with the corresponding Reynolds stresses and the turbulence bursts are also shown which arises in the near wall region. In Kopparthy et al. [23], several coarse models such as, $k-\epsilon, k-\omega$, RSM and SA models have been implemented for the single phase turbulent flows for a diffusing horizontal column and it's seen that pressure and velocity fields could be predicted very well with the $k-\epsilon$ and RSM models. When it comes to two-phase stratified flows, it is reported that RSM models could predict well for low flow rates, but fails and gives deviating and unsatisfactory results when the flow rates are increased. Another interesting study of single phase channel flow has been carried out in Eggels et al. [8] using the finite volume method instead of the spectral method. The findings of this works compares the mean and r.m.s velocities and also Reynolds stresses with experimental data and were found to be agreeable.

Studies of Moser, Kim, and Mansour [40] have performed fully developed channel (turbulent) flow for three different shear based Reynolds number $Re_\tau = \frac{u_\tau \delta}{\nu}$, where u_τ is the shear based (frictional) velocity and δ being the half-channel distance. It was found that the Reynolds based effects (log-law behaviour, components of the TKE budgets etc) are

obeyed for 180≤ Re_τ ≤ 590 and for higher Re_τ, the behaviour is Reynolds-effect-free. A very well appreciated and known work in the field of turbulent flow for horizontal channel is of Kim, Moin, and Moser [17]. They have performed a DNS at a Re of 3300 for a horizontal box of dimensions 192 × 129× 160 points. For the choice of spatial discretization, spectral methods have been used. This method entails using Fourier series expansion in the stream-wise and span-wise directions and using Chebyshev polynomial expansion for the normal components. This stands arguably good in the case of turbulence because of the choice of higher order interpolation functions considered here over FDM (includes FVM) techniques. The general characteristics of turbulence were in good argument whereas the computed Reynolds stresses and vorticity fluctuations seemed to deviate from the experimental results in the near wall region. This work was further developed by Mansour, Kim, and Moin [36] where the data sets of the channel were derived from the previous work and the transport equation of Reynolds stresses and the dissipation rate of TKE were analysed for a low Re. The main conclusion drawn was that the terms of the budgets become more important in the near-wall region which is commonly argued to become less important away from the wall. In particular, the production terms of the TKE budget become more important close to the wall and the dissipation terms become equally pronounced away from the wall. Hence it would be of much importance to put attention to the near wall region when coarse models for the same are developed.

STRATIFIED FLOWS

One of the first works on the direct numerical simulation of two-phase stratified flows could be found in the literature of Riley et al. [46]. The stratification effects were varied by using different Froude numbers. For most of the computations performed, waves were formed for the varying Fr, hence having the induced wave effects on the flow. The simulations were performed in a relatively small grid of 32^3 points. A pseudo-spectral method was used to discretize the equations in a Fourier space. A leap-frog time integration scheme was used for convective terms whereas a Crank-Nicholson scheme was used for the diffusion terms. Limiting to the small computational domain, the Re was limited to 27.2 In a broad sense, the statistics in the normal directions seemed to be inhibiting whereas the statistics in the homogeneous directions seemed to be enhancing. Generally, it was also noticed that there was a decay in the dissipation of kinetic energy. The general notion of vortex-stretching in turbulent flows were also supported as the vorticity seemed to be decaying.

Counter-current Flow : A remarking research on this topic was carried out by the group of Lombardi, De Angelis, and Banerjee [32]. Simulations have been performed at different density ratios (indicating the dynamic coupling between the phases) for the setting of a counter-current flow where-in the interface was kept flat (corresponding to very high Weber number or high Surface Tension). The spatial length (non-dimensional) is represented as shear-based units and the normal extent of each of the phases are 170 shear based units each. No-shear i.e, a free-slip boundary condition has been employed at the outer boundaries whereas the fluids are coupled with the so called interfacial boundary conditions (continuity coupling of velocities and shear stresses, ensuring

momentum transfer). Periodic boundary conditions are applied in the homogeneous directions. A constant pressure gradient is applied in the to counter the effect of momentum losses at the interface due to friction. The complete Navier-Stokes along-with the interfacial boundary conditions are solved with the pseudo-spectral method (fourier expansions and chebyshev polynomials in the homogeneous and normal directions respectively)(Sengupta, Mashayek, and Jacobs [50]). A fractional step integration is used for the temporal discretization where-in one of the two interfacial boundary condition is solved in the first half and the next in the next half of the time step. An arbitrary Lagrangian-Eulerian boundary fitting method was used to solve the interface motion. This constitutes for solving the advection equation on an arbitrary mesh where each of the phases are coupled by the balance of continuity and shear.

Firstly, it was seen was seen that for the dynamic coupling far from unity, the interactions are decreased. The main inference drawn from this research was that, the gas-side sees the interface as a solid boundary due to the high shear imposed by the fluid on the gas side. Due to this, they exhibit turbulence behaviour similar to of wall characteristics, whereas this is not the same for the liquid side where it shows some high fluctuations and seemed to be more active. This is also supported by analysing the energy budgets. In the near interfacial region of the liquid side, the production and the dissipation terms are higher and lower than on the gas side, respectively, which seem to be unbalanced on the whole. Another main inference from the energy budget analysis about the turbulent diffusion. The diffusive nature was more pronounced at the interface for the liquid side and slightly away from the interface for the gas-side. A non-dimensional shear rate, $\tilde{S}$ shows that, for $\tilde{S} > 1$, low speed streaks appear (London [33]). Sweep events are found near interface and ejections far away from the interface. Near the interface, gas-liquid sweeps are found confirming high interfacial shear stress (high Reynolds stress production) and gas - liquid ejections are formed in the low shear regions (away from the interface)(De Angelis [7]Lam and Banerjee [28]). This leads to the formation of quasi stream-wise vortices between the regions of high and low shear and large vortices (few of them) are attached to the interface, pointing out that the interfaces are coupled.

A continuation of Lombardi, De Angelis, and Banerjee [32] was carried out in Fulgosi et al. [13] but with a free deformable interface and compared to an open-channel flow. One difference which was noted from Lombardi, De Angelis, and Banerjee [32] was, the r.m.s velocities initially have a non-zero value since the interface is not flat anymore. It was reported that the transport TKE budget revealed insignificant differences, only that it was slightly more pronounced than the open-channel case in the viscous sub layer region. Although, Reynolds stress budgets showed significant different in the direction normal to the interface. It was seen that the pressure diffusion makes turbulence more isotropic by lowering shear stresses. An auto-correlation function for the vorticity was maximum at the interface and reduces in the direction normal to it implying the very existence of vortical activities which might also enhance mixing characteristics.

Direct numerical simulations for a similar setting of Lombardi, De Angelis, and Banerjee [32] has been carried out in Hasegawa, Kasagi, and Hanazaki [15]. Similar results for

velocity profiles were shown and the difference between the behaviour of gas and the liquid side, given the degree of dynamic coupling between the two. Interestingly, it was shown that for different length ratios (of domain) for each of the phase, the distance between the streaks formed also varies, implying the interaction between the phases with same argument as above.

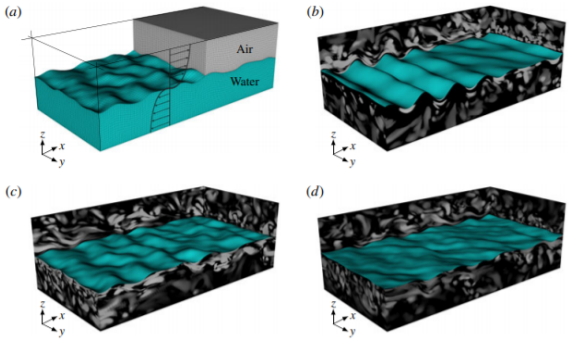

Figure 2.1: Counter-current flow setting for various stratification scenarios Zonta, Soldati, and Onorato [64]

A pioneer research as an extension to Lombardi, De Angelis, and Banerjee [32]Fulgosi et al. [13] was performed in Fulgosi et al. [14]. The full Navier-Stokes along-with the jump conditions (interfacial boundary conditions) were solved for a counter-current setting (for example Figure 2.1 d). Interestingly, neither of the Interface capturing nor the Interface tracking method were used, but a boundary(interface) fitting method. Boundary fitting method 'fits' the mesh according to the interface. Free slip boundary conditions were imposed on the outer boundary. The interfacial jump conditions (from the global mass, momentum and shear stress balances) were given as Fulgosi et al. [14]

$$\begin{aligned} \frac{1}{Re}((\tau_L-\tau_G)\cdot\mathbf{n})\cdot\mathbf{n}+\tilde{p}_G-\tilde{p}_L+\frac{1}{We}\nabla\cdot\mathbf{n}-\frac{1}{Fr}f=0 \\ ((\tau_G-\tau_L)\cdot\mathbf{n})\cdot\mathbf{t}_i=0 \quad i=1,2, \\ \tilde{\mathbf{u}}_G=\frac{1}{\mathscr{R}}\tilde{\mathbf{u}}_L \end{aligned} \tag{2.6}$$

where Re, We, Fr are the dimensionless numbers which were carefully chosen to stop the waves from breaking, τ and $\tilde{u}$ are the shear stress and the velocity respectively for a dynamic coupling of $\mathscr{R}$ = 29.9 (normal air-water density coupling ratio). These three together with

$$\frac{\partial f}{\partial t}+\tilde{\mathbf{u}}\cdot\nabla f=0 \tag{2.7}$$

represent the jump conditions and the advection of the interface using boundary-fitting method. A pseudo-spectral technique similar to Lombardi, De Angelis, and Banerjee [32]

was used for the spatial discretization (De Angelis [7]). The simulation was performed at a shear Re of 171. The computational domain for each of the gas and liquid phase was represented in wall units of 1074×537×171.

One of the main conclusions drawn was that the role of the deforming interface was to act like a dampener of the turbulent field in the region near interface. This was confirmed by less pronounced values of r.m.s velocities and the rate-of strain tensor. Although an extensive analysis about sweep-ejection events are not provided as in Lombardi, De Angelis, and Banerjee [32], it is argued that the deforming interface did not affect the orientation of quasi-streamwise vortices since there was not much change in the vorticity, ω_z. Studying the energy budget equations, especially for the Turbulent Kinetic Energy (TKE) budget given by,

$$\frac{Dk}{Dt} = \underbrace{-\overline{u_i u_j}\frac{\partial U_i}{\partial x_j}}_{\text{Production}} \underbrace{-\frac{1}{\rho}\frac{\partial}{\partial x_i}\overline{p u_i}}_{\text{Pressure Diffusion}} \underbrace{-\frac{1}{2}\frac{\partial}{\partial x_j}\overline{u_i u_i u_j}}_{\text{Turbulent Transport}} \underbrace{+\frac{1}{2}\nu\frac{\partial^2}{\partial x_j^2}\overline{u_i u_j}}_{\text{Viscous Diffusion}} \underbrace{-\nu\overline{\frac{\partial u_i}{\partial x_j}\frac{\partial u_i}{\partial x_j}}}_{\text{Dissipation}} \tag{2.8}$$

It revealed the similarity to the previous conclusion of general dampening of turbulent field. This argument emerged since the dissipation terms seemed to be lesser than the channel flow case (which this was validated against). Additionally, the Reynolds stress budgets (half trace of Equation 2.8) were also studied. It was seen that the pressure diffusion (source of energy and also re-distributive mechanisms) seemed to counter-balance the reduction in dissipation. The energy was redistributed from the normal components, thus reducing the turbulent production and promoting isotropy. Hence it was concluded that, the deforming nature of the interface dampens the turbulent field, reduced the dissipation thus making the near interface region less anisotropic. However away from the interface, the production and transport terms were more pronounced. Interestingly, it was also seen that, that the drag is reduced near the interface. This is due to the fact that, since energy is redistributed, there is essentially reduction in shear, making some components of the RST (Reynolds stress tensor) lower than of the channel flow case (which was compared against). Similar to Lombardi, De Angelis, and Banerjee [32]Fulgosi et al. [13], a non-dimensional shear rate built and the effective streak formation was also studied and non zero value of TKE at the interface confirmed the coupling mechanisms (momentum transfer etc.)

In Zonta, Soldati, and Onorato [64], a DNS was performed in a counter current setting to explore the influence of dynamics based on the dominance of We and Fr. The physical domain which is distorted, is mapped to a reference domain and the equations are solved using a pseudo-spectral method. It was noticed that, initially the growth of the waves were linear. Later in time, the wavy interface had some influence on the dynamics of the near interface region. For the ratios of $\frac{\sqrt{F}}{We} < 2$, the surface tension effects dominate and for ratios $\frac{\sqrt{F}}{We}$ >2, the gravity effects dominate due to exponential growth.

Co-current flow : In Liu et al. [31], a DNS of a gas-liquid co-current couette flow for a flat interface configuration was performed. The shear Re for water and air were set at 120 and 271 respectively. For the choice of spatial and temporal discretization, the same setting as of Lombardi, De Angelis, and Banerjee [32] was used. From the flow statistics, it was concluded that the gas side, perceives the (flat) interface as a solid wall. The water side boundary layer was found to be much thinner than the air side due to increasing turbulent transport near interface. TKE budget analysis revealed that, the peak values for production are attained near the interface when compared to the gas-side. Turbulent transport was enhanced by viscous diffusion. Apparently, the water side showed an increase in the dissipation of TKE which contrasting to Lombardi, De Angelis, and Banerjee [32]. Moreover, in the air-side the TKE is transported from bulk to the interface, whereas in the liquid side, TKE is transported from the interface to the bulk region which could be argued with the vortex dynamics across the interface.

Although quite a number of researches have reported on the turbulent characteristics of stratified flows and the influence of interface, there are very few which talk about the growth of the interface and how it affects the nearby region during it's growth. One such work would be of Lin et al. [30], where a DNS is performed for gas-liquid co-current flow at a $Re_* = 115$. Boundary conditions and the spatial discretization mimic Fulgosi et al. [13]Lombardi, De Angelis, and Banerjee [32]. A second order Runge-Kutta method was used for the time integration. It's seen that the wave evolve linearly initially but at later stages, the growth becomes exponential (Zonta, Soldati, and Onorato [64]Fernandino and Ytrehus [11]). When the surface waves were weak, the streaks observed were quite disoriented and when they grew strong, the streaks became more oriented. In a general sense, it was seen that for the air side, the changing wave effect did not have much influence as the water side did, for the turbulent fluctuations. The velocity variances are significantly changed in the horizontal and also the normal component in the near interface region as the waves start to build. The pressure fluctuations in the air side behaved differently for the period linear and exponential growth. Initially during the linear growth, the pressure fluctuations were due to the turbulent motion but at later stages (exponential growth) become waveform and move along-with surface waves (Zonta, Soldati, and Onorato [64]).

2.3. DISCUSSIONS BASED ON THE REVIEW

Author	Flow setting	Num meth	Interface geometry
Riley et al.[45]	n.a	Pseudo-spectral	n.a
Lombardi et al.[32]	Counter current	Pseudo-spectral	Flat
Lam et al.[28]	Counter current	Pseudo-spectral	Flat
Fulgosi et al.[13]	Counter current	Pseudo-spectral	Wavy
Fulgosi et al.[13]	Counter current	Pseudo-spectral	Wavy
Hasegawa et al.[15]	Counter current	Pseudo-spectral	Flat
Zonta et al.[64]	Counter current	Pseudo-spectral	Wavy
Liu et al.[31]	Co current	Pseudo-spectral,FDM	Flat
Lin et al.[30]	Co current	Pseudo-spectral	Wavy
Trontin et al.[55]	n.a	FVM-WENO	Decaying
Vincent et al.[58]	n.a	FVM-WENO	Decaying
Komori et al.[22]	Co Current	FDM	Wavy
Kurose et al.[25]	Co-Current	FDM	Wavy

Table 2.1: This table summarizes the different numerical schemes, flow setting and the interface geometry used in various simulations

Author	Interface model	Re_*	We	Fr	$\mathscr{R}=\frac{\rho_1}{\rho_2}$
Riley et al.[45]	n.a	27.2	n.a	3.65, 1.83	n.a
Lombardi et al.[32]	ALE,BFC	60.4	n.a	low	29.9,1,10
Lam et al.[28]	ALE,BFC	60.4	n.a	low	n.a
Fulgosi et al.[13]	ALE,BFC	171	5.3×10^{-3}	4.5×10^{-4}	29.9
Fulgosi et al.[14]	ALE,BFC	171	4.8×10^{-3}	8.7×10^{-4}	29.9
Hasegawa et al.[15]	ALE,BFC	300,150	n.a	low	841
Zonta et al.[64]	ALE,BFC	170	8.4×10^{-4}	2.9×10^{-6}	n.a
Liu et al.[31]	ALE,BFC	120,271	n.a	n.a	828
Lin et al.[30]	ALE,BFC	115	n.a	n.a	n.a
Trontin et al.[55]	LS	93	n.a	n.a	1
Vincent et al.[58]	LS	n.a	0.05,2,110	n.a	1
Komori et al.[22]	ALE,BFC	210	5.6	n.a	n.a
Kurose et al.[25]	ALE,BFC	380	9948	116	n.a

Table 2.2: This table summarizes the various interface modelling techniques, the shear Reynolds number, Weber and Froude number and the degree of dynamic coupling between the phases

2.4. MAIN INFERENCES

The main discussions based on the review of the existing literature of Two-Phase Stratified flow can be summarized by the following points-

- Table 2.1 and 2.2 summarizes the state of the art direct numerical simulations performed in the recent literature. The numerical method, the flow setting, interface geometry and modelling have been listed. Boundary conditions for almost all of the simulations employed periodic conditions in the homogeneous and free slip boundary condition in the normal direction, with expceptions from [46] simulated with periodic conditions and [31] simulated with periodic and no-slip condition. Moreover, the flow properties like the Re (listed as air,water in-case different Re were used or just one if both were same), We, Fr and the degree of dynamic coupling $\mathscr{R}$ for each of the simulations have also been discussed. Information about the property which was not highlighted in the literature is written as n.a. (not available.) This gives an easy identification of the methods and the properties around which each of the direct numerical simulations is performed, thus also enabling to identify the most suitable setting for this thesis.

- Most of the literature have considered the pseudo-spectral method for the choice of spatial discretization. Spectral methods, in general provide good results when simulating turbulent flow and have an advantage of using high-order interpolation functions which makes is easy to perform computations on a coarse mesh than a very fine mesh with low order finite difference schemes[50]. Most of the literature have used Fourier polynomials in the stream and span-wise directions and Chebyshev polynomials in the normal direction[32][14] ([31] uses second order FDM for the normal direction). For the choice of time intergration, some of the literature solved it with a fractional time step (solving continuity of shear and velocity in fractional times, mostly with Adams-Bashforth and Crank-Nicholson for convective and viscous terms respectively) [32][14][13] and second order Runge-Kutta method in [30]. On the outer boundaries of each of the phases, mainly to prevent turbulence generation at and near walls (other than the interface), a free slip condition is used and for the streamwise and the spanwise directions. To compensate for the loss momentum due to friction, a constant pressure gradient is applied in the stream-wise direction to drive the flow. These choices of boundary conditions and discretization schemes could be considered to implement for this thesis project.

- Interface plays an important role in the turbulent characteristics of each of the phase. The turbulent fluctuations are varied near the interface. And majority of the effects are shown in the region very close to the interface. Many results conclude the instantaneous velocities, pressure fields and the vorticity fields, budget terms in the TKE and the Reynolds stresses are all affected in the Viscous sub-layer and the log-law layer.

- For a flat or a freely deformable interface, most of the effects in the fluid are due to turbulence existing in the flow. But for higher speed to wave-slope ratios, the

velocities have an additional orbital (wave induced component of velocity) motion which has high influence in the near interface turbulent characteristics. This means that the wave induced turbulence becomes more effective [64][11].

- Although, turbulence in the liquid phase (heavier phase) is the most affected and active. Most of the analyses in the gas-side concluded that the gas phase (lighter) perceives the interface as a flexible solid boundary. Hence, the gas-side shows close wall-behaviour (near-wall characteristics).
- Velocities and the lower order statistics show a different behavior than the wall for the liquid side. For different sheared environments, for example wavy stratified flow, the statistics have additional effects. Statistics in the homogeneous directions are enhanced while there's not much effect in the normal directions [13][45][32][31].
- Energy and stress budgets reveal a lot of information about different mechanisms (or individual effects) of turbulence near interface. A common conclusion from all of the authors was that, the dissipation terms seemed to be reducing near the interface. This could be because of the large shear stresses acting across the interface. In case of deformable interface, this is balanced by viscous diffusion. Increase in the diffusive nature, transports the TKE into the bulk region. This is also verified by the pressure-strain correlation. This also shows that, turbulence becomes more isotropic. In a general notion, it could be said that the transport mechanisms are higher and the viscous mechanisms are reducing in nature in the near interface region. [31][14][32].
- Lastly, low speed streaks are formed near the interface. Vorticity fields also show that sweeps dominate near high shear and ejections in low shear region. Quasi-streamwise vortices are known to be formed and some of them are also attached to the interface, justifying coupling mechanisms. [28].

2.5. INITIAL RESEARCH QUESTIONS

To keep it ideal and more purposeful, it is the best to mainly narrow down on performing direct numerical simulations for two-phase stratified flows, with a combination of different pre-processing and post Processing tools, where-in the simulation would be mainly performed in RK-Basilisk (an extension to Basilisk which was developed at NRG). To execute this, the most sensible questions that could be asked are:

R.1 Which of the configuration/setting, either a co-current or a counter-current flow could be simulated so as to achieve results specific to application or close the scientific gap?

R.2 Since the problems needs to simulate sharp interfaces, capture smallest scales of turbulence (which DNS inherently does) a good strategy for meshing needs to be developed.

R.3 The most important question would be as to how the entire simulation would be set up. The choice of spatial and temporal discretizations and the role of boundary

and initial conditions play an important role on the stability and convergence of these simulations.

R.4 Due to the friction at the surface, there is momentum loss. Turbulence is also dissipative in nature. How do we then exactly drive the flow ?

R.5 How is the validation of the obtained DNS data sets going to be performed?

R.6 With the energy and stress budget analysis, much near-interface "information" could be extracted. How can we accurately compute the budget terms and what are the useful inferences that could be collected?

2.6. UPCOMING GOALS AND OBJECTIVES

The main goals for the upcoming graduation project are:

- Validation of RK-Basilisk for a pipe flow and single-phase channel flow using reference DNS data sets.
- Development of stratified two-phase flow configuration: With the identified setting from this literature research, a suitable simulation strategy is developed for the case of two-phase stratified flow.
- Development of a DNS for this flow configuration using RK-Basilisk: As a continuation from the previous step, a direct numerical simulation for the setting would be performed on RK-Basilisk with the HPC clusters at NRG.
- Further Code development on RK-Basilisk: As discussed earlier, the interface dynamics are better studied with TKE budgets. A code would be developed on RK-Basilisk and implemented for the same.
- Analysis and post-processing of the DNS data sets, which include studying the contours, flow properties and the budgets near interface.

3

BASILISK

This chapter discusses the technical aspects of the software used to run the simulations in this thesis. *Basilisk*, a successor of Gerris, is an open-source CFD solver, built on 'C', to solve partial differential equations based on the discretization scheme Finite volume method (FVM). Although this solver is capable of solving a wide array CFD problems, it serves as an excellent tool for simulating multiphase problems. Since basilisk combines adaptive refinement (Adaptive mesh refinement (AMR)) and the Multigrid iterative method, simulating two-phase becomes more feasible.

Usually, the domain is divided into a number of cells where the equations of mass and momentum are solved. This is called meshing. There are situations wherein the accuracy of the solution becomes important in a specific region of interest. To achieve accurate results in these regions, we require a well refined mesh than the regions out of scope for multi resolution analysis. Such grids with multiple resolutions are termed as Non-Uniform (Cartesian) meshes (E.g. - A Shishkin grid to resolve the boundary layer for singularly perturbed problems). But if we expect this region of interest to change dynamically, the mesh needs to "adapt" with respect to a few constraints specified. A method that uses efficient algorithms to generate dynamic meshes which adapt to the accuracy within sensitive regions over time is called *Adaptive mesh refinement (AMR)*. For example, simulating bubble-bubble interaction or a Taylor bubble would be computationally cheaper on AMR since the region of interest/study would be the gas-liquid interface and not the continuous phase itself. Basilisk, which works on AMR, facilitates to simulate them with different resolutions based on a user-defined inputs as the maximum and minimum level refinement and a field based on which the refinement is done. The same applies to stratified two-phase flows, where it is necessary to capture the dynamics in the near-interface region. Basilisk restricts this to be a scalar field and as immediate examples, one could specify the phase fraction or velocity gradient field etc.

3.1. NUMERICAL MODELLING IN (RK-) BASILISK

Basilisk is a solver which combines non-uniform quadtree and octree based discretizations with finite volumes, AMR and multigrid. The momentum equations are solved with an approximate projection scheme [44]. The Poisson's equation for pressure is solved thereby ensuring the incompressibility constraints. Additional modules and conditions are also available for problems with embedded boundaries. RK Basilisk is a solver developed at NRG by making a few amendments to the standard Basilisk solver. A few notable concepts in (RK-)Basilisk are:

- A general idea of discretizations, time integration procedures are given in [44]. Although this reference is based on Gerris, it closely resembles the features of Basilisk. Similar to the standard Basilisk solver, RK-Basilisk uses a projection-based algorithm to solve the momentum equation. To be precise, it uses the *Pressure Implicit Splitting of Operators (PISO)* scheme. A range of implicit and explicit time integration schemes are available to solve the equations, following the Butcher-Tableau of definitions. Choices are also available for a discretization of the convective scheme. For the simulations of stratified flow, a 3 stage RK method for time integration and a central difference scheme for the convection term were chosen.

- In non-body confirming grids, the flow does not always align with the grid. This is generally referred to as immersed boundaries. Another similar concept is also an embedded boundary. Both the standard and RK-Basilisk solver have the capability to solve problems with complex flow geometries. Wall damping and penalisations are introduced to the solver to tackle these boundaries.

- Another possibility in RK-Basilisk is to solve the full discretization of the viscous term

$$\mathbf{D} = \frac{\mu}{2}(\nabla \mathbf{u} + \nabla \mathbf{u}^T) \tag{3.1}$$

  which leaves second part the rate of strain tensor to be non-zero, staying fully discretized.

- Fields in both standard Basilisk and RK-Basilisk are available which are basically iterators over physical fields. Instead of the conventional *for-loops* inherent to C, (RK-) Basilisk introduces iterators which can iterate through cells (*foreach()*), faces (*foreach_faces()*), boundaries (*foreach_boundary()*), dimensions (*foreach_dimension()*) etc. These iterators are necessary to apply/modify boundary conditions, compute fluxes etc.

- For explicit time marching iteration-based schemes, to ensure convergence, it is important to have a correct CFL condition. In this case, (RK-) Basilisk offers a predefined function under which the user could input a value prior to the simulation based on the problem being solved so as to ensure convergence.

By default, Basilisk initiates a square domain in 2D and a cubic domain in 3D and hence is not desirable to study the boundary layer phenomenon. In these situations,

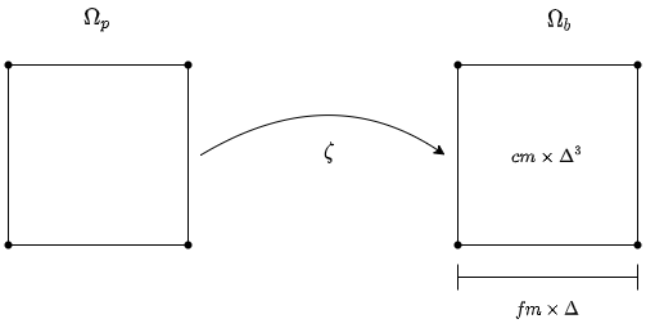

Figure 3.1: Grid transformation of $\Omega_p \rightarrow \Omega_b$ with included metrics

(RK)-Basilisk offers to stretch the domain by certain deformation and cell stretch functions (more to be discussed in the upcoming chapters).

Before discussing the deformations and cell stretching, metrics in Basilisk are introduced. It is vital to know that Basilisk does not have the physical definitions of cell volumes and cell faces. Assuming we have a physical domain, Ω_p, with uniform spacing, the finite volumes would be unit cubic cells having area :

$$A_p = \Delta^2$$

and volume:

$$V_p = \Delta^3$$

where $\Delta = \frac{L}{N}$, is the cell to cell distance with L and $N = N_x = N_y = N_z$, being the length and the number of cells respectively. Basilisk maps these unit cubic cells belonging to a uniform grid, Ω_p to cubic cells belonging to a transformed grid in, Ω_b additionally with the so called *metrics* (also shown in Fig.3.1), such that: $\zeta : \Omega_p \rightarrow \Omega_b \mid \Omega_p, \Omega_b \subseteq \mathbb{R}^d$, $d = 1,2,3$.

$$\mathbf{x_b} = \zeta(\mathbf{x_p}) \tag{3.2}$$

$\mathbf{x_b} \in \Omega_b \subseteq \mathbb{R}^d$ and $\mathbf{x_p} \in \Omega_p \subseteq \mathbb{R}^d$.

With metrics, the transformed volume and area could be defined as:

$$V = cm \times \Delta^3$$

and

$$A_f = fm \times \Delta^2$$

where cm and fm are the cell and face metrics respectively. Since they map to a uniform grid, the metrics are equal to unity. But there is a possibility to have a new definition for the metrics in order to have a non-uniform grid, subjected to deformations.

For studying single phase or two phase stratified flows, we need accurate information near interface and near walls. Using adaptive mesh refinement might not lead to the same accurate solution at all time instants. One of the few reasons is that the interpolation coarse grid to a fine grid is shown to have spurious excitation in the spectrum of turbulence [37]. In this case, it is advised to have a high-resolution static mesh to resolve the boundary layers. Although (RK-) Basilisk offers as an extensive tool for AMR and multigrid for simulating multiphase flows, due to the importance of resolutions, other computational efforts and considering the geometry of the interface (discussed in the upcoming chapters), an alternative solution is to construct meshes with a high resolution near the boundary and to gradually coarsen it towards the region where the solution is not as important, by means of stretching, deformations and metric changes to have non-uniform boundary confirming grids, which is what is adapted in this thesis, introduced in the next chapter.

4

SINGLE PHASE FLOWS

As mentioned in the previous chapters, this thesis moves forward to the main goal, that is to accurately develop a methodology to perform DNS of two-phase turbulent stratified flow. Before going ahead with the aforementioned task, a Single phase problem is studied, modelled, simulated, validated and understood so as to help us put in initial contact with the canonical problem of the two-phase turbulent flow. This chapter is aimed to establish the key concepts, development of methodology, statistics of turbulence and some initial results which could then be correlated or extended to the two-phase flow problem. Hence, the concepts of meshing, averaging strategy and the results are explained a bit more extensively. Initially the numerical methodologies are discussed, followed by a section strategies to construct an efficient mesh. Next, the actions of the averaging procedure is briefly explained and finally some results are shown and elaborated.

As there are many classical studies based on pressure driven turbulent pipe and channel flows (ref [17] [36] [1]), a the focus is shifted to study turbulent Couette flows instead. The key difference between channel flows and Couette flows is the way how the flow is driven. Flows that are purely driven by shear, known as Couette flows were studied in [20][39]. One of the bounding walls is moved with a shear velocity relative to the other (which is a stationary wall) to impose the required wall shear stress based frictional Reynolds number. [20][39] base their main study on the large structures which are observed in the bulk region of the channel. Because of these large-scale structures in Couette flow, slightly higher production and diffusion is observed along with a balance in the transport of momentum fluxes of $\langle u'v' \rangle$ and fluctuating pressure.

In some of the studies for example in, [19] [5] and [18], the flow was driven by both pressure and shear. This is particularly possible if there is free slip imposed on a moving wall, and the flow being driven by a mean pressure gradient, and generally called as Couette-Poiseuille flows. All three works employ a pressure gradient which is applied dynamically to balance a superficial wall shear stress. The computational methods adopted were FDM on a staggered grid, with a Crank-Nicholson scheme for the time

integration. It is seen that the Reynolds stresses and the turbulent intensity are higher which leads to an elongation of the logarithmic region when compared to pure pressure-driven - Poiseuille flows with a similar Re_τ.

Another interesting DNS of turbulent plane Couette flow was studied by the group of [56]. A DNS was performed to solve the governing equations by FDM using Crank-Nicholson and Adam-Bashforth for time integration. The flow was driven by moving the top wall with a certain wall velocity, U_w relative to a stationary bottom wall, whereas periodic B.C. were used in the homogeneous directions. Two-point velocity correlations provided evidence to use large enough computational domains to capture the large structures. A TKE budget equation is solved to study the individual $\langle u_i u_j \rangle$ budgets. A Re_τ dependence is observed for some of the terms in the budget of $\langle u'v' \rangle$ and $\langle v'v' \rangle$

In all of the presented literature, none of them were based on the Finite Volume Method for a DNS. Considering this as an amendment to this thesis, the modelling and the simulation is done in RK-Basilisk, which is based on FVM and it is shown that good statistics could be obtained even with using low order interpolation functions on coarse meshes when compared to the classical spectral methods. Considering the goals of this chapter, since [56] presents concise and adequate information on modelling, statistics of velocities and budgets, this study is adapted as a reference case and are validated against the simulations performed in RK-Basilisk.

4.1. NUMERICAL METHODS

The brief literature survey informed about the various trends in simulating Single phase turbulent flows. The key difference in these simulations were the flow driving mechanisms, where either a streamwise pressure gradient $\nabla_x \tilde{p}$ or a wall shear stress τ_w is applied to drive the flow by a pressure difference or by shearing the boundaries respectively. As discussed earlier, considering the main goal of this thesis which aims to solve a two-phase shear driven flow like [31], we adapt to solve the Single phase turbulent flow with this same mechanism as presented in [56] and validate the results using NRG's solver RK-Basilisk.

Numerical simulations are performed to solve the Navier-Stokes in a channel as shown in Fig.4.1. It is sometimes useful to represent velocities in a different scale, i.e, when non-dimensionalised with a certain reference velocity. As we know turbulent flows scales with shear, we use a velocity scale which is directly associated with the shear stress. This velocity scale is obtained by non-dimensionalising the velocity by a reference velocity called *shear* or *frictional* velocity. This frictional velocity, u_τ could be defined by:

$$u_\tau = \sqrt{\frac{\tau_w}{\rho}} \tag{4.1}$$

where $\tau_w = \mu \frac{\partial u}{\partial y}$ is the associated shear stress, known as the *wall shear stress*. The shear velocity becomes important in the near-wall region since it characterizes the tur-

bulent scales and strength. By using u_τ as the reference velocity, the half-height H as

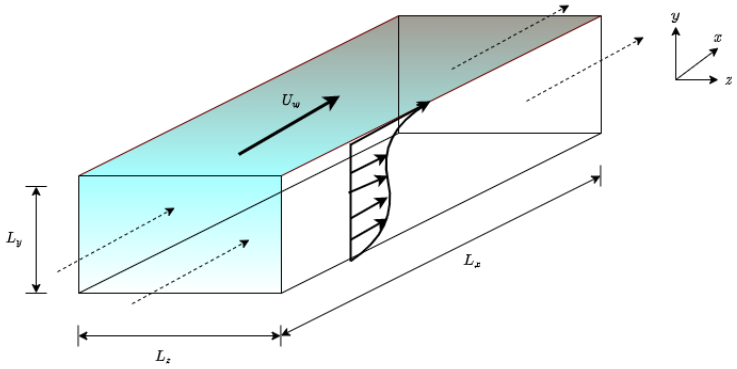

Figure 4.1: The computational domain for the problem simulated

the reference length scale and t_s as the reference time scale, we non-dimensionalise the Navier-Stokes equations which results in :

$$\frac{\partial \tilde{u}_i}{\partial \tilde{t}} + \frac{\partial \tilde{u}_i \tilde{u}_j}{\partial \tilde{x}_j} = -\frac{\partial \tilde{p}}{\partial \tilde{x}_i} + \frac{1}{Re_\tau}\frac{\partial^2 \tilde{u}_i}{\partial \tilde{x}_j^2}$$
$$\frac{\partial \tilde{u}_i}{\partial \tilde{x}_i} = 0 \tag{4.2}$$

which are solved in a computational domain, Ω_{nb} of the size $(L_x \times L_y \times L_z) = (2\pi \times 2 \times \pi)$. The numerical discretization is based on the second-order finite volume method. Discretization for the convective term uses a central difference scheme. A second-order explicit 3-stage Runge-Kutta method has been used to integrate the convection and diffusion terms in time. Hence, to ensure convergence, a CFL = 0.4 has been used. Simulations are performed for a shear Reynolds number, $Re_\tau = 126$ which corresponds to $Re = 8600$, which is in a turbulent regime of wall-bounded flows.

The required wall shear stress, τ_w is imposed by choosing a certain frictional velocity. Range of values for the ratio of $\frac{u_\tau}{U_w}$ was given in [31]. By choosing $u_\tau = 1$ the ratio $\frac{u_\tau}{U_w} = 0.02937$ gives $U_w = 34.0$. Hence, the top wall is constrained to have a no-slip boundary, $U_w = 34.0$ (represented by a thick solid arrow in Fig4.1) relative to the bottom wall, $U = 0.0$. Instead of a well defined inlet and outlet, we have a periodic domain. Hence, we have periodic boundary conditions in the streamwise and the spanwise direction (represented by the dashed arrows in Fig4.1).

As a general practice, the perturbations are added in to generate a turbulent flow after the flow is developed. But in our simulations, sinusoidal profiles superimposed on a linear profile of velocity to start with a turbulent flow. In the homogeneous directions,

the initial profiles are:

$$\tilde{u}(y,z) = \left(\frac{U_w}{2}\right)(y+H) + \frac{\sin(4z)}{4}$$
$$\tilde{w}(x) = \left(\frac{U_w}{2}\right)\frac{\sin(2x)}{4} \tag{4.3}$$

A general workflow is followed in pre and post processing this Single phase test case. The same workflow is followed for the upcoming two-phase model as well. Initially, the problem to be simulated is understood from the test case. A brief survey helps to understand and translate the reference case so as to model it in NRG's solver RK-Basilisk C. Codes are written to set up the physics, discretization schemes, boundary conditions, flow initialisation etc. The strategy for meshing (discussed in chapter 4.2) is also implemented along with the code, as a part of the pre-processing stage. Depending on the problem size, simulations are run in parallel in NRG's HPC cluster. As the simulations are running, a script averages the instantaneous quantities and stores it as scalar fields. This completes the simulation stage. The post processing stage is started by visualising the flow fields, examining the scalar fields for correctness. In case, if there are any discrepancies in the solution, the simulations are run again after rectifying the issue. If not, another script ensemble averages over space and time (stored as N snapshots at user defined intervals as the simulation progresses) by interpolating data from an unstructured RK-Basilisk grid to a structured grid. This returns a number of scalar fields by averaging over a 3D domain to a 2D space in the wall normal direction. Finally, a python script is written for final stages of post processing the ensemble averaged quantities and to visualise the mean velocities, r.m.s', turbulent kinetic energy budgets etc.

4.2. MESHING

Since we have two rigid walls, the flow is confined and interacts with it. The presence of these walls directly influences the overall turbulence in the channel. It is essential to capture the associated turbulent boundary layers as accurate as possible. Moreover, considering the goal of this chapter, which is to study the TKE budgets, they become locally important in these near-wall viscous regions. Hence, the mesh needs to be constructed with a resolution that is fine enough to capture these layers. Since we know that DNS is already computationally expensive and restricted to small domains, it is not always feasible to adapt to a higher-level grid (i.e, a mesh with more cells than a given level). A foremost goal would be to find an "adequate grid" that has a good agreement of the statistics with [56]. Of course, moving onto a higher-level grid will be interesting to visually study and to post-process the data.

In section 3, it was discussed how a grid is transformed from a physical space, Ω_p to Basilisk space, Ω_b by a mapping. A unit cubic cell a mapped to a cube which includes new metrics cm and fm. But there is also a possibility that they could be mapped to form a non-uniform grid, Ω_{nb} as well, which are subjected to deformation and stretching (see Fig 4.2). Cells belonging in and around the boundary layer need to be stretched and deformed with a strategy that would essentially capture all the necessary information. The basic idea is to have a non-uniform grid with homogeneous deformation in

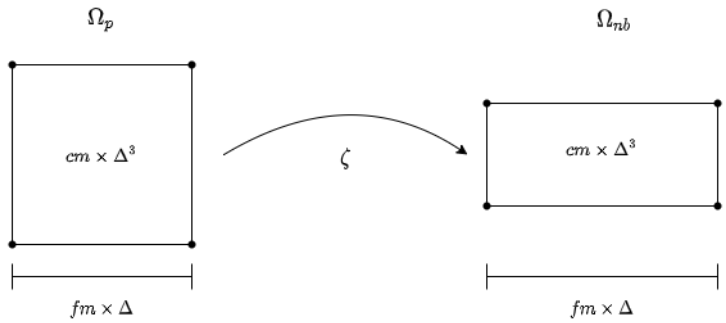

Figure 4.2: Mapping of an untransformed cell from Ω_p to a stretched cell in Ω_{nb}

the streamwise and the spanwise directions, but a highly clustered grid near the top and bottom boundaries in the normal direction. Hence, we need a transformation that maps the uniformly spaced grid, Ω_p to a non-uniform grid, Ω_{nb} (non-uniform basilisk domain) with the use of some cell stretching and deformation functions.

As a first step, a geometric grading ratio is determined. This grading ratio, also known as a *grading factor* controls the growth of each cell based on the cell width. Based on a given first cell height Δ_0 of Ω_p, half-height,H of the domain and the number of cells in the normal direction, N_y a function determines a constant grading factor, α which could be represented by:

$$\alpha = \eta(\Delta_0, H, N_y) \tag{4.4}$$

For Ω_p which has the normal coordinates y_i, $i = 1, ..., N_y$, the cell width with a 'constant stretching' can be written as:

$$\Delta_i = y_{i+1} - y_i = \alpha \Delta_{i-1}$$

Based on this, we can also define a cell width to be based on the first cell height, Δ_0 leading to a non-uniform grid:

$$\Delta_i = \alpha^i \Delta_0 \qquad i = 0, ..., N_y$$

Hence, the wall normal coordinates of this deformed grid can be constructed by a deformation function, $\zeta : \Omega_p \rightarrow \Omega_{nb} \mid y_{nb} = \zeta(y_i, \alpha, \Delta_0)$, $y_{nb} \in \Omega_{nb}$ and $y_i \in \Omega_p$, where Ω_{nb} is abbreviated for a non-uniform deformed basilisk domain, which maps a uniform grid to a non-uniform grid:

$$y_{i,nb} = \zeta(y_b, \alpha, \Delta_0) = y_0 + \sum_{i=1}^{i<Ny-1} \alpha^i \Delta_0 \tag{4.5}$$

where y_0 is the first wall normal co-ordinate and $\sum_{i=1}^{i<Ny-1} \alpha^i \Delta_0$ is the formed by a geometric progression:

$$\sum_{i=1}^{i<Ny-1} \alpha^i \Delta_0 = y_0 + \Delta_0 \left(\frac{\alpha^i - 1}{\alpha - 1} \right) \tag{4.6}$$

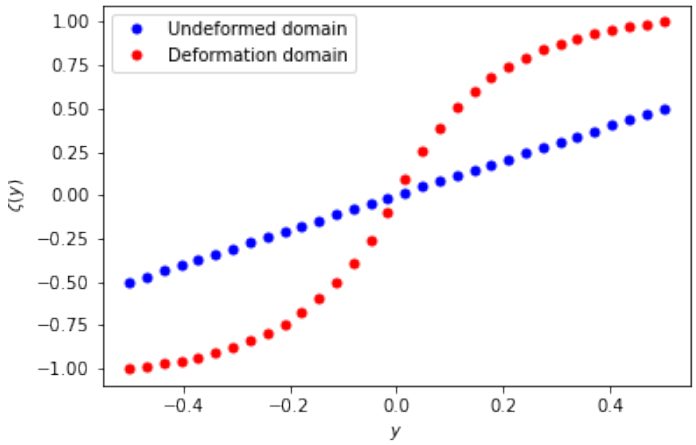

Figure 4.3: Transformed and untransformed coordinates, $y \in \Omega_p$

A typical transformation of grid is represented in Fig4.3. Two different curves are presented. A normalised $\Delta y_0 = \Delta y_0^+ = \frac{\Delta_0 u_\tau}{\nu}$, (here, Δy_0 is the first cell width) $N_y = 32$ and $H = 1$ has been used as the first cell height, the number of points and the half-height respectively. Blue markers represent coordinates, $y_p \in \Omega_p = [-0.5, 0.5]$ and red markers represent the deformed grid coordinates, $y_{nb} \in \Omega_{nb} = [-1, 1]$, therefore stretching the further by 0.5 units in both the normal directions. If a transformed grid has no deformation and it is clear that this curve will have an $\alpha = 1$, representing an uniformly transformed grid. Hereafter, the wall normal coordinates are not represented as y_{nb}, but just as y to maintain simplicity and uniformity. Although, when non-dimensionalised distances are written, they are denoted appropriately.

In Basilisk, it is not only sufficient to model the transformation of the normal coordinates but to specify the magnitude by which each cell is stretched so as to perfectly fit in with these transformed coordinates. It might be confusing to sometimes differentiate between the grading factor and cell stretching. Grading factor is basically an expansion ratio which is a constant determined based on the global parameters, while cell stretch is a function that stretches a cell based on the local coordinates. Upon observation, we can notice these cell stretches are basically the derivatives of the deformation function, which determine a factor by which the cells are expanded/compressed. This stretching function is clearly represented in Fig.4.4. We clearly have a high peak around 0, two cells sharing the maximum magnitude of stretching and the lowest at the other ends. This depicts that the cells in the bulk regions are stretched more when compared to the cells in the top and the bottom wall. Hence the near-wall region has a fine resolution, which is exactly what we desire. To get visual understanding, these cells are visualised as edges in paraview as shown in Fig.4.5. The clustered cells are visualised better on a mesh with lower level; $N_x \times N_y \times N_z = 64 \times 64 \times 64$ cells. It is clear that the bulk region has a very

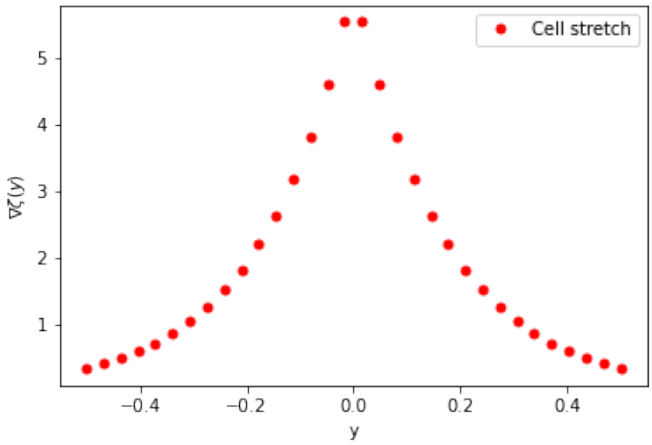

Figure 4.4: Cell stretching, $y \in \Omega_p$

coarse mesh, with the near-wall regions being refined well. We now have a mesh which geometrically progresses from the wall towards the bulk and declines away from the bulk towards the other wall.

To have good accuracy in capturing the boundary, the value y^+ should be chosen to be in the viscous sub-layer. This simply means that the first cell should have a certain value that falls under the thickness of the viscous sub layer. For internally bounded flows, $y^+ < 5$ represents the viscous sub layer. This y^+ value coming out by normalising the y-coordinate by $\frac{\nu}{u_\tau}$, is a non-dimensionalised wall normal distance (in the non-uniform deformed basilisk domain). A more compact definition

$$y^+ = \frac{yu_\tau}{\nu} = \frac{yRe_\tau}{H} \tag{4.7}$$

basically, represents the 'local frictional Reynolds number'. Similarly the non-dimensionalised cell width is written:

$$\Delta y^+ = \frac{\Delta y u_\tau}{\nu} = \frac{\Delta y Re_\tau}{H} \tag{4.8}$$

In our simulation, we choose $\Delta y^+ = 1.5$ to resolve the layers adequately for M6 and M7. Moving to a higher mesh, M8 which has 256 cells in each direction, this Δy^+ value was found to be too big in order to find a grading factor, α. Hence, the Δy^+ value is lowered to 0.9 (only for the M8 mesh) to produce a grading factor. We run the simulations for $Re_\tau = 126$. Hence, we place the first cell at

$$\Delta y = \left(\frac{\Delta y^+}{Re_\tau}\right)$$

which seemed to be a good resolution to resolve the layer. Simulation runs are performed on 3 different meshes, $M6, M7, M8$ which has $2^6, 2^7, 2^8$ cells in each direction

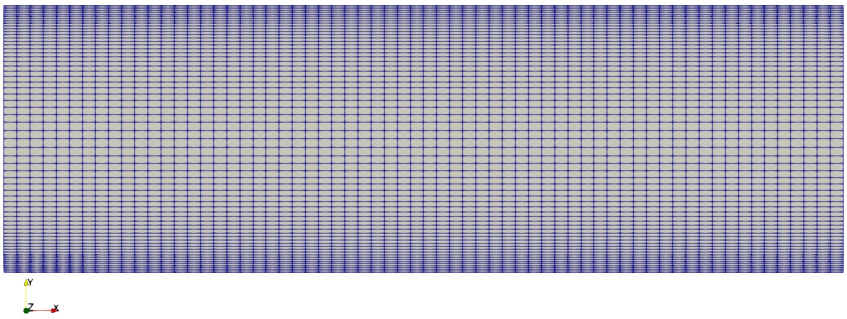

Figure 4.5: A visualisation of the clustered mesh constructed with deformations on a 2D-plane

respectively. The mesh statistics are presented in the Table4.1:

Mesh	Shear Re	First cell width	Domain	Grid	Resolution		
M	Re_τ	y^+	$L_x \times Ł_y \times L_z$	$N_x \times N_y \times N_z$	Δx^+	Δy^+	Δz^+
M6	126	1.5	$2\pi \times 2 \times \pi$	64 ×64 × 64	12.3	1.5 - 8.32	6.18
M7	126	1.5	$2\pi \times 2 \times \pi$	128 ×128 × 128	6.18	1.5 - 2.54	3.09
M8	126	1.5	$2\pi \times 2 \times \pi$	256 ×256 × 256	3.09	0.9 - 1.07	1.54

Table 4.1: Mesh statistics for Single phase flow

As we move onto level 8 meshes and higher, the normalised cell width remains almost the same. This means that, if we adapt to meshes with higher resolution, $\alpha \approx 1$, giving almost a uniform mesh. In this case, it is safe to stay with an adequate resolution and avoid the higher computational cost. Keeping this in mind, a mesh independence study is performed to in order to find the accuracy of the solution compared to the test case for a given mesh, Fig4.6. The mean velocity profile in the logarithmic scale is monitored. It is seen that all the 3 meshes have a good agreement with the profiles from the reference case. But since M8 has an even lower first Δy^+ value, and more number of cells (more cells clustered in viscous sub-layer), this resolution has captured the viscous sub layer more accurately than the other two meshes. But as the statistics are concerned, all 3 meshes gave almost identical results.

4.3. RESULTS

We wish to validate the results of [56] against the simulations performed in RK-Basilisk. The research group tests the results for different frictional Reynolds numbers and differ-

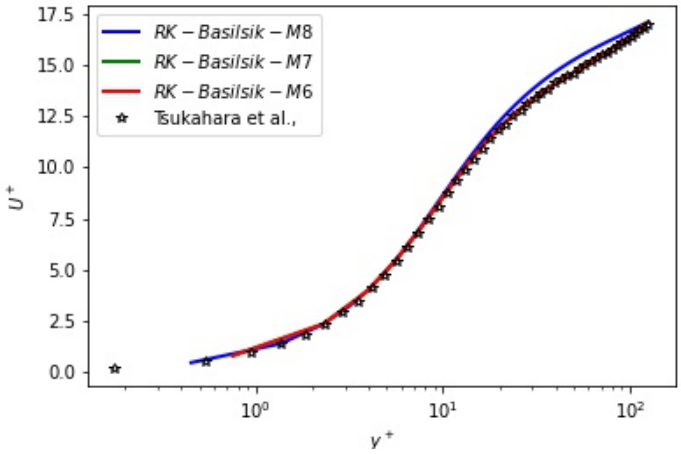

Figure 4.6: Mean velocity plotted against a height in logarithmic scale for 3 different mesh resolutions

ent sizes of the computational domain, we wish to validate only for $Re_\tau = 126$. Although they use higher-order FDM for computations, it should be nevertheless interesting to see how well lower-order FVM performs for these turbulent simulations. Initially, the lower order statistics are shown, followed by some higher order statistics along with some visualisations and contours. Later, we move on to the interesting part of studying the TKE budgets.

4.3.1. AVERAGING

Once the flow is fully developed they are averaged in the following way:

- Initially, the mean quantities of the variables are computed in a particular time step,

$$\Phi(\mathbf{x}, t_a) = \frac{1}{\Delta t_a} \int_{t_a}^{t_a+\Delta t_a} \phi(t_a, \mathbf{x}) dt_a \tag{4.9}$$

  where t_a is time step for averaging. Equation 4.9 is the time average of the instantaneous value over a given time interval $\Delta t_a >$ smallest time scale of turbulence. At a user-specified interval, these averages are stored as snapshots. In particular, a snapshot is a range of data sets (scalars of flow variables and gradients) that are useful information to study mainly the statistics and the budgets.

- Since there are N number of snapshots/realizations, the scalars are further averaged by the *ensemble averaging*. This is done in three steps.
  With a similar methodology discussed in sec 4.2, a structured Cartesian mesh is constructed. An algorithm interpolates the time averaged quantities from Basilisk grid to this Cartesian grid. This is because, the Basilisk grid is unstructured and requires additional efforts for averaging. Hence, the data is located in the unstructured grid and interpolated to a structured (Cartesian) grid and averaged. Secondly

the interpolated data is ensemble averaged over snapshots (after attaining steady state):

$$\Phi(\mathbf{x}) = \lim_{T\to\infty} \int_{t_a \in T} \Phi(\mathbf{x}, t)\, dt \tag{4.10}$$

Next, yet another ensemble averaging is performed over space to find an averaged quantity as a function of domain height. For a given 2D slice , the variables are plane averaged. Several slices of these planes at different wall normal coordinates are averaged again to give a final averaged quantity in space.

$$\langle \Phi(y) \rangle = \left[\left(\frac{1}{(N_x \times N_z)} \sum_{k=1}^{N_z-1} \sum_{i=1}^{N_x-1} (\Phi(\mathbf{x})) \right) \right] \tag{4.11}$$

4

For computing some higher-order statistics, gradients and second derivatives need to be computed from the ensemble averaged quantities. This is especially important to study the budget terms since the budgets contain the gradients and the second derivatives in their individual definition.

For the gradients, firstly the fields are interpolated on the faces by a weighted average of their cell metrics.

$$\langle u_f(y) \rangle = \frac{cm^+ \langle u_{-1} \rangle + cm^- \langle u \rangle}{cm^+ + cm^-} \tag{4.12}$$

Then a simple forward difference operator constructs gradients over these interpolated face values

$$\frac{d\langle u \rangle}{dy} \approx \frac{\langle u_f \rangle - \langle u_{f_{-1}} \rangle}{cm \times \Delta} \tag{4.13}$$

Similarly, for the second order derivatives, two consecutive gradients are constructed. Firstly, a gradient is computed between the cell-centered value to be approximated on the cell face.

$$\frac{d\langle u \rangle}{dy}_f \approx \frac{\langle u \rangle - \langle u_{-1} \rangle}{cm \times \Delta} \tag{4.14}$$

Again, a the second gradient is taken over these cell faces to approximate the second derivative, which is defined on the cell center

$$\frac{d^2\langle u \rangle}{dy^2} \approx \frac{\frac{d\langle u \rangle}{dy}_f - \frac{d\langle u \rangle}{dy}_{f_{-1}}}{cm \times \Delta} \tag{4.15}$$

This depicted an overall picture of how the instantaneous quantities are (ensemble) averaged in time and space. Although the constructed gradients and second derivatives have a high truncation error in the numerical discretization, these lower order approximation seem to be sufficient for the present study.

4.3.2. MEAN VELOCITY AND FLUCTUATIONS

The instantaneous (non-dimensional) velocity component u_i can be expressed by the Reynolds decomposition

$$\tilde{u}_i = \langle \tilde{u} \rangle + \tilde{u}' \tag{4.16}$$

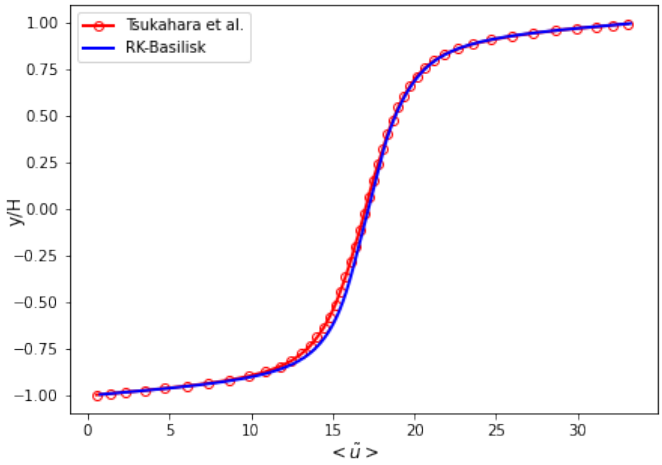

Figure 4.7: Mean velocity $\langle \tilde{u} \rangle$ plotted over domain height y/H

where $\langle \tilde{u} \rangle$ and $\tilde{u}'$ are the mean and the fluctuating part of velocities. After the flow is statistically steady, the flow is averaged to compute the mean quantities. Since there is only net flow in the streamwise direction, the mean quantity in the spanwise direction and the normal direction is negligible and thus $\langle \tilde{v} \rangle = \langle \tilde{w} \rangle = 0$.

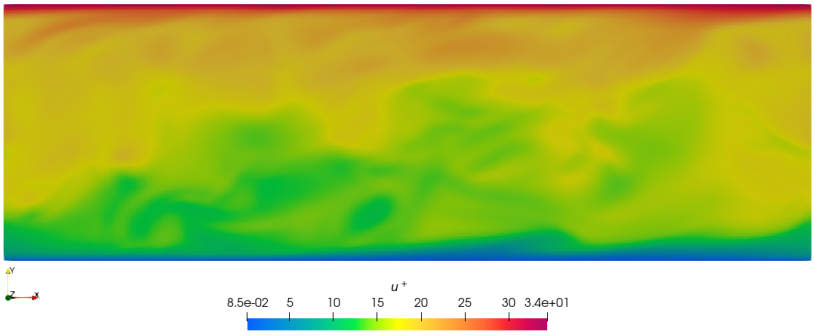

Figure 4.8: Instantaneous velocity magnitude from a snapshot taken at $t^+ = 80$ on a M8 mesh

Figure 4.8 shows the instantaneous velocity magnitude from a snapshot taken at $t^+ = 80$ on M8 mesh. The bulk of the flow is chaotic, consists of disturbances and is non smooth, which visually confirms the channel to be turbulent. The regions near the

top and the bottom walls constitute the maximum and minimum velocity respectively. The bulk region has velocities in the range $12 < \tilde{u} < 22$. $\tilde{u}$ is shown to be u^+ in the legend to also represent a non-dimensional scale.

Figure 4.7 shows the mean streamwise velocity $\langle \tilde{u} \rangle$. The values are compared against the reference data from [56]. We see that there is a very good agreement with our test case. Compared to turbulent pressure driven channel flows, Couette flow do not preserve the axis-symmetric parabolic velocity profile. A no-slip velocity at the top plate creates sharp gradients in this region, showing similarities to a stationary wall in a turbulent flow. This makes the channel to have a rotationally symmetric monotonic "S-shaped" velocity profile. Naturally a stationary bottom wall also acts as a generator of turbulence making the region around the wall to have sharp gradients. Moving away from the walls towards the bulk of the flow ($-0.75 < y/H < 0.75$), the velocity profile has a very small slope. These slopes represent the mean streamwise gradients of the flow, which are shown in Figure 4.9. Near the bounding walls, ($-1 < y/H < -0.75$ and $0.75 < y/H < 1$), the gradients are typically higher, ranging from ($125 < y/H < 0.2$ and $0.2 < y/H < 125$) respectively. This shows that the near-wall regions show very high viscous effects, due to a high turbulence activity. In the bulk region, the gradient is more or less a constant and as also seen from the velocity profile, the gradients do not exactly die out, but have a very small finite value. Since a non-zero gradient exists at the center line, and $\mu^+ \neq 0$, the channel has a non-zero shear stress. [56] report these values of mean streamwise gradient at the center line of the channel to be 0.184. From our computations, we find the value to be 0.225 which is a good agreement, suggesting that the bulk flow has been adequately resolved.

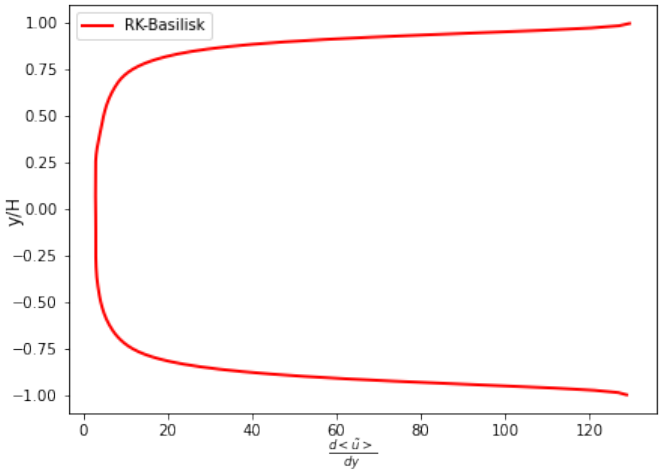

Figure 4.9: Streamwise velocity gradient in the normal direction

The mean velocity in inner variables is shown Figure 4.10. Inner variables or inner scales refer the representation of velocity in wall units. This is done by studying it in a logarithmic scale. The velocity is represented in such a way that it scales with the logarithmic distance from the wall in the normal direction. This is also known as law of the wall [49]. The logarithmic wall normal distance is divided into several regions that associates the strength of viscous and inertial motions in the fluid. It was previously discussed that the first cell center should be placed within the viscous sub layer i.e $y^+ < 5$. Principally the velocity should start from $\langle \tilde{u} \rangle = 0$ which ensures that the viscous sublayer has been fully resolved. Although in this study, we see that it has not been resolved. But this does not mean that we have an inadequate resolution, since we have non-zero velocity within the viscous sub-layer. It is seen that the viscous sub layer covers the extent until $y^+ < 5$. This is where the viscous effects dominate in the entire flow due to the high shear rate imposed by the wall. The buffer layers extends from the viscous sub-layer until $y^+ < 30$. The viscous effects are weaker than in the viscous sub-layer. The log-law layer is active from $y^+ > 30$. Due to turbulent stresses, the inertial effects are as important as the viscous effects in this region. The mean velocity is plotted until the center line of the channel. The center line velocity is averaged to be at $\langle \tilde{u} \rangle = 17.5$. The corresponding y intercept is at $y^+ \approx 120$, which is the frictional Reynolds number that is imposed confirms the definition of it too.

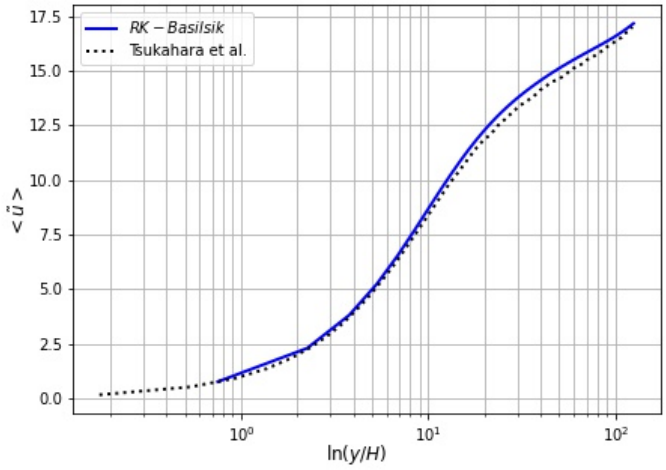

Figure 4.10: Mean streamwise velocity $\langle \tilde{u} \rangle$ plotted as in a logarithmic scale

The turbulence intensity is compared for all of the 3 velocity components in Figure 4.11 each represented by a colour : Yellow for the streamwise component, red for the spanwise component and green for the normal component. The root-mean-squared values of the fluctuating velocity component from the Reynolds decomposition of velocity informs about the turbulence activity in a region. Fluctuations produced by the

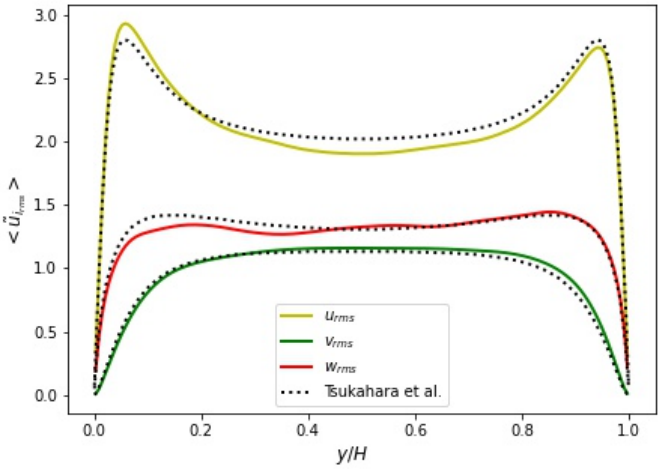

Figure 4.11: R.m.s fluctuations are shown for all 3 components. Values are compared against the reference data set from [56]

streamwise component are higher than the spanwise and the normal component. The peaks of the streamwise velocity fluctuations appear in the near-wall region, confirming walls to be a big source for turbulence. The spanwise fluctuations are higher than the normal fluctuations and but both of them seem to attain a constant value in the bulk region of the flow. The test case shows a small under prediction for the streamwise fluctuations but has a good agreement with the reference case for the other two components. Compared to channel flows where the fluctuations have a local minima at the center line of the channel, Couette flows do not show this behaviour. All 3 components show a constant value throughout the bulk region. With these constant fluctuations, a non-zero turbulent shear stress exists at the center line of the channel.

4.3.3. REYNOLDS AND TOTAL SHEAR STRESS

Upon averaging the NSE, an equation for the mean flow could be obtained and leads to an additional fluctuating stress component apart from the averaged quantities. This additional term is the contributor of fluctuations to the momentum flux in the mean motions of the flow. This forms a tensor, which is commonly referred to as the *Reynolds stress tensor*, governing the turbulent shear stress induced in the flow. This rank 2 tensor can be denoted by:

$$R_{ij} = -\rho \left\langle \tilde{u}_i \tilde{u}_j \right\rangle \tag{4.17}$$

For a flow with constant density, the Reynolds tensor can be written as: $R_{ij} = -\left\langle \tilde{u}_i \tilde{u}_j \right\rangle$. The element $R_{12} = R_{xy} = -\left\langle \tilde{u}' \tilde{v}' \right\rangle$ is studied in Figure 4.12. A very good agreement of is obtained with the reference case. The turbulent shear stress contrasting to the viscous shear stress. The bulk flow is majorly influenced by the large motions which contributes to a high turbulent shear stress. Most importantly, due to non-zero turbulence intensity,

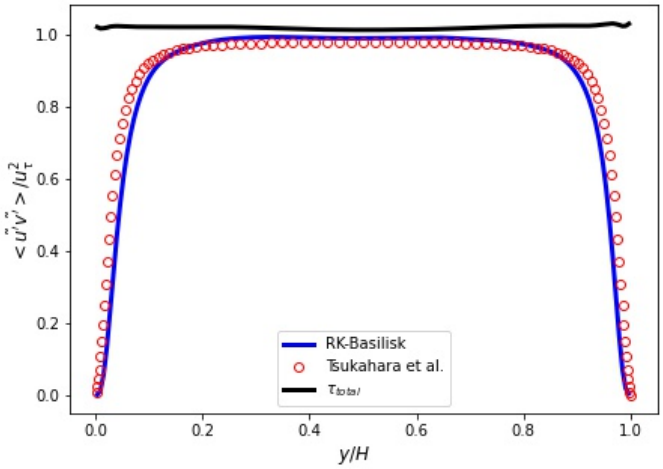

Figure 4.12: Reynolds shear stress $R_{xy} = \left\langle \tilde{u}_i \tilde{u}_j \right\rangle / u_\tau^2$ is compared against the reference of [56]. The total shear stress τ_{total} is also shown. $y/H = 0$ is the bottom wall and $y/H = 0$ is the top wall.

the turbulent shear stress has a constant value of 0.8 in non-dimensional units throughout the core of the flow.

Contributions to shear stresses arise due to both viscous effects and turbulent effects. Both the effects dominate in different regions in turbulent Couette flow. By integrating the x-momentum equation for the mean flow and using the physical conditions for a plane Couette flow, a relationship for the total (planar) shear stress τ_{total} can be obtained [56].

$$\begin{aligned} \tau_{total} &= \mu^+ \frac{d\langle\tilde{u}\rangle}{dy} - \frac{\langle \tilde{u}'\tilde{v}' \rangle}{u_\tau^2} \\ &= \tau_{visc} + \tau_{turb} \\ &= 1 \end{aligned} \tag{4.18}$$

where $\mu^+ \frac{d\langle\tilde{u}\rangle}{dy}$ is the contribution due to viscous effects and $\frac{\langle \tilde{u}'\tilde{v}' \rangle}{u_\tau^2}$ is the contribution due to turbulent effects, better termed as viscous stress and turbulent shear stress (or Reynolds shear stress) respectively. Interestingly, shear stress is obtained to be a constant of unity, which is found to be constant at all heights confirming the inference from the previous section. A constant shear stress value of 1 in non-dimensional units is a good indication that the flow is statistically steady [56]. From Figure 4.9, it is deducible that τ_{visc} due to the mean streamwise velocity gradient, is weaker in the bulk whereas, τ_{turb} dominates in the bulk. Thus, it is intuitive that these stresses complement each other from the deviation of uniform (non-dimensional) unit shear stress throughout the channel.

4.3.4. TKE BUDGETS

Turbulent kinetic energy, characterized by the fluctuating velocity component is the energy associated per unit of mass in a fluid [43].

$$k = \frac{1}{2}(\langle \tilde{u}'^2 \rangle + \langle \tilde{v}'^2 \rangle + \langle \tilde{w}'^2 \rangle) \tag{4.19}$$

Naturally, regions having a high activity of turbulent fluctuations, corresponds to having a large kinetic energy. Figure 4.13 shows such behaviour.

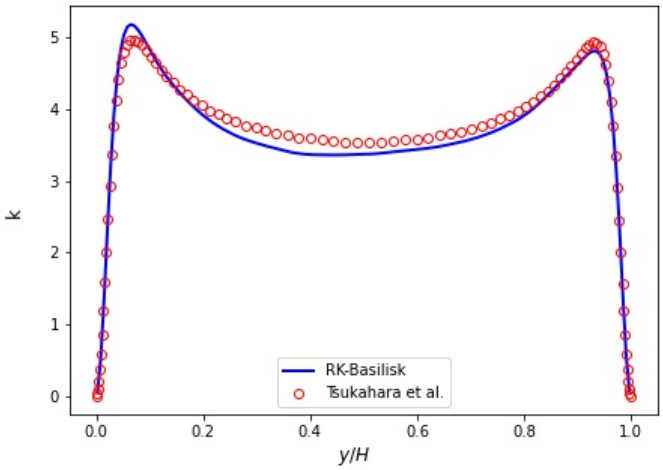

Figure 4.13: Turbulent kinetic energy contained in the flow. $y/H = 0$ is the bottom wall and $y/H = 0$ is the top wall.

Results show a good agreement with the test case except for a small under prediction near the top wall and a small over prediction at the bottom wall. The turbulent kinetic energy is dominated by the streamwise fluctuating component since the have a higher magnitude when compared to the other two directions (see Figure 4.11). Due to the presence of a bounding wall having a no slip condition influences the flow to have high gradients, which causes the kinetic energy to be high in this region. In our test case, the kinetic energy seems to be a bit higher near the bottom wall than the top wall even though both are constrained to have a no-slip condition at the walls.

An equation for the material derivative of turbulent kinetic energy can be obtained by applying a Reynolds decomposition for the NSE pre-multiplied by u_i' [41]. This results in an equation which is commonly referred to as the *Turbulent kinetic energy budget* (TKE

Budget) equation :

$$\frac{Dk}{Dt} = \underbrace{-\left\langle \tilde{u}_i' \tilde{u}_j' \right\rangle \frac{\partial \langle \tilde{u}_i \rangle}{\partial \tilde{x}_j}}_{\text{Production}} \underbrace{- \frac{1}{\rho} \frac{\partial}{\partial \tilde{x}_i} \langle \tilde{p} \tilde{u}_i' \rangle}_{\text{Press. Diffusion}} \underbrace{- \frac{1}{2} \frac{\partial}{\partial \tilde{x}_j} \left\langle \tilde{u}_i' \tilde{u}_i' \tilde{u}_j' \right\rangle}_{\text{Turb. Transport}} + \underbrace{\frac{1}{2} \nu \frac{\partial^2}{\partial \tilde{x}_j^2} \langle \tilde{u}_i' \tilde{u}_i' \rangle}_{\text{Viscous Diffusion}} \underbrace{- \nu \left\langle \frac{\partial \tilde{u}_i'}{\partial \tilde{x}_j} \frac{\partial \tilde{u}_i'}{\partial \tilde{x}_j} \right\rangle}_{\text{Dissipation}} \tag{4.20}$$

(Hereafter in this thesis, when these budget terms are abbreviated, the convention of : P, Π, T, D and ϵ is used for production, pressure diffusion, turbulent transport, viscous diffusion and dissipation respectively) It identifies the physical mechanisms which generates, transports and decay turbulence. Hence, when the flow is statistically steady, the material derivative is in equilibrium. Each one of the terms' weight indicates a gain or loss in turbulence governed by these physical mechanisms. Figure 4.14 shows the individual plots of the terms in the r.h.s of equation 4.20. The terms are shown only in the lower half of the domain since they are symmetric with the upper half. The following discussion provides a brief overview explaining about the trend shown in the respective curves.

As the name suggests, the budget of production reveals the magnitude of turbulence generated in the region of interest. Since this characterizes the generation of turbulence formed by the fluctuating components, this primarily acts as a source term due to shear. Since the mean flow in the spanwise and the normal direction is negligible, the mean velocity gradient in those direction is zero, and thus the production of turbulence is purely identified by

$$P_k = -\langle \tilde{u}' \tilde{v}' \rangle \frac{\partial \langle \tilde{u} \rangle}{\partial \tilde{y}}$$

The previous section showed the behaviour of the turbulent shear stress and the viscous stress. As we see that the production term being a product of the mean streamwise gradient and turbulent shear stress indicates that the turbulence generation is purely because of the stresses in the fluid. Figure 4.14 (a) shows the budget of production of turbulence. A very good agreement is obtained with the reference case. Due to high velocity gradients and high turbulent shear imposed by the walls, generation of turbulence is localised in the near-wall region. Considering this, and from examining the graph, it is conclusive that the stress in the bulk region supplies more kinetic energy towards the wall. Or in other words, production of turbulence is due to the extraction of kinetic energy from the mean flow [41]. Due to a non-zero shear stress as seen from the previous section, Figure 4.14 (a) also shows a non-zero production at the bulk region of the flow.

Figures 4.14 (b), (c) and (d) together represent the diffusion in turbulence. The effective mixing leads to turbulence being transported anisotropically. The budgets of diffusion is comprised due to pressure, viscous effects and transport by velocity fluctuations. These terms have a divergence form and is mainly responsible for redistribution of turbulent kinetic energy. Among the three contributors, the transport due to pressure has lowest magnitude. But the pressure diffusion is known to be the main contributor to redistribute teh energy from the normal components to the homogeneous components

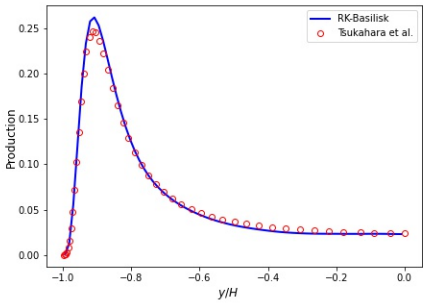

(a)

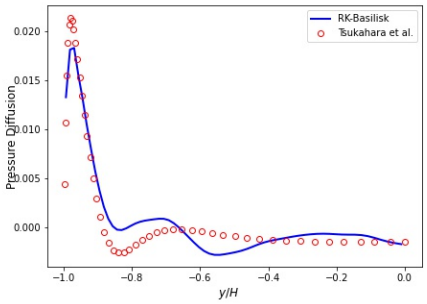

(b)

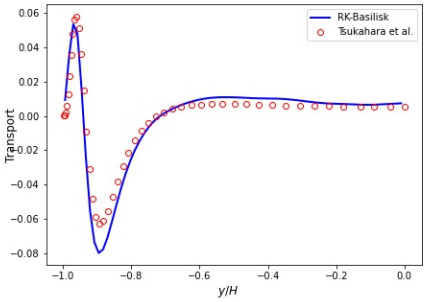

(c)

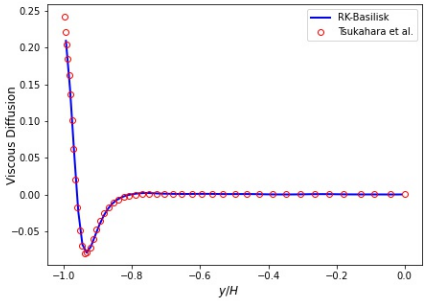

(d)

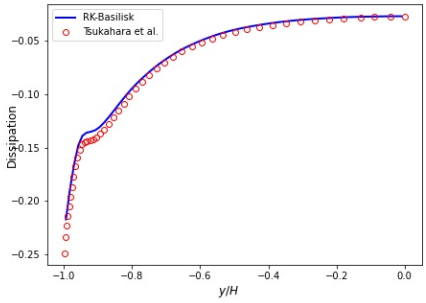

(e)

Figure 4.14: Individual terms in the budget equation 4.20 for **(a)** Production **(b)** Pressure diffusion **(c)** Turbulent transport **(d)** Viscous diffusion **(e)** Dissipation. Solid blue lines represent the computed terms from the test case, compared against red marker points from [56].

[14]. Results alternate between a small under prediction and over prediction. This might be due to the fact that the lower order FVM methods does not perform the best to predict such small variations in the pressure fluctuations. The transport on the other hand is a higher order statistic due to the triple product of velocity fluctuations. In the bulk of the flow, we almost have a zero transport, but towards the walls, the transport has two peaks, partly contributing to both gain and loss in TKE.

Transport due to viscosity has the highest magnitude among the 3 transport terms. In the bulk region, the viscous transport is zero, but has the highest variation near the wall region. Initially there were problems in predicting the viscous diffusion at the top wall, which showed over predicted values. The second derivates of scalar fields constituting the viscous diffusion is computed by finite difference operators from locally averaged velocity fields in a given time interval as seen from section 4.3.1. Boundary conditions were for the computation of these scalar gradient fields. Although setting the appropriate boundary conditions, the diffusion value showed much higher values than expected. To rectify this, the profiles of these averaged velocity fields were extrapolated to fit in the correct boundary conditions. Yet they over predicted the values at the wall. Finally, by trial and error, a small number (typically in the order of $1e-3$) was multiplied with the actual boundary condition and seemed to be a temporary fix, making it a very sensitive boundary condition. This still remains as an open question as to why such a sensitive boundary condition leads to the correct prediction in the diffusion values.

Dissipation represents the loss or decay in turbulence inside the channel. It is always negative and thus acts as a sink. Figure 4.14 (e) shows the dissipation in this Couette flow. Near the wall, we see that it has a negative peak, meaning most of the turbulence produced is equally destroyed at the walls, balancing the TKE in the channel. Theoretically $P \approx D$, but practically in internal flows, it is always reported that they do not balance each other [17] [56].

Figure 4.15 shows the individual terms of the budgets combined together represented in a single scale. They are again showed only for the lower half of the domain due to the symmetricity. Budgets in our test case is in very good accordance with the reference case from [56]. Near the viscous region $y^+ < 15$, the budgets become important. But away from the the log region and throughout the core of the flow, these terms have a constant non-zero value due to a non-zero constant shear stress. Generally it is seen that the turbulent kinetic energy produced at the walls extracts (by transport due to pressure, velocity fluctuations and viscosity) energy from the mean flow and dissipates at the wall to maintain equilibrium. As we move from the bulk towards the wall, the production term has a peak value of approximately 0.25 in non-dimensional units and constitutes the highest budget. From equation 4.20, we see that production is one of the terms which does not scale with the viscosity. Hence, the production in an internal shear driven turbulent flow is independent of Reynolds number, and thus $P_k \approx 0.25$ as $Re \rightarrow \infty$. We see that large scale production is not exactly balanced by dissipation in this Couette flow. The dissipation seems to have a higher value than production. As dissipation scales with viscosity (see equation 4.20), we can say that the flow belongs to a low Re and a high

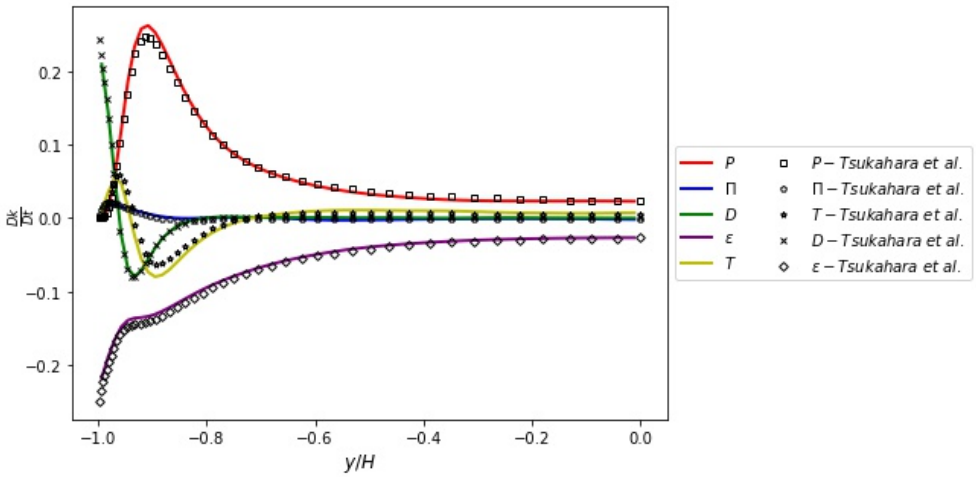

Figure 4.15: Budgets of the turbulent kinetic energy. Solid lines show the computations from the test case. The values are compared against the chose literature [56], represented in shapes.

viscous regime. As a cause, turbulence decays more, leading to quicker energy cascades. More of kinetic energy seems to be converted as heat or into internal energy.

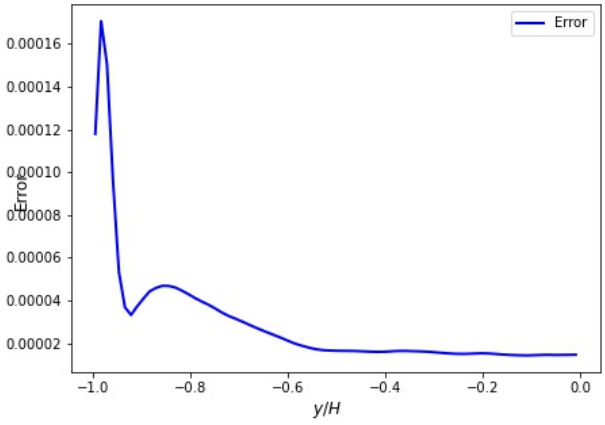

Figure 4.16: Error in computations of budget terms

Figure 4.16 shows the error in computations of the budget terms. Theoretically, the sum of the budget terms should balance the material derivative of the turbulent kinetic energy, which in principle is zero. But we see that there is a very small error which leads to a non-zero value near walls. [41] discusses that it is quite difficult to achieve the equi-

librium relationship between the budgets and the material derivative. As dissipation scales with viscosity, much smaller scales called the 'Taylor micro-scales' are necessary to fully resolve the dissipation in the same order of magnitude of dissipation. Another causality might be due to the lower order FVM functions which introduces approximation errors of the derivatives leading to small errors as observed in the figure. To overcome this, spectral methods are chosen which uses higher order functions to solve the equations in a Fourier space and is known to do well for simulations involving turbulence [14] [17].

5

CO-CURRENT STRATIFIED FLOW

Following the strategies and ideas introduced in the previous chapter, they are adopted and extended to the two-phase problem. Although this required additional modelling effort, the result seemed to be in good agreement with the chosen reference case. Before approaching the canonical problem, a brief literature survey on the common strategies to solve the air-water coupling is discussed. Further sections give a detailed picture of the numerical methods, a new strategy on the mathematical modelling of air-water coupling, meshing and finally the results.

The groups of [64] and [14] solve a stratified air-water coupled flow subjected to very small deformations of the interface. They simulate a flow for $Re_\tau \approx 170$ (for both the phases), driven by a pressure gradient and emulating a domain with infinite depth. Higher-order schemes were such as pseudospectral methods were used to solve the equations of momentum and mass. Following [14], [64] solve the two domains separately with a fractional iteration alternating between the two domains. Air and water motions are coupled with continuity of velocity, tangential and normal stress balance. The interface motion is computed by solving the pure advection equation and with the 'Boundary fitting coordinates (BFC)' method. BFC has been gaining a lot of attention in solving deforming interface topologies. This has been reported to perform similar to the other numerical methods such as FDM/FVM, although fails when subjected to strong changes in topology [29].

A coupled air-water shear driven co-current flow was solved by the group of [30]. A pseudospectral method along with the second-order Runge-Kutta method were the numerical methods adopted to solve the equations. The flat interface was coupled via the continuity of shear and velocity. Following the work of[32], [31] used the same numerical strategies to solve a co-current Couette air-water flow for a flat interface. This work done, was the first to simulate both the phases with their respective scales.

A common methodology called the 'fractional time step iteration' was used to solve

the air-water motions in almost all of the above works discussed. The idea behind this is to decouple the air and water motions and to solve them separately, treating them as two different domains coupled at the interface. The top boundary of water domain and bottom boundary of air domain locally serve as the interface and they are coupled by the interfacial conditions. For the first fractional half of the time step, air side motions are solved subject to the velocity at the top boundary of the water domain, satisfying the continuity of velocity. Similarly, for the next half of the fraction, water side motions are solved subject to the shear stress provided by the bottom boundary of air side, satisfying the continuity of shear stress. Hence, the air-water motions are solved alternatively in a given time step until the flow becomes statistically steady.

The work of [31] particularly stands out due to the fact that they solve the motions in the respective scales of air and water, which surprisingly has not been reported in any of the previously mentioned works of [32],[14]. When true air-water ratios are used, the difference in the densities and viscosities lead to the Reynolds number of both the phases being coupled by a factor (see equation 5.4). Thus, the velocity and shear continuity just across the interface leads to two different spatial and temporal scales, where air side motions are much faster than the water side [31]. Moreover, by using realistic air-to-water ratios which inherently leads to two different Reynolds number across the phases, opens the problem to a more realistic scenario, which are typically seen in nuclear applications. Therefore, it should be interesting to model the system with two scales and validate the results against this literature, [31] and finally highlighting the effects seen with such choices of air-water parameters.

Unfortunately, at the moment RK-Basilisk does not offer to solve the problem with the fractional iteration method. Of course it could be developed, but would take an appreciable amount of time and also would make the goals of this thesis out of scope. Thus, right now we are constrained to solve the problem without decoupling the phases to apply a fractional iteration scheme, but to solve it 'together' as one single system. This already knocks out the possibility of having two different temporal scales as the air and water system (which originally will have different temporal scales) 'should' be solved together.

5.1. NUMERICAL METHODS

This section provides a detailed idea behind the numerical methods implemented to solve the two-phase stratified Couette Flow configuration. Firstly, the problem and the equations responsible for the multiphase system including additional conditions that need to met at the interface is explained. This is followed by a short discussion of the numerical methods adopted to solve the system. But unlike the reference case, we wish to solve the problem without a fractional time step iteration scheme, i.e., solving the system together, but with different scalings. We see that the numerical methods when constrained (explained in the upcoming paragraphs) is not straightforward, and the additional numerical strategies which are adopted are carefully explained.

We consider a co-current air-water flow driven purely by shear. This shear is imposed by imposing a finite velocity U_w at the top wall, which is separated from a bottom plate distanced at $2H$ kept stationary, where H is the half-height for the entire domain, ref Fig. 5.1. To avoid any external forcing, there is neither a gravitational force, nor a pressure gradient added to the system. Due to the density difference and to keep it physical, air is simulated in the upper half and water in the lower half of the domain. We assume and thereby model to have no wavy effects at the interface, hence maintaining a flat interface. This means that we have high gravity and/or surface tension. We have u, v and w as the streamwise, normal and spanwise components of velocity with x, y and z as the reference axes with the interface being located at the origin. The equations governing the multiphase fluid system is the Navier-Stokes equation :

$$\begin{aligned} \frac{\partial \rho u_i}{\partial t} + \frac{\partial (\rho u_i u_j)}{\partial x_j} &= -\frac{\partial p}{\partial x_i} + \mu \frac{\partial^2 u_i}{\partial x_i \partial x_j} \\ \frac{\partial u_i}{\partial x_i} &= 0 \end{aligned} \tag{5.1}$$

where, $\rho = \rho^* f + (1-f)\rho^\dagger$ and $\mu = \mu^* f + (1-f)\mu^\dagger$ are the variable densities and kinematic viscosities responsible for each phase ($*$ for air and $\dagger$ for water) based on the phase fraction f. u_i can be written as (u, v, w) indicating the three components of velocity with i being the direction along each of the reference axes.

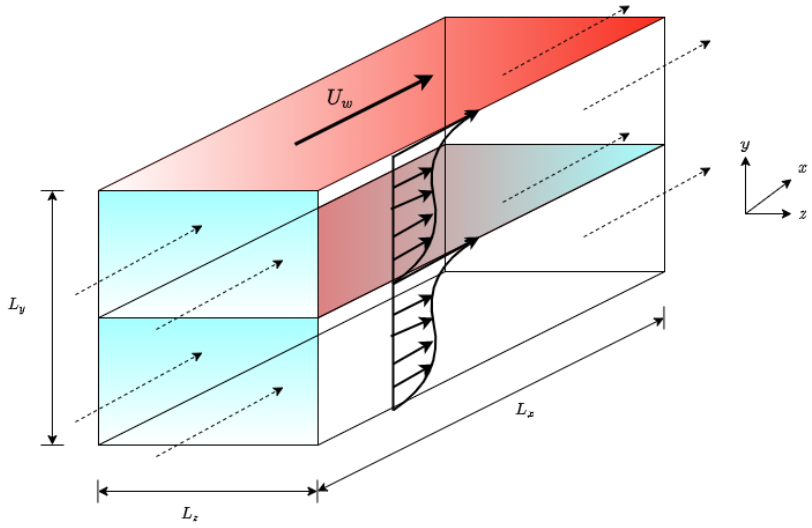

Figure 5.1: The computational domain and the physical problem simulated

This along with the interface advection equation solves the two-phase problem with an actual multiphase modelling technique, such as the VoF method. But we wish to solve the two-phase problem without any of the interface modelling technique, therefore also

closely working around the concepts built in [31]. Using VoF or any other method makes sense if we have a non-stationary interface for which the wavy motion has to be captured accurately or when we have to resolve interfaces of complex topologies. But this is disregarded simply due to the fact that we assume and thereby solve for a flat interface throughout the simulation in $[0, T]$. Therefore it is inadequate to solve the VoF advection equation as it would just increase the computational cost of the overall problem. Hence, there is a need to replace this by additional conditions which has the characteristics of a stratified interface separating both the domains.

As long as there is absence of mass transfer across a fluid-fluid interface, the velocities at the interface are continuous [52]. This vector condition of velocity is analogous to a no-slip condition. This is given by the equation 5.2. If either velocity continuity or just shear continuity is specified, the problem becomes ill-posed [53]. Since we have two unknown velocity fields (air and water), we need twice as many as equations to close to problem. If we assume the interface to have infinitesimal thickness, from the equilibrium of forces, we can write a condition based on the stress acting on that face [52]. This is given by equation 5.3. :

$$u_i^a = u_i^w \qquad i = 1,2,3 \tag{5.2}$$

$$\mu_a \frac{\partial u_j^a}{\partial x_i} = \mu_w \frac{\partial u_j^w}{\partial x_i} \qquad j = 1,3 \tag{5.3}$$

where μ_a and μ_w are the dynamic viscosities of air and water respectively and also tabulated along with other flow properties in Table 5.1. One immediate solution should be that the vertical component of the velocity condition at the interface should be zero, since we assume to have a flat interface.

Fluid	Density	Kinematic Viscosity	Dynamic Viscosity
	ρ	ν	μ
Water	998	1.14×10^{-6}	1.14×10^{-3}
Air	1.205	1.45×10^{-5}	1.75×10^{-5}
Water-Air ratio	828.21	7.86×10^{-2}	65.1

Table 5.1: Fluid properties at 20°C and 1 atm.

Other than these interfacial conditions, periodic boundary conditions are applied in the streamwise and the spanwise directions. Simulations are performed in a domain which has a size $L_x \times L_y \times L_z = (2\pi H \times 2H \times \pi H)$, where H is the half height. The equations of motion are discretized based on the second order finite volume method. A central difference operator has been used to discretize the convection term. The equations are then integrated in time with the 3-stage Runge-Kutta method. To ensure convergence, a CFL = 0.4 was chosen.

Before proceeding to the rest of the details, some constraints and problems related to the implementation of the aforementioned model is briefly summarized.

- As mentioned earlier, the main constraint posed by (RK-)Basilisk is the unavailability of the fractional time step solver. Due to this, the air and water system cannot be decoupled to be solved in alternative fractional time step. Thus, we are forced to solve a coupled system together with the same temporal scales.

- Since $\mu_a \ll \mu_w$ ($\mu_w = 65.1\mu_a$) water phase has more inertia when compared to the air phase. Thus, gradients and motions in the air side would be much larger when compared to the water side. The interface velocity U_i would be much smaller than the top wall velocity U_w [31]. This leads to the fact that, air side motions require a much smaller time step than the water side to resolve the quick motions. Solving the equations 'together' on a continuous setting with the parameters specified in Table 5.1 crashed the simulation. This is due to the reason mentioned above. Thus, the solver, trying to resolve the coupled motions at the interface, typically marched to time steps in the magnitude of $1e-10$, which caused the simulation to diverge.

- Next issue is basically a conjuction of the above two reasons. When the system is solved together, computing gradients at the interface will involve, say velocities, of two different scales i.e, velocities in units of water and units of air. As this is already undesirable for the computation of the solution variable(s), also will have unphysical gradients for the averaged quantities which leads to incorrect computation of budget terms.

Considering these issues, we need to come up with a strategy to firstly solve the problem together (coupled) by preserving the nature of numerical gradients at the interface. Thus, in the next section, we see how this problem is tackled and overcome by developing certain numerical strategies which locally (at the interface) modifies certain terms of the Navier-Stokes equations in order to comply with respective scalings and working through the constraints mentioned above.

5.2. MATHEMATICAL MODELLING OF THE INTERFACE COUPLING

As mentioned earlier, we wish to simulate the problem in two different scales. These two different scales arise purely by using true air-water ratios of flow parameters. We see from [31] that,

$$Re_\tau^a = \sqrt{\frac{\rho_w}{\rho_a}}\frac{\nu_w}{\nu_a} Re_\tau^w = \sqrt{\frac{\rho_a}{\rho_w}}\frac{\mu_w}{\mu_a} Re_\tau^w = 2.26 Re_\tau^w \tag{5.4}$$

Hence, from a continuous dimensional NSE, we could move to using a non-dimensional form of NSE to simulate to different scales of the problem. Previously we had μ and ρ varying across the interface to define a stratified multiphase problem (equation 5.1). In the non-dimensional counterpart, we just have a Re_τ which acts as a flow parameter as also seen in the previous chapter. Hence for the non-dimensional two-phase NSE, we

just have Re_τ which varies across each phase. Since we assume to have a flat interface, we can define :

$$Re_\tau(\mathbf{x}) = \begin{cases} Re_\tau^a & \text{if} \quad y > y_{int} \\ Re_\tau^w & \text{if} \quad y < y_{int} \end{cases} \tag{5.5}$$

where y_{int} is the ordinate along which the interface is located. Thus we could re-write the NSE as :

$$\begin{aligned} \frac{\partial \tilde{u}_i}{\partial \tilde{t}} + \frac{\partial \tilde{u}_i \tilde{u}_j}{\partial \tilde{x}_j} &= -\frac{\partial \tilde{p}}{\partial \tilde{x}_i} + \frac{1}{Re_\tau(\mathbf{x})} \frac{\partial^2 \tilde{u}_i}{\partial \tilde{x}_j^2} \\ \frac{\partial \tilde{u}_i}{\partial \tilde{x}_i} &= 0 \end{aligned} \tag{5.6}$$

which is the equation solved by RK-Basilisk.

Usually a non-dimensionalisation with a u_τ and H, leads to the coefficient of the viscous term having a frictional based Reynolds number (also seen in the previous chapter). By using two different frictional Reynolds numbers - Re_τ^a and Re_τ^w, it is presumed that we introduced non-dimensionalisation based on two frictional reference velocities, u_τ^a and u_τ^w each for one domain. Although this is physically not true nor allowed, but it is written so that it is easy to distinguish, identify and label the phases.

Simulations are performed for the same frictional Reynolds numbers as mentioned in [31]. The respective air side and the water side frictional Reynolds numbers are : $Re_\tau^w = 120$ and $Re_\tau^a = 2.26 Re_\tau^w = 271$. In the previous section, it was indicated that the solver faces difficulties when the problem is solved with the actual physical parameters. This was due to the large ratio of the physical viscosities. This is potentially overcome by simulating a non-dimensional Navier-Stokes equations. This is because of the difference in the ratio of the coefficient of the viscous term. Now, these coefficients are non-dimensional viscosities, denoted by $\mu^* = \frac{1}{Re_\tau^a}$ and $\mu^\dagger = \frac{1}{Re_\tau^w}$. The ratio of $\frac{\mu^\dagger}{\mu^*} \ll \frac{\mu_w}{\mu_a}$. Hence, by still having two different scales, we avoid a huge computational inefficiency.

Thus we aim to solve the stratified two-phase problem together as a whole system, but as if we had two single-phase problem with this it's respective units, coupled at the interface. This basically combines the idea of two different scalings from the reference literature, but solves with the constraint (the fact that we can't adapt to a factional iteration scheme) posed by RK-Basilisk. Now that certain ideas are established, we can break down the equation solved by RK-Basilisk (equation. 5.6) to represent two different scales.

$$\begin{aligned} \frac{\partial u_i^*}{\partial t} + \frac{\partial u_i^* u_j^*}{\partial x_j} &= -\frac{\partial p^*}{\partial x_i} + \frac{1}{Re_\tau^a} \frac{\partial^2 u_i^*}{\partial x_j^2} \\ \frac{\partial u_i^*}{\partial x_i} &= 0 \end{aligned} \tag{5.7}$$

and

$$\frac{\partial u_i^\dagger}{\partial t} + \frac{\partial u_i^\dagger u_j^\dagger}{\partial x_j} = -\frac{\partial p^\dagger}{\partial x_i} + \frac{1}{Re_\tau^w}\frac{\partial^2 u_i^\dagger}{\partial x_j^2}$$
$$\frac{\partial u_i^\dagger}{\partial x_i} = 0 \tag{5.8}$$

where $'*'$ represents the scaled units in air and $'\dagger'$ represents the scaled units in water. All the 'tildes' have been dropped since $*$ and $\dagger$ already represent units in non-dimension scales.

At the interface, there are a few other reconstructions that are required too. Due to the constraint of solving the problem 'together', the gradients computed just at the interface will involve velocities in different scales (also mentioned earlier). Since we have to solve 'coupled system' as 'two single-phase flows', we need to re-scale the velocities belonging to the gradients/fluxes at the interface so that the re-scaled fluxes have the units of the phase which it belongs to. This is especially required for the diffusion term in the NSE since they lead to incorrect fluxes unless re-scaled. Apart from this reason, due to the fact that we want to solve it as two single-phase flows, there are other fluid-fluid boundary conditions that are need to be satisfied for the convection and the pressure terms. They are altogether discussed in the upcoming paragraphs.

5.2.1. CONVECTIVE FLUXES

From the interfacial conditions (equation 5.2), we know that the velocity at the interface should be continuous. The following discussion takes the concepts from interface modelling method to explain a certain behaviour of velocity component at the interface [52]. The interface motion could be expressed by :

$$\frac{\partial F}{\partial t} + \mathbf{u}\cdot\nabla F = \frac{dF}{dt} = 0 \tag{5.9}$$

for which the unit normal could be defined by $\mathbf{n} = \frac{\nabla F}{|\nabla F|}$ and hence, the normal component at the velocity at the interface by, $\mathbf{u}\cdot\nabla\mathbf{F} = \mathbf{u}\cdot\mathbf{n}|\nabla F|$. For a system with flat interface separating air and water, the kinematic condition at this gas-liquid interface can be written as:

$$\mathbf{u_a}\cdot\mathbf{n} = \mathbf{u_w}\cdot\mathbf{n} = -\frac{1}{|\nabla F|}\frac{\partial F}{\partial t} \tag{5.10}$$

If we require the interface to be flat and also need it to be stationary, we would have $\frac{\partial F}{\partial t} = 0$. Hence, the continuity condition for the normal component reduces to:

$$\mathbf{u_a}\cdot\mathbf{n} = \mathbf{u_w}\cdot\mathbf{n} = 0 \tag{5.11}$$

But when we simulate the problem together, the interface is located at the faces shared between the air cells and the water cells. Hence, we need a face velocity or a flux condition which sets the face velocity at the interface to be zero. This can simply be

derived from the convective term of the NSE.

The convective acceleration due to a fluid velocity **u** is:

$$\frac{\partial u_i^* u_j^*}{\partial x_j}$$

and

$$\frac{\partial u_i^\dagger u_j^\dagger}{\partial x_j}$$

We begin by integrating this acceleration term over a control volume V. Using the Gauss divergence theorem, we can replace the volume integrals by surface integrals :

$$\begin{aligned}\frac{1}{V^*}\int_V \frac{\partial u_i^* u_j^*}{\partial x_j} &= \frac{1}{V^*}\int (u_i^* \cdot n) u_j^* \cdot dA \\ &= \sum_{f\sim \text{faces(V)}} \left(\int_f (u_i^* \cdot n) u_j^* \cdot dA\right)\end{aligned}$$

and

$$\begin{aligned}\frac{1}{V^\dagger}\int_V \frac{\partial u_i^\dagger u_j^\dagger}{\partial x_j} &= \frac{1}{V^\dagger}\int (u_i^\dagger \cdot n) u_j^\dagger \cdot dA \\ &= \sum_{f\sim \text{faces(V)}} \left(\int_f (u_i^\dagger \cdot n) u_j^\dagger \cdot dA\right)\end{aligned}$$

It is clear that we integrate over all of the faces over a control volume ∂V, but right at the interface, there is exactly one face. Since we do not want any convective transfer across the interface, the flux normal to the interface is set to zero. Hence,

$$(u_i^* \cdot n)\big|_{f_{int}} = 0 \tag{5.12}$$

and

$$(u_i^\dagger \cdot n)\Big|_{f_{int}} = 0 \tag{5.13}$$

Although they are represented in two different scales, the problem RK-Basilisk solves just has one face. So, we just the convective flux $(\tilde{u}\cdot n)|_{f_{int}}$, where $\tilde{u}$ represents a general non-dimensional velocity.

5.2.2. PRESSURE GRADIENT

Earlier it was discussed that the each of the phases are scaled differently because of the difference in the non-dimensional viscosity responsible for each of the phase. Upon non-dimensionalisation based on the respective shear velocity, u_τ and the domain height, H, we see that (note that the itldes are used to give a general idea of non-dimensional quantities here, but not with resepect to each scaling)

$$-\frac{\partial p}{\partial x_i} = -\frac{\partial \tilde{p}}{\partial \tilde{x}_i}\frac{\rho}{H}u_\tau^2$$

Hence the the pressure gradient $\frac{\partial \tilde{p}}{\partial \tilde{x}}$ has a different definitions at the interface, or simply been scaled in units based on the shear different shear velocities.

Careful attention must be paid in order to ensure careful predictions of the variables and the gradients at the interface. To derive a correct boundary condition for pressure, we start from the momentum equation. Since an adjustment is required only for $\nabla_y p$, the (unscaled) y-momentum equation is reduced in order to derive an appropriate pressure boundary condition. This derivation should be analogous for each of the phase. We have :

$$\frac{\partial \tilde{v}}{\partial \tilde{t}} + \frac{\partial \tilde{v}\tilde{u}_j}{\partial \tilde{x}_j} = -\frac{\partial \tilde{p}}{\partial \tilde{y}} + \frac{1}{Re_\tau}\frac{\partial^2 \tilde{v}}{\partial \tilde{x}_j^2} \tag{5.14}$$

We have an incompressible flow between a well defined boundary, with constant height, H. Assuming steady flow (from the perspective of single-phase flow) which has a constant flow rate, we can assume that the flow is planar. In this case, velocity vector will be just a function of y, the gradients in the homogeneous (streamwise and spanwise) directions are almost negligible. Hence,

$$\tilde{v} = \tilde{v}(y)$$

At the lower boundary, since we have a no-slip condition $v(y = 0) = 0$. As known from the previous section, since we impose the flux normal to the boundary to be zero, which inherently is the interface velocity, $v(y_{int}) = 0$. And we have the incompressiblity constraint,

$$\frac{\partial \tilde{u}_i}{\partial x_i} = \frac{\partial \tilde{u}}{\partial x} + \frac{\partial \tilde{v}}{\partial y} + \frac{\partial \tilde{w}}{\partial z}$$

As discussed, the velocity gradients in the homogeneous directions are negligible. Hence, we see that the incompressibility constraint reduces to

$$\frac{\partial \tilde{u}_i}{\partial x_i} = \frac{\partial \tilde{v}}{\partial y} = 0$$

Hence, we see that $v(y)$ = constant at all heights. The y-momentum equation reduces to the pressure gradient balancing the viscous terms,

$$\frac{\partial \tilde{p}}{\partial y} = \frac{1}{Re_\tau}\frac{\partial}{\partial y}\left(\frac{\partial \tilde{v}}{\partial y}\right)$$

Since we see that the gradient $\vec{\nabla}_y v$ reduces to zero at the interface, we have

$$\left.\frac{\partial \tilde{p}}{\partial y}\right|_{int} = 0 \tag{5.15}$$

Upon close examination, we see that condition is what we exactly impose at walls when simulating single-phase wall bounded flows. Hence this makes sense, since we basically aim to solve two-phase problem as if we had two-single-phase problems. This Neumann pressure condition 'naturally' occurs as a part of the NSE and it is quite typical to use a homogeneous Neumann pressure condition at walls, in order for the flow to freely develop.

5.2.3. DIFFUSION FLUX

Similar to the pressure term, having a non-zero gradient across the interface, a certain non-zero momentum flux exists across the interface. Since these fluxes have a gradient term in the definition, these account for velocities from two different phases. This in particular is an important term to be correctly imposed at the interface since diffusion characterizes turbulence overall, hence directly affecting the budgets of turbulence. This suggests that, the diffusion term needs to be replaced too, appropriately, subject to few scalings required for the fluxes from each of the phase to have it's own units, which is shown in the upcoming discussion.

The main idea is to replace the incorrect diffusive fluxes at the interface by a corrector flux, $\mathscr{D}^c$. The incorrect fluxes are first removed from the discrete system by setting the coefficient of the flux, $\mu^+ = 0$ (non dimensional viscosity coefficient, $mu^+ = \frac{1}{Re_\tau}$). Since we aim to treat it as two different flows, a finite volume discretization process is adapted to arrive at the appropriate fluxes from each of the phases. It should be noted that, when re-writing the fluxes, the gradients involve velocities from other phase as well. Hence, a "scaling correction", $\mathscr{S}$ is used to re-scale the velocities so that the fluxes will have the units of the phase to which it belongs to. In particular, the air-phase velocity in the water-phase flux should be rescaled to the units of water and vice-versa. This is scaling parameter is developed from the coupling conditions elaborated in the following.

We start with the finite volume discretization of the dimensional viscous term in the NSE:

$$\begin{aligned}\mathscr{D} &= \frac{\mu^+}{\tilde{V}} \int_{\tilde{V}} \tilde{\nabla} \cdot \tilde{\nabla} \tilde{u} d\tilde{V} \\ &= \frac{\mu^+}{\tilde{V}} \int_{\tilde{V}} \frac{\partial}{\partial \tilde{x}_i} \left(\frac{\partial \tilde{u}_j}{\partial \tilde{x}_i} \right) d\tilde{V}\end{aligned}$$

From Gauss' divergence theorem, we have

$$\int_V \nabla \cdot F dV = \int_A F \cdot \mathbf{n} dA$$

Hence, we convert the volume integrals to surface integrals

$$\begin{aligned}\frac{\mu^+}{V} \int_{\tilde{V}} \frac{\partial}{\partial \tilde{x}_i} \left(\frac{\partial \tilde{u}_j}{\partial \tilde{x}_i} \right) d\tilde{V} &= \frac{\mu^+}{\tilde{V}} \int_{\tilde{A}} \frac{\partial \tilde{u}_j}{\partial \tilde{x}_i} \cdot \mathbf{n}_{f,i} d\tilde{A} \\ &= \frac{\mu^+}{\tilde{V}} \sum_{f \sim faces(V)} \frac{\partial \tilde{u}_j}{\partial \tilde{x}_i} \cdot \mathbf{n}_{f,i} d\tilde{A}\end{aligned}$$

This,

$$\mathscr{D}^c = \frac{\mu^+}{\tilde{V}} \sum_f \left. \frac{\partial \tilde{u}_j}{\partial x_i} \right|_f \cdot \mathbf{n}_{f,i} d\tilde{A}$$

exactly is the corrector (non-dimensional) momentum flux that needs to be added at the interface.

As we see from the 5.2, the missing fluxes are along the interface and the face is shared by two cells, one from the air phase and the other from the water phase. As the control volume shares just one face, we can be more specific with the notation. Air cell shares the south face and water cell shares the north face. Hence, we could denote the respective fluxes as $\mathscr{D}^c|_{a,s}$ and $\mathscr{D}^c|_{w,n}$. As it was already mentioned that we intend to solve from the perspective of single-phase flows, the interface "acts" as a "boundary" for each of the phases. Since these share a common face, an interface velocity, $\tilde{u}^{int}$ is used in the definition of the gradients in the fluxes.

$$\mathscr{D}^c\big|_{a,s} = \frac{\mu^*}{V}\left(\frac{u_j^* - u_{j,int}^*}{\Delta/2}\right)\cdot\mathbf{n}A_f$$
$$\mathscr{D}^c\big|_{w,n} = \frac{\mu^\dagger}{V}\left(\frac{u_{j,int}^\dagger - u_j^\dagger}{\Delta/2}\right)\cdot\mathbf{n}A_f$$

with Δ being cell center to cell center distance, $\mathbf{n}$ being the outward normal and A_f being the area of the face. It should be noted that, now these fluxes are defined in it's own units, i.e, in units of air and water. Hence, the interface velocity, $\tilde{u}_{j,int}^*$ in units of air and $\tilde{u}_{j,int}^\dagger$ in units of water. In the last paragraphs, it was mentioned that the gradients require information from the other phases and due to this, re-scaling is necessary. But it was just shown that we define gradients with an interface velocity, but this ambiguity will be resolved, once when we see that the interface velocity is simply but an weighted average of the (re-scaled) velocities from each of the phases, interpolated at the face.

A definition for the non-dimensional scaled interfacial velocities are not readily available. From the continuity of shear and velocity at the boundary, we arrive at an expression for an interfacial velocity first and then respective non-dimensional interface velocities are developed.

Shear stresses are continuous at the interface. Note that the following are in dimen-

sional units

$$\begin{aligned}
\tau_a &= \tau_w \\
\mu_a \frac{\partial u_j^a}{\partial y} &= \mu_w \frac{\partial u_j^w}{\partial y} \\
\mu_a \frac{u_j^a - u_j^{int}}{\Delta/2} &= \mu_w \frac{u_j^{int} - u_j^w}{\Delta/2} \\
\mu_a (u_j^a - u_j^{int}) &= \mu_w (u_j^{int} - u_j^w)
\end{aligned}$$

Rearranging for the u_j^{int}, we get:

$$u_j^{int} = \frac{(\mu_a u_j^a + \mu_w u_j^w)}{(\mu_a + \mu_w)}$$

Before proceeding to the non-dimensionalisation of the interface velocity with the respective reference velocities, the scaling factor $\mathscr{S}$ is shown from [31]. We can usually define the frictional velocity as $u_\tau = \frac{\tau_0}{\rho}$. The ratio of shear velocities gives,

$$\begin{aligned}
\frac{u_\tau^a}{u_\tau^w} &= \frac{\sqrt{\frac{\tau_0}{\rho_a}}}{\sqrt{\frac{\tau_0}{\rho_a}}} \\
&= \sqrt{\frac{\rho_w}{\rho_a}} \\
&= 28.8 \\
&= \mathscr{S}
\end{aligned}$$

This makes sense because, the shear stress is continuous at the interface, this scaling factor, which essentially is the ratio of the frictional velocities, brings out the disparity in both the phases due to the large density difference. This gives us a qualitative hint that the air-side non-dimensionalised velocities just near the interface would be much lower than the water side velocities.

Using this, the air phase interface velocity can be non-dimensionalised by u_τ^a, as:

$$\frac{u_j^{int}}{u_\tau^a} = \frac{(\mu_a \frac{u_j^a}{u_\tau^a} + \mu_w \frac{u_j^w}{u_\tau^a})}{(\mu_a + \mu_w)}$$

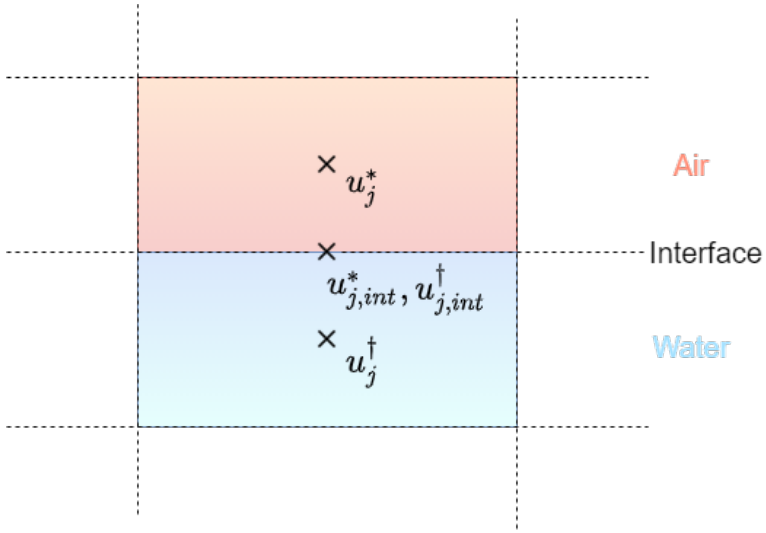

Figure 5.2: Cells above and below the interface belonging to the the air-phase and water-phase respectively. The interface velocities in units of $*$ and † are computed by interpolation of u_j^* and $u_j^\dagger$

Using the previous derived Scaling factor $\mathscr{S}$, we can write

$$\frac{u_j^{int}}{u_\tau^a} = \frac{(\mu_a \frac{u_j^a}{u_\tau^a} + \mu_w \frac{u_j^w}{\mathscr{S} u_\tau^w})}{(\mu_a + \mu_w)}$$
$$u_{j,int}^* = \frac{(\mu_a u_j^* + \mu_w u_j^\dagger / \mathscr{S})}{(\mu_a + \mu_w)}$$

gives the non-dimensionalised interface velocity in units of air.

Similarly, using the same scaling factor, a non-dimensionalised interface velocity can be obtained by using u_τ^w as the reference velocity, :

$$\frac{u_j^{int}}{u_\tau^w} = \frac{(\mu_a \frac{u_j^a}{u_\tau^w} + \mu_w \frac{u_j^w}{u_\tau^w})}{(\mu_a + \mu_w)}$$
$$\frac{u_j^{int}}{u_\tau^w} = \frac{(\mu_a \frac{u_j^a}{u_\tau^a / \mathscr{S}} + \mu_w \frac{u_j^w}{u_\tau^w})}{(\mu_a + \mu_w)}$$
$$u_{j,int}^\dagger = \frac{(\mu_a \mathscr{S} u_j^* + \mu_w u_j^\dagger)}{(\mu_a + \mu_w)}$$

gives the non-dimensionalised interface velocity in units of water.

It was previously hinted that, at the interface the motions will be lower in the air side, than in water. Looking at the interfacial velocity, this being non-dimensionalised with it's friction velocity and knowing that $u_\tau^a \gg u_\tau^w$, we see that the $u^*_{j,int} \ll u^\dagger_{j,int}$.

These definitions $u^*_{j,int}$ and $u^\dagger_{j,int}$ are finally used to now fully define the required corrector flux from the faces at the interface. Hence,

$$\mathscr{D}^c\big|_{a,s} = \frac{\mu^*}{V}\left(\frac{\frac{(\mu_a u_j^* + \mu_w u_j^\dagger/\mathscr{S})}{(\mu_a+\mu_w)} - u_j^*}{\Delta/2}\right)\cdot \mathbf{n}A_f$$

$$\mathscr{D}^c\big|_{w,n} = \frac{\mu^\dagger}{V}\left(\frac{\frac{(\mu_a \mathscr{S} u_j^* + \mu_w u_j^\dagger)}{(\mu_a+\mu_w)} - u_j^\dagger}{\Delta/2}\right)\cdot \mathbf{n}A_f$$

Considering the sign convention for the normals and also expanding, we have

$$\mathscr{D}^c\big|_{a,s} = \frac{\mu^*}{V}\left(\frac{\mu_a u_j^* + \mu_w u_j^* - \mu_a u_j^* - \mu_w u_j^\dagger/\mathscr{S}}{(\mu_a+\mu_w)\Delta/2}\right)A_f$$

$$\mathscr{D}^c\big|_{w,n} = \frac{\mu^\dagger}{V}\left(\frac{\mu_a u_j^* \mathscr{S} + \mu_w u_j^\dagger - \mu_a u_j^\dagger - \mu_w u_j^\dagger}{(\mu_a+\mu_w)\Delta/2}\right)A_f$$

After some rearrangement, we can finally write the corrector flux needed from each of the phases :

$$\mathscr{D}^c\big|_{a,s} = \frac{\mu^*}{V}\left[\left(\frac{\mu_w}{\mu_a+\mu_w}\right)\left(\frac{u_j^* - u_j^\dagger/\mathscr{S}}{\Delta/2}\right)\right]A_f \tag{5.16}$$

$$\mathscr{D}^c\big|_{w,n} = \frac{\mu^\dagger}{V}\left[\left(\frac{\mu_a}{\mu_a+\mu_w}\right)\left(\frac{u_j^* \mathscr{S} - u_j^\dagger}{\Delta/2}\right)\right]A_f \tag{5.17}$$

Although these fluxes could be closely compared to the original fluxes, we see that there are important and necessary differences which help to simulate the way we want. Firstly, the gradients responsible from each of the phase for the corresponding flux term require the velocity from the other phase, but now is re-scaled so that information taken from the other phase is in the units of the phase where the gradient belongs to. Secondly there is apparently a "dimensional viscosity scaling" in front of the rescaled gradients.

With this, we have successfully derived the new inertial, pressure and viscous terms at this interface. This truly enables us to simulate a two-phase stratified flow as two-single-phase flows being coupled at the interface, where each of the phase simulated has been scaled in it's own reference velocity, u_τ, thereby essentially answering/solving the third constraint specified in section 5.1.

5.3. MESHING

It is important to have a fine resolution where the flow is subjected to high gradients. Parts of the domain where these high gradients exist are near-walls. In the test case that we want to simulate, the near-interface region would also be subjected to high gradients and high shear rate. Hence, it is also important to capture the layers belonging to this region accurately. Moreover, we want to study the budgets near the interface accurately. Hence, by using the same strategy for meshing as in the previous chapter, we extend it to our two-phase scenario. For the streamwise and the spanwise directions, we stay with having homogeneous deformations and cell stretching. In the normal directions, we require a highly clustered grid near-walls and near-interface.

The main goal is to map a uniformly spaced grid, Ω_p to a non-uniform grid Ω_{nb} so as to construct a clustered grid. Firstly the same function, η (as seen in the previous chapter) is used to determine the grading factor, α based on the domain half height, H, number of cells in the normal direction, N_y and the first cell height. The grading factor then determines the cell width based on the index of the cell and the first cell width. Due to the difference in Re_τ of both the phases, they can give our two different spatial scales. Compromising on some computational efficiency, but due to simplicity, the mesh is constructed on the the y^+ values of the bigger Re_τ so that the scales of fluid having a smaller Re_τ is automatically resolved by resolving the grid with higher Re_τ. The same grading, deformations and the cell stretches are used near the interface and near the walls. Hence, the same deformation function, $\zeta : \Omega_p \rightarrow \Omega_{nb} | y_p \in \Omega_p$ and $y_{nb} \in \Omega_{nb}$ maps the uniform domain to a stretched non uniform basilisk domain. Since we typically need the same transformations in both the domains, the same functions, but adjusted accordingly could be used to construct the same deformations

$$y_{nb} = \zeta(\Delta_0, \alpha, y_0) = \begin{cases} y_0 + \sum_{i=1}^{i<Ny-1} \alpha^i \Delta_0 & y > y_{int} \\ y_0 + \sum_{i=Ny}^{i<2Ny-1} \alpha^i \Delta_0 & y < y_{int} \end{cases} \tag{5.18}$$

where the summations $\sum_{i=1}^{i<Ny-1} \alpha^i \Delta_0$ and $\sum_{i=Ny}^{i<2Ny-1} \alpha^i \Delta_0$ form a geometric progression:

$$\sum_{i=1}^{i<Ny-1} \alpha^i \Delta_0 = y_0 + \Delta_0 \left(\frac{\alpha^i - 1}{\alpha - 1} \right) \qquad (y > y_{int}) \tag{5.19}$$

and

$$\sum_{i=Ny}^{i<2Ny-1} \alpha^i \Delta_0 = y_0 + \Delta_0 \left(\frac{\alpha^i - 1}{\alpha - 1} \right) \qquad (y > y_{int}) \tag{5.20}$$

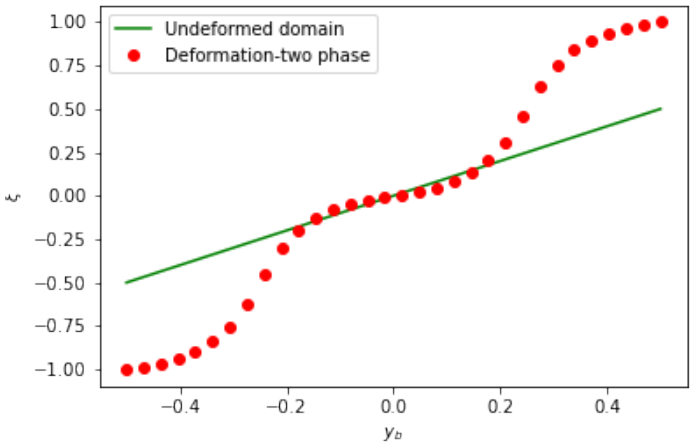

Figure 5.3: Deformation function mapping $\Omega_b \rightarrow \Omega_{nb}$

Fig. 5.3 shows the deformation of a uniform grid $\Omega_p = [-0.5, 0.5]$ transformed to a non-uniform grid $\Omega_{nb} = [-1, 1]$. A grading factor of $\alpha = 1.195581$ was determined and the normal coordinates were determined which is represented by the red markers. The graph shows the deformed coordinates for a total of $N_{cells} = 32$ with a $\Delta_0 = \frac{1.5}{Re_\tau}$, where $Re_\tau = 271$. It is clearly seen that the domain is now deformed from having a unit length to now a length of $L_0 = 2$. The cell wall normal coordinates have been constructed such that the near-interface region now has the same slope as the near-wall region, confirming that these regions have the same deformations. This can also be confirmed from the slope of the deformation function which represents the cell stretch corresponding to the respective deformations in Fig. 5.4. Two different peaks are observed around -0.5 and 0.5 which confirm that the cell stretch around this region is high and correspond to two coarse regions. The other regions have small cell stretching which confirm that the these near-wall and the near-interface region have more fine cells than the coarse region. The constructed mesh is then better visualised in paraview which is seen from Fig.5.5

Since the higher meshes are quite hard to distinguishable between the coarse regions and the fine regions, paraview visualisation of the meshes are presented for a level 7 mesh, which has $N_x \times N_x \times N_z = (128 \times 128 \times 128)$ cells. 128 cells in the normal direction are clustered in the near-interface and the near-wall region. It is seen that the cells are refined less in the bulk region of each of the phase and and refined well near the interface and also near-walls to capture the boundary layers accurately.

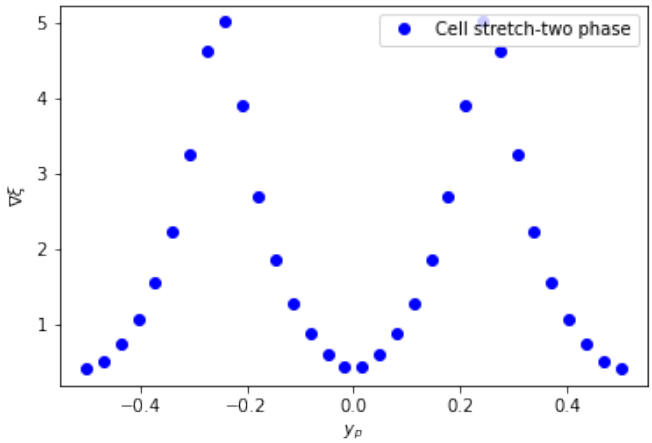

Figure 5.4: Cell stretch function for two-phase

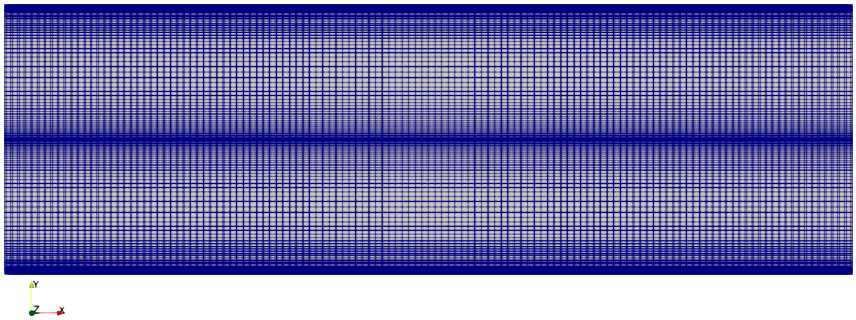

Figure 5.5: A visualisation of the clustered grid constructed for the two-phase problem

To capture these boundary layers to a good extent, it is equally important to choose a y^+ which falls under the viscous sub layer (as also discussed in the previous chapter) to depict the high sheared regions. Hence, the first cell should be stretched reasonably so that $y^+ < 5$. Initially a value of $\Delta y^+ = \frac{1.5}{Re_\tau^a}$ was tested. Although the motions in the air was resolved, this showed a large error in predicting the mean velocities in both the phases. Hence a better value of $\Delta y^+ = \frac{1.0}{Re_\tau^a}$ was used. By using this y^+ value, the cells are stretched even smaller in the near-interface and the wall region, making the resolution very fine compared to the when using the previous y^+. The change in y^+ value is accounted in such a way that the fine cells (typically near the interface) are made ever finer and the

coarse cells coarser (typically in the bulk of flow). Hence, this hinted us to move onto a better mesh, such as a M8 mesh, which typically has more cells distributed in the bulk flow. Mesh statistics for all of these values are tabulated in Table 5.2

Mesh	Shear Re	First cell width	Domain	Grid	Resolution		
M	Re_τ^a, Re_τ^w	y^+	$L_x \times Ł_y \times L_z$	$N_x \times N_y \times N_z$	Δx^+	Δy^+	Δz^+
M6	271,120	1.0	$2\pi \times 2 \times \pi$	$64 \times 64 \times 64$	12.3	1.07 - 28.76	6.18
M7	271,120	1.0	$2\pi \times 2 \times \pi$	$128 \times 128 \times 128$	6.18	1.02 - 11.16	3.09
M8	271,120	1.0	$2\pi \times 2 \times \pi$	$256 \times 256 \times 256$	3.09	1.00 - 3.86	1.54

Table 5.2: Mesh statistics

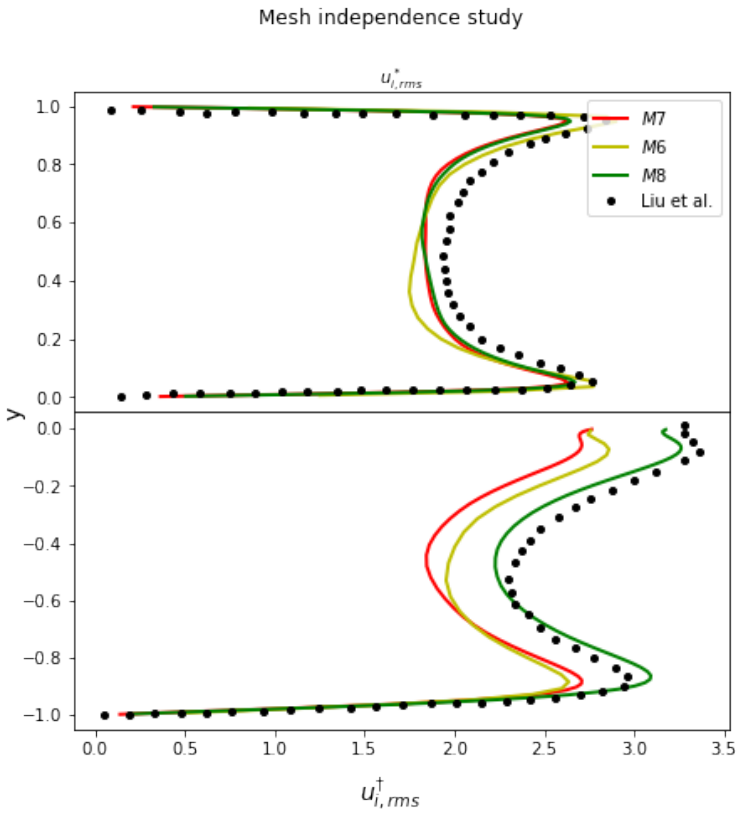

Figure 5.6: Statistics for 3 different meshes compared against [31]

Mesh statistics are presented for 3 different grids (M6, M7, M8) for the same resolution near boundaries. The coarsest cells in M6, M7 and M8 are have Δy^+ of 28.76, 11.16, 3.86 respectively. As a first observation we see that the first cell width Δy^+ scales with

the local Reynolds number Re_τ^a, the cell width of the coarse cells becomes high. Compared to Table 4.1, the coarse cells in the two-phase domain have high stretching. Hence given that, the cells in the bulk region are too coarse, there might be a possibility that the bulk flow would not be resolved accurately. This should be taken into account because, the unresolved bulk region might affect the interface and also the overall flow, leading to under prediction of the required data. Unlike single-phase flow which had close Δy^+ values for M8, we see that two-phase grids fail to have good resolutions overall even when moving to M8. This suggests that it is highly necessary to move onto to higher meshes such as M9 and M10 which would have 512 and 1024 cells clustered in the normal direction, to have a better accuracy. Unfortunately, considering the computational time and budgets, the simulation runs for these M9 and M10 meshes were not performed. A mesh independence study (Fig. 5.6) is performed to see the agreement between the grid presented in Table 5.2. The r.m.s fluctuations for these meshes are monitored. The statistics are compared against [31] who ran simulations for a clustered grid of $N_x \times N_y \times N_z = 128 \times 512 \times 256$ cells, who also report a huge under prediction when simulating on meshes with $N_y < 256$. M6 and M7 do not perform well as there is a huge error in predicting the fluctuations. This might be possibly due to the aforementioned fact that the insufficient resolution in the bulk region. But it is seen that, the M8 mesh performs comparable to a the grid presented in [31], which has a smaller Δy^+ value when compared the other two meshes. Hence, simulations and statistics are presented to the M8 grid from now since it has a comparable agreement with the chosen reference case.

5.4. RESULTS

This section will first start with the averaging procedures and then provide a qualitative description of some lower order and higher order statistics based on the described modelling in the previous section. Results are shown for a test case with corresponding to the M8 mesh and are compared against the simulations performed in [31] and turn out to be in a good agreement and hence the model being validated.

5.4.1. AVERAGING

Section 5.2 discussed the reasons why re-scaling of gradients across the boundaries were necessary. As computations proceed, we begin local averaging of instantaneous quantities to store in snapshots as discussed in section 4.3.1. Wall normal gradients are taken for computations of the budget terms. As we have two scales just across the interface, the gradients are scaled differently. Hence, we need some adjustments in the computations of gradients and second derivatives according to their respective scalings to estimate the budgets near the interface.

For the computations of gradients, the velocities from the cell centers are interpolated at the face. At the interface, without any scaling, the interpolated velocity would have units both air and water. For example, we would have,

$$\left\langle u_f(y)^{*,\dagger} \right\rangle = \frac{cm^+ \left\langle u^\dagger \right\rangle + cm^- \left\langle u^* \right\rangle}{cm^+ + cm^-}$$

where $\left\langle u_f(y)^{*,\dagger} \right\rangle$ represents the 'mixed' gradient. Using this gradient for the post-processing

gradients would lead to an incorrect computations in the budget terms. Hence, a new strategy for the computation in correct units is implemented which is discussed briefly.

Since we treat the problem as two single-phase domains, we disregard the idea of using velocities from the other phase for computing the interface gradient. We leverage the fact that we have already computed the interfacial velocity in two units, $u^*_{j,int}$ and $u^\dagger_{j,int}$ which could then be used to define gradients in their respective units. As a first step, scalar fields are created to store these interfacial velocities and they are averaged locally within a given time, t:

$$\left\langle u_{j,int}(x)^* \right\rangle = \frac{1}{\Delta t}\int_t^{t+\Delta t} u^*_{j,int}(t,\mathbf{x})\,dt \tag{5.21}$$

$$\left\langle u_{j,int}(x)^\dagger \right\rangle = \frac{1}{\Delta t}\int_t^{t+\Delta t} u^\dagger_{j,int}(t,\mathbf{x})\,dt \tag{5.22}$$

If we assume that the interface 'acts' like a boundary for the single-phase domains, we could compute gradients with $\left\langle u^*_{j,int} \right\rangle$ and $\left\langle u^\dagger_{j,int} \right\rangle$ like how any other gradient at a boundary would be computed. Additionally, we should be aware that now that the gradients are being approximated between a cell's face and it's cell center value. These interfacial gradients are:

$$\frac{d\left\langle u^*_{j,int} \right\rangle}{dy} \approx \frac{\left\langle u^*_j \right\rangle - \left\langle u^*_{j,int} \right\rangle}{cm \times \Delta/2} \tag{5.23}$$

in for the air side, and

$$\frac{d\left\langle u^\dagger_{j,int} \right\rangle}{dy} \approx \frac{\left\langle u^\dagger_{j,int} \right\rangle - \left\langle u^\dagger_j \right\rangle}{cm \times \Delta/2} \tag{5.24}$$

for the water side. Hence, without rescaling we can construct the interfacial gradients in its respective units by just averaging the interfacial velocity fields. The second derivatives are constructed in the same way, involving the interfacial gradient. Using the averaged interfacial velocity, the gradient is calculated (equations 5.23, 5.24). Now that these gradients have their respective units, the second derivatives are approximated without any rescaling in the same way as explained in section 4.3.1 :

$$\frac{d^2\left\langle u^\dagger_{j,int} \right\rangle}{dy^2} \approx \frac{\frac{d\left\langle u^\dagger_{j,int} \right\rangle}{dy} - \frac{d\left\langle u^\dagger_j \right\rangle}{dy} > \Big|_{-1}}{cm \times \Delta} \tag{5.25}$$

for the water side, and

$$\frac{d^2\left\langle u^*_{j,int} \right\rangle}{dy^2} \approx \frac{\frac{d\left\langle u^*_{j,int} \right\rangle}{dy} - \frac{d\left\langle u^*_j \right\rangle}{dy} > \Big|_{-1}}{cm \times \Delta} \tag{5.26}$$

The other procedures of locally averaging fields and ensemble averaging in space and time over N snapshots remain similar to what is explained in section 4.3.1.

5.4.2. MEAN VELOCITIES AND R.M.S FLUCTUATIONS

Firstly, the dimensional velocity profiles are shown in Fig. 5.7. The raw output produced by Basilisk is non-dimensionalised since we solve the non-dimensional equations of momentum. Table 5.1 is used to calculate the respective shear velocities of air and water phase and the velocities represented are rescaled up to the physical units. From the figure, it is seen that when the velocities are plotted on the same scale the water side velocities are much smaller in magnitude when compared to the air-side. This is because of the large difference in the dynamic viscosities in both the phases ($\mu_a \ll \mu_w$). Visualisations of the instantaneous dimensional velocity from post processing are also shown in Figure 5.8. It is observed that the air side velocities are much higher when compared to the water side. The small bulk Re and high dynamic visocities pose a high inertia on the water side, causing it to have much smaller motions when compared to the low viscous fluid above it.

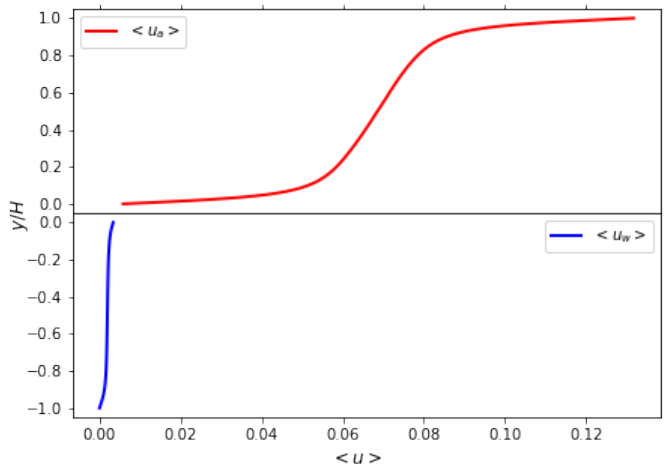

Figure 5.7: The mean dimensional velocity profiles of air phase, in red and water phase, in blue

The interface velocity is not shown in Figure 5.7 since the velocities being a cell centered term, are averaged at the cell centers (and also for the other results in this thesis). But in principle, the velocities do not show any jumps, and are continuous at the interface, thereby also satisfying the interfacial condition 5.2. Due to the difference in the magnitude, it is almost apparent that the velocity has a linear profile. Hence, it becomes very hard to understand the turbulent nature in the water phase, unless rescaled. This, leads us to the conclusion that one needs to study the statistics in its respective scales to infer more qualitative results.

It makes sense physically, to examine the statistics after normalisation in wall units/shear scales. From the continuity relations, a scaling factor $\mathscr{S}$, by which the shear scales are

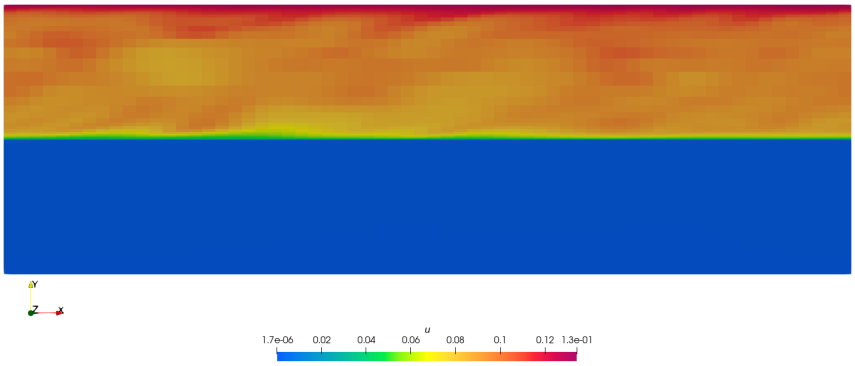

Figure 5.8: Snapshot of instantaneous dimensional velocity taken at $t^+ = 60$ for a grid with $N_x \times N_y \times N_z = 64 \times 64 \times 64$ cells.

related was shown. It was seen that, $u_\tau^a = \mathscr{S} u_\tau^w$. After normalisation, as a result, we see that the air side motions are scaled down and the water side motions are scaled up, bringing them up to a closely comparable scale. Hence, to understand the respective turbulent behaviour in each of the phase, the non-dimensionalised statistics are presented henceforth (which is already what comes out as the raw data from RK-Basilisk simulations, since the basis of these simulations already involve different scalings).

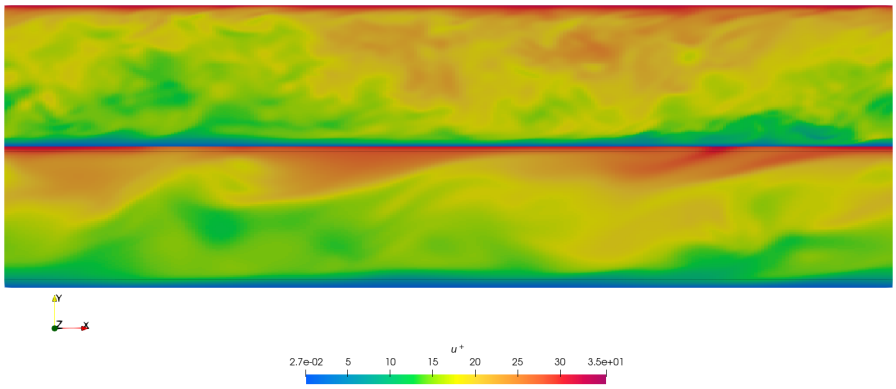

Figure 5.9: Snapshot of instantaneous velocity at $t^+ = 60$

Figure 5.9 shows a snapshot of the instantaneous velocity at $t^+ = 60$ on a M8 mesh.

The flow direction is from left to right along the periodic boundaries. As a first observation it is seen that due to a high Re_τ^a, the air side motions are more incoherent and constitutes more turbulent behaviour than the water side motions. Since we force the normal fluxes at the interface to be zero at all instances, the interface remains flat. Unlike the dimensional scale as seen in Figure 5.8, the water side interfacial velocities are in comparable scales of top wall velocity in the air phase, and consequently air side velocities near the interface and comparable to the velocities near the bottom wall in water phase. This is of course due to the fact that the velocities are scaled up and scaled down because of the scaling factor $\mathscr{S}$. From visualisations, it can be said that the constructed M8 mesh has performed well in capturing the interface velocities well since the boundary layers look captured well enough. This is qualitatively examined in the upcoming discussions.

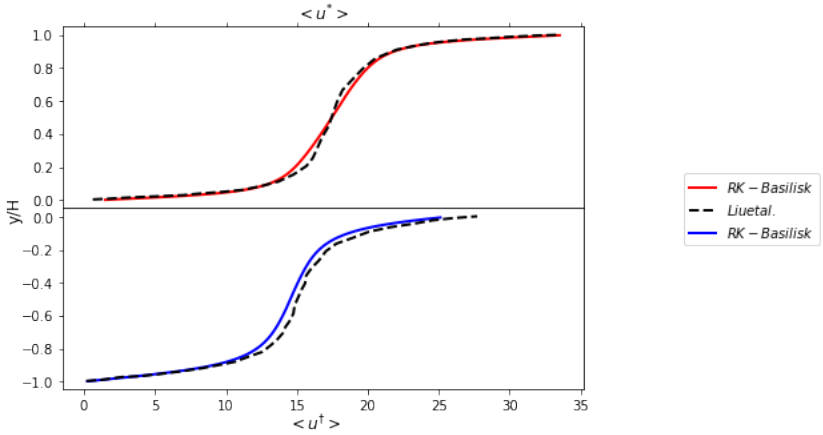

Figure 5.10: Mean velocities of both air and water phase in non-dimensionalised units of air and water.

Figure 5.10 shows the mean velocities of air ($\langle u^* \rangle$) and water ($\langle u^\dagger \rangle$) phase each of them non-dimensionalised in their respective shear units. Unlike in Figure 5.7, due to the difference in scales, both the phases show the characteristic 'S-shaped' profile as seen in turbulent Couette flows. The data is compared against the mean velocities shown in [31] and seem to have a good agreement. Although, there is a very small under prediction. This might be due to the fact that we need a much better resolution to capture the bulk flow. Around $0.3 < y/H < 0.7$, there is a minimal under prediction and this being in the bulk region of the flow, suggests that a better resolution is needed to resolve the flow in these regions, as also discussed in the previous section. Another reason might be the inaccurate imposition of the wall shear stress. If the imposed wall velocity, U_w is lesser than what is supposed to be imposed, it might lead to the flow being less sheared. This consequently reduces the interface velocity, u_i and might lead to the water being less sheared since we know that the flow in the water phase is completely driven by the flow in air. Apart from these observations, in the bulk flow, $-0.7 < y/H < -0.3$ and $0.3 < y/H < 0.7$ the flow is subjected to small change in velocities. And at the center line of the channel, the flow does not have a zero gradient, indicating that there are

simply non-zero shear stresses too. And in regions $-1.0 < y/H < 0.8$, $-0.2 < y/H < 0.2$, $0.8 < y/H < 1.0$ we see that the velocity in the respective phases show high slopes. These near-wall gradients are hence subjected to high gradients. These facts can also be confirmed by examining the Figure 5.11. As mentioned in the averaging section, wall nor-

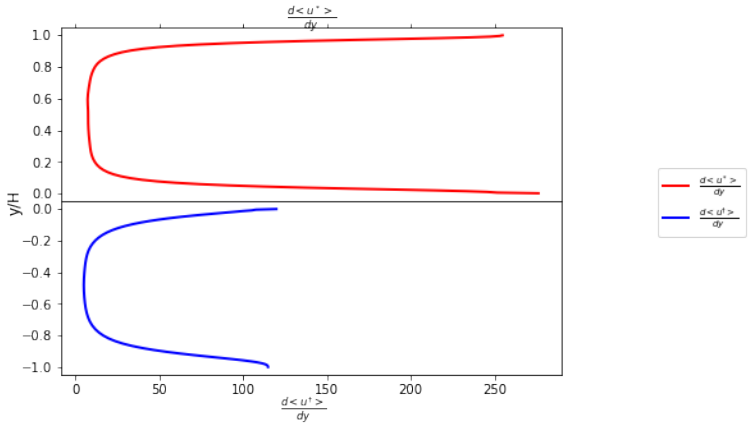

Figure 5.11: Mean streamwise velocity gradient taken over the channel height. The quantities are non-dimensionalised in their respective shear units

mal gradients require a rescaling at the interface because since the FDM operator used to construct the interface gradients would have two different velocity scales. Hence, the re-scaled gradients are presented here. The near-interface and the near-wall region have high gradients whereas the bulk region is as apparent as to having a zero gradient. Knowing that the velocity in the bulk is not constant, it is safe to assume that, these gradients still have a finite value and does not necessarily have a zero gradient in the bulk. There are certainly a few theoretical and experimental studies ([35] [3] [20]) which confirm that the center line gradient approaches a value of 0.2 (in non-dimensional units) as $Re_\tau \to \infty$. A clear inference from this is that, there is certainly a non-zero shear stress and thus turbulent production in these center lines [56] [31]. Another inference from these plots is the ratio of these gradients. We know from the continuity of shear (shown for mean velocities) that:

$$\mu_a \frac{d\left\langle u_j^a \right\rangle}{dy} = \mu_w \frac{d\left\langle u_j^w \right\rangle}{dy} \tag{5.27}$$

The non-dimensional shear stress is continuous by

$$\mu_a u_\tau^a \frac{d\left\langle u_j^* \right\rangle}{dy} = \mu_w u_\tau^w \frac{d\left\langle u_j^\dagger \right\rangle}{dy} \tag{5.28}$$

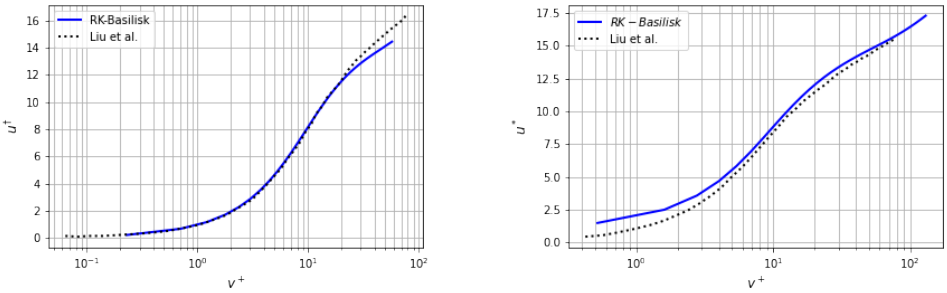

Figure 5.12: Mean velocities in the logarithmic scales for (a) near-wall and (b) near-interface in the air side

Plugging the respective dynamic viscosities and the scaling factor for the shear velocities, we see :

$$\frac{d < u^* >}{dy} \approx 2.26 \frac{d < u^\dagger >}{dy} \tag{5.29}$$

This ratio is also what is seen from the plot, where the non dimensional gradient of air phase is around 2.26 higher than the non dimensional gradient of the water phase thereby also indicating the correctness of the physical model implemented with appropriate scalings.

The mean velocities in the classical logarithmic scale is showed in Figure 5.12. Figure 5.12(a) shows the mean velocities near the bottom wall in the air side. As seen in classical wall bounded turbulent flows, a viscous sub layer is observed in $y^+ < 5$ followed by the thin buffer layer. Beyond $y^+ \approx 30$, the log-law layer followed by the outer layer appears. Similarly comparisons are made for the near-interface region in the air side (seen in Figure 5.12(b)). We see that the velocity does not necessarily start at zero, suggesting that there is a small interface velocity in the air side. But it is readily noted that, the air side does have the logarithmic behaviour as a wall bounded flow would. Hence, a main inference would be that the side feels the interface as a flexible non-deforming wall.

Next, the turbulence intensity $u'_{i,rms} = \sqrt{\langle u'_i u'_i \rangle}$ is plotted Figure 5.13. The averaged fluctuations are normalised by u_τ^2 in their shear units. The values are compared against the reference data sets of [31]. For the mesh chosen for the test case, there is a fairly good agreement. The streamwise fluctuations in the flow seem to be stronger when compared to the other two directions, followed by the spanwise fluctuations having a higher magnitude than the normal fluctuations. Comparing the streamwise fluctuations, the maxima is obtained around $y/H \approx 0.1$ and $y/H \approx 0.9$ in the air side. The intensity of turbulence seem to be the strongest in these near-wall and near-interface regions. Whereas, the water side fluctuations are very distinctive. In the near-interface region of water side, the fluctuations do no die out as we see in the air side. But a similarity is seen in the bot-

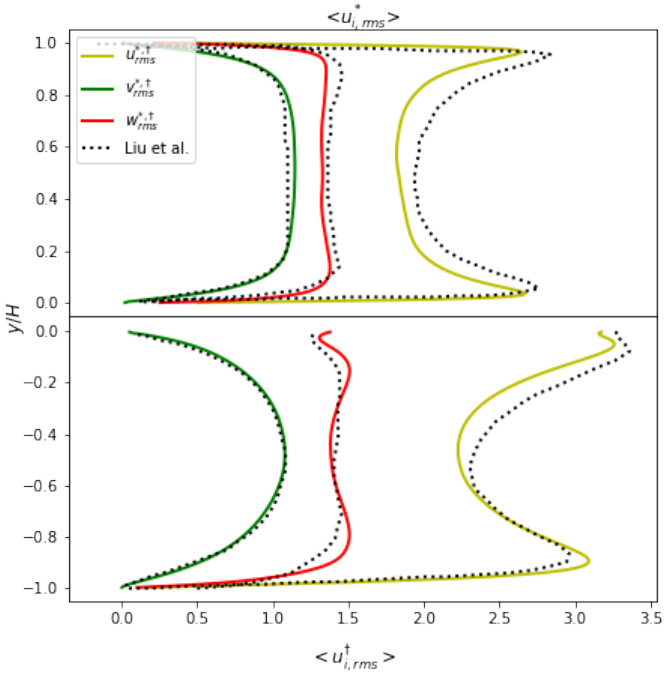

Figure 5.13: The fluctuating velocity components

tom wall. This means that, for the water phase, the interface is less constrained when compared to the bottom wall and has comparatively a less shear. The intensities are also comparable to what is seen in a turbulent open channel flow [51]. The spanwise fluctuations seem to have a similar behaviour as the streamwise fluctuations. Although, there are a few differences. The highest fluctuations are peaked around $w_{rms} \approx 1.5$ for both the phases and does remain constant throughout the domain in the normal direction. In the air side, at the top wall, the fluctuations die out due to the presence of a wall. With the fluctuations going almost to zero at the interface, establishes the fact that the interface is seen as wall by the gas phase. Water side spanwise fluctuations near the interface also have a non-zero value indicating a constraint free surface. Similarities between the normal fluctuations and the streamwise fluctuations are observed. Interestingly, the normal fluctuations at the interface for the water side die out. This is only because we enforce the normal fluxes at the interface to be zero.

In overall, the air side turbulence fluctuations have the behaviour of single-phase wall bounded flows. As an obvious partial fact, this is because of the presence of a wall at the top side. But the near the interface, after presenting the statistics in it's respective scales, the fluctuations go almost to zero. This shows that certainly a high inertia is

felt due to the high shear imposed by water on air, hence the interface behaving like a wall for the air side. Generally in pressure driven channels, a local minima is observed in the center line of the channel. But this is not observed in Couette flows due to a non-zero shear at the interface [20]. This also helps in supporting an already drawn inference there exists non zero production and dissipation at the center line of the channel, since the balance of the TKE is constituted by the normal stresses $\langle u'u' \rangle, \langle v'v' \rangle, \langle w'w' \rangle$ in the Reynolds stress tensor.

5.4.3. REYNOLDS STRESSES

The components along the diagonals of the Reynolds stress tensor are the normal stresses and the off-diagonal components are the turbulent shear stresses. In particular the most interesting component is $R_{xy} = -\left\langle u'_x u'_y \right\rangle = -\langle u'v' \rangle$. Figure 5.14 shows the distribution of this particular component across the channel height. We see that the stress has a peak value of 0.8 (in non-dimensional units) in the bulk of the channel and stays constant throughout the bulk. Upon integrating the mean streamwise momentum equations with

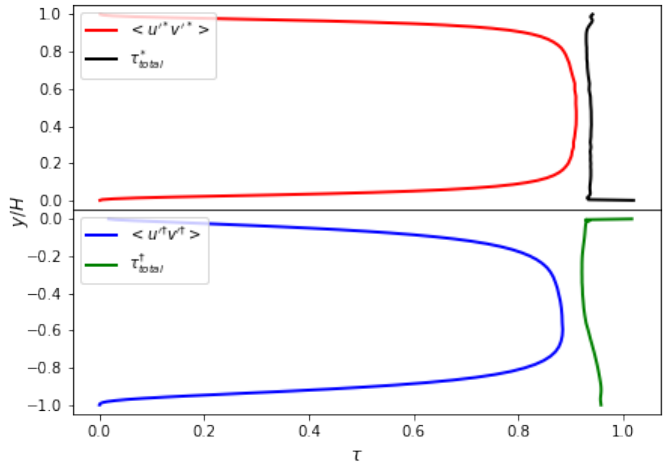

Figure 5.14: Reynolds shear stress R_{xy} and the total shear stress in the channel τ

the conditions for a Couette flow, we see that (also shown in the previous chapter)

$$\mu \frac{d\langle u' \rangle^+}{dy^+} - \frac{\langle u'v' \rangle}{u_\tau^2} = 1 \tag{5.30}$$

$$= \tau_{total} \tag{5.31}$$

is the total shear stress across the channel in the normal direction [20]. The above relation is generalised in non-dimensional units. The total shear stress is plotted along with

the shear stresses in Figure 5.14. The total (planar) shear stress, τ_{total} arises from contributions of shear from viscous stresses and turbulent (Reynolds) stresses and both of the stresses seem to be dominating near the wall, but only one of them is stronger in the bulk. As discussed the viscous shear stress dominates in the near-wall and near-interface region, whereas the turbulent shear stresses dominate near boundaries, near-interface, and also in bulk (ref Figure 5.11 and Figure 5.14). In theory, the deviation of the viscous shear stress $\mu^+ \frac{d\langle u^+ \rangle}{dy^+}$ from the total shear stress τ is balanced by the contributions of the turbulent shear stress $\langle u'v' \rangle / u_\tau^2$. But in this test case simulated, we see that the shear stress τ is not exactly unity and has a small under-prediction. But exactly at the interface, the stress equals unity for both the air and water phase. As discussed earlier, an imposed wall shear stress drives the flow in air, which in turn drives the flow in water. An incorrect imposition might lead to an under prediction or an over prediction of the shear stress and looking at the plot, there might have been a possibility that the shear stress imposed was little under than what was required. Another theory is that a loss in overall momentum in the channel. Due to a "shear-free-like" surface for water at the interface, there might be excess dissipation than what is produced, which in turn affects in the momentum in the water-phase. This leads to the entire air-water domain having a small loss in momentum. To rectify this, the boundary conditions were corrected to impose more shear throughout the channel. But the deviations in the τ was still observed and thus stands as a problem not solved, creating room for improvement.

5.4.4. TURBULENCE KINETIC ENERGY BUDGET

In this section, the behaviour of TKE and it's budgets comprising of various mechanisms are discussed. Firstly, the individual terms of these budgets are explained with the context of two-phase flow. Then the budgets are shown altogether in a single scale to elaborate on the overall picture, redistribution mechanisms etc. Finally, the error in computing these budget terms is shown and the possible reasons are briefly discussed.

Turbulence kinetic energy,

$$k_a = \frac{1}{2}(\langle u'^* u'^* \rangle + \langle v'^* v'^* \rangle + \langle w'^* w'^* \rangle) \tag{5.32}$$

and

$$k_w = \frac{1}{2}(\langle u'^\dagger u'^\dagger \rangle + \langle v'^\dagger v'^\dagger \rangle + \langle w'^\dagger w'^\dagger \rangle) \tag{5.33}$$

is the kinetic energy associated in the turbulent flow characterized by the velocity fluctuations in each of the phase. Figure 5.15 shows the kinetic energy k_a and k_w in air and water phase respectively. Kinetic energy in the air side peaks near-wall and near-interface and thus looks to be symmetric. Whereas, this symmetricity is not observed in k_w. k_w has a peak at the bottom wall and has the same magnitude as the peaks observed in air-side. But just at the interface, the kinetic energy attains a maximum considering the overall flow. There is a non-zero kinetic energy associated with the "shear-free-like" surface. Hence, it is seen that the kinetic energy from the mean flow is re-distributed

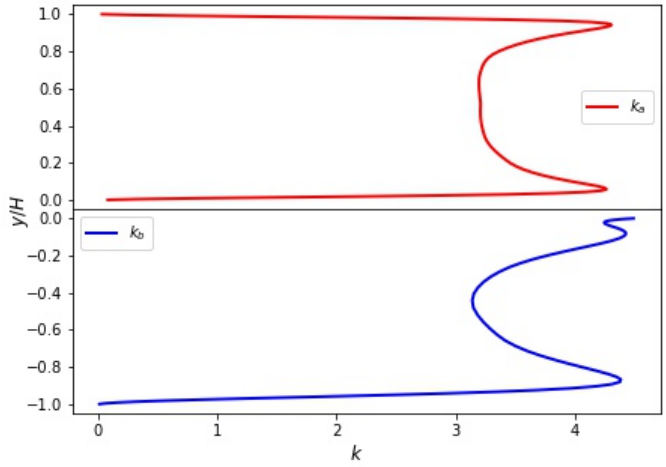

Figure 5.15: Turbulent kinetic energy in both the phases

more towards the interface in the fluid having the lighter density.

The turbulent kinetic energy (TKE) budget identifies the contributions of physical mechanisms that influence turbulent flow characterized by velocity fluctuations. The TKE budget is linked to the physical systems that create, transport, and decay turbulence by nature. Each term's weight indicates flow's potential to decay or cause turbulence. These physical mechanisms that change the rate of the kinetic energy are turbulence production, turbulent diffusion and dissipation. The diffusion can still be decomposed as 3 other physical mechanisms : diffusion due to pressure, diffusion due to molecular forces and finally the turbulent transport. On the whole they can be represented by the following equation shown separately in units of water (†) and in units of air (∗).

$$\frac{Dk_a}{Dt} = \underbrace{-\left\langle u_i^{*\prime} u_j^{*\prime} \right\rangle \frac{\partial \left\langle u_i^* \right\rangle}{\partial x_j}}_{\text{Production}} \underbrace{-\frac{1}{\rho}\frac{\partial}{\partial x_i}\left\langle p^* u_i^{*\prime} \right\rangle}_{\text{Press. Diffusion}} \underbrace{-\frac{1}{2}\frac{\partial}{\partial x_j}\left\langle u_i^{*\prime} u_i^{*\prime} u_j^{*\prime} \right\rangle}_{\text{Turb. Transport}} + \underbrace{\frac{1}{2}\nu\frac{\partial^2}{\partial x_j^2}\left\langle u_i^{*\prime} u_i^{*\prime} \right\rangle}_{\text{Viscous Diffusion}} \underbrace{-\nu\left\langle \frac{\partial u_i^{*\prime}}{\partial x_j}\frac{\partial u_i^{*\prime}}{\partial x_j} \right\rangle}_{\text{Dissipation}} \tag{5.34}$$

and

$$\frac{Dk_w}{Dt} = \underbrace{-\left\langle u_i^{\dagger\prime} u_j^{\dagger\prime} \right\rangle \frac{\partial \left\langle u_i^\dagger \right\rangle}{\partial x_j}}_{\text{Production}} \underbrace{-\frac{1}{\rho}\frac{\partial}{\partial x_i}\left\langle p^\dagger u_i^{\dagger\prime} \right\rangle}_{\text{Press. Diffusion}} \underbrace{-\frac{1}{2}\frac{\partial}{\partial x_j}\left\langle u_i^{\dagger\prime} u_i^{\dagger\prime} u_j^{\dagger\prime} \right\rangle}_{\text{Turb. Transport}} + \underbrace{\frac{1}{2}\nu\frac{\partial^2}{\partial x_j^2}\left\langle u_i^{\dagger\prime} u_i^{\dagger\prime} \right\rangle}_{\text{Viscous Diffusion}} \underbrace{-\nu\left\langle \frac{\partial u_i^{\dagger\prime}}{\partial x_j}\frac{\partial u_i^{\dagger\prime}}{\partial x_j} \right\rangle}_{\text{Dissipation}} \tag{5.35}$$

The left hand side of both the equations are typically zero due to the fact that we average when the flow is statistically steady (verified with constant planar shear stress).

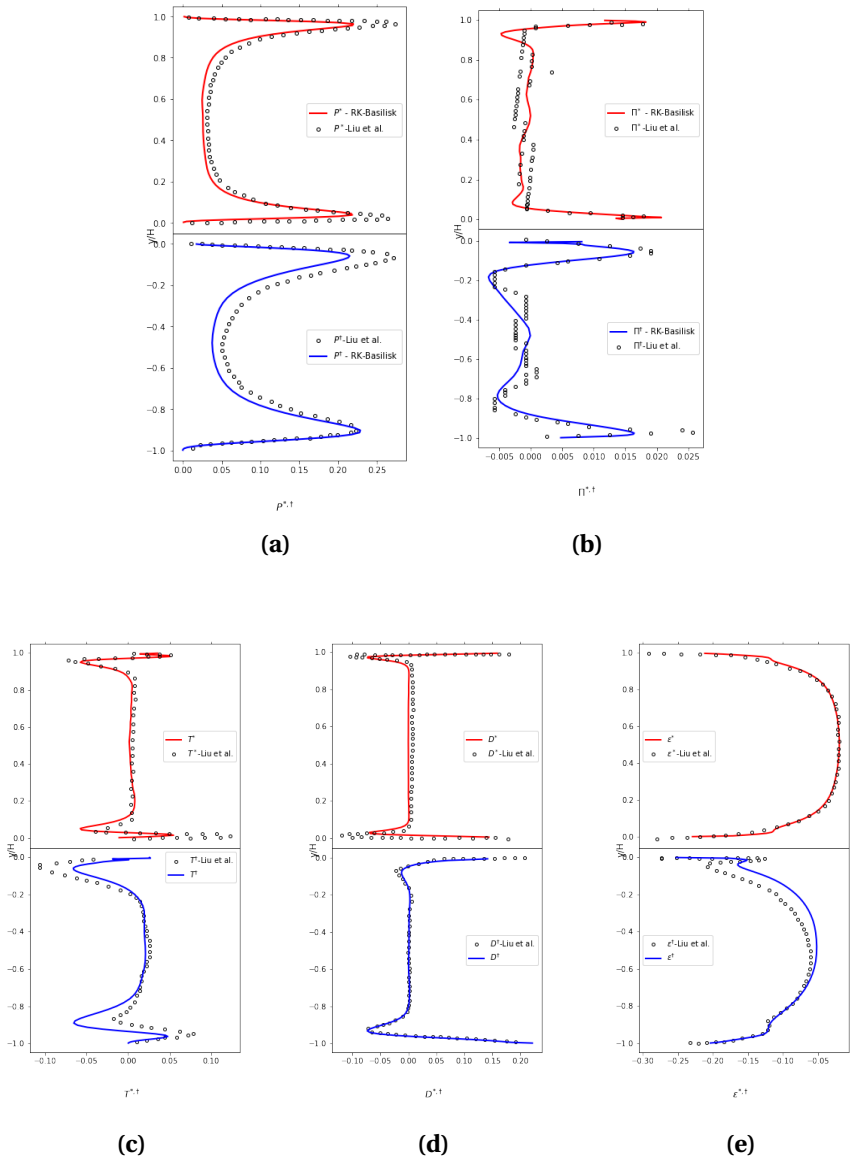

Figure 5.16: Individual terms in the budget equation 4.20 for both the phases of **(a)** Production **(b)** Pressure diffusion **(c)** Turbulent transport **(d)** Viscous diffusion **(e)** Dissipation. Solid blue lines represent the water phase, compared against [21] and red lines represent the air phase compared against [1] .

Figure 5.16 shows the individual terms of the budgets. The production in the channel is characterized by interaction of the turbulent stresses and the mean gradient. Looking

near the interface (see Figure 5.16(a)), the production is similar to the top wall (where it is localised in $y^+ < 19.5$), indicating that the interface for the air side is 'wall-like'. The water side production also has similarity when it comes the the profile being symmetric (near-wall and near-interface). But what is more appealing is that the spatial extent of production in the water-phase is more when compared to the air-phase, typically until $y^+ < 37.3$. This might be because of the the difference in thickness of boundary layers between the air and water phases near the interface.

The smallest contributions to the transport is due to pressure (see Figure 5.16(b)). Although hardly noticed due to small magnitudes, a good agreement for the pressure diffusion was obtained. The reference data for the pressure diffusion is sampled irregularly since it was very intricate to collect data based on very small magnitudes. A sharp increase in the pressure diffusion is observed in the logarithmic regions.

A slightly higher order statistic in TKE budget is the transport due to the triple product in velocity fluctuations (see Figure 5.16(c)). Thus, noticeable local increase in the magnitude of fluctuations directly affect the transport terms too. As far as the agreement is concerned, the test case is able to reproduce the transport terms decently. It shows the typical trend and matches well for the air side, but in the water phase, there is a noticeable under prediction. The general behaviour of the transport term is that it has two peaks (one positive and one negative). The negative peak means that the energy transported into the area while a positive peak means that the energy is taken away from that area [31]. Since air drives the flow in water, as a general notion we can say that the kinetic energy from the bulk flow in air side is transported 'into' near-interface region of the water side, and further from the near-interface region into the bulk of water, as also seen in the reference case [31].

Viscous diffusion is more localised near-walls and near-interfaces (see Figure 5.16(d)). This is very well noticed in the air phase both near-wall and near-interface, due to the obvious reason of behaviour being similar to the single-phase flow. But the diffusion is significantly different in the water-phase. In particular the diffusion seems to be higher near the interface as also seen in open channel flows simulations of [21].

Looking at the dissipation in the air side, it decreases in the bulk region, and has a sharp increase towards the interface, balancing different budget terms in different regions (discussed in the upcoming paragraphs) (see Figure 5.16(e)). The dissipation in the water side is more interesting because of the asymmetries between the interface and the bottom wall. The kinks in both these regions are different and the dissipation near the interface is more significant. The dissipation has a weak agreement with the reference case here, but does reproduce the 'dip' indicating the presence of more dissipation of turbulence at the interface.

The trends of these budgets altogether is presented in Figure 5.17 and are compared against the data from [31]. We see that there is fairly good agreement with the most budgets presented by the group. Looking at the overall picture, we see that these budgets

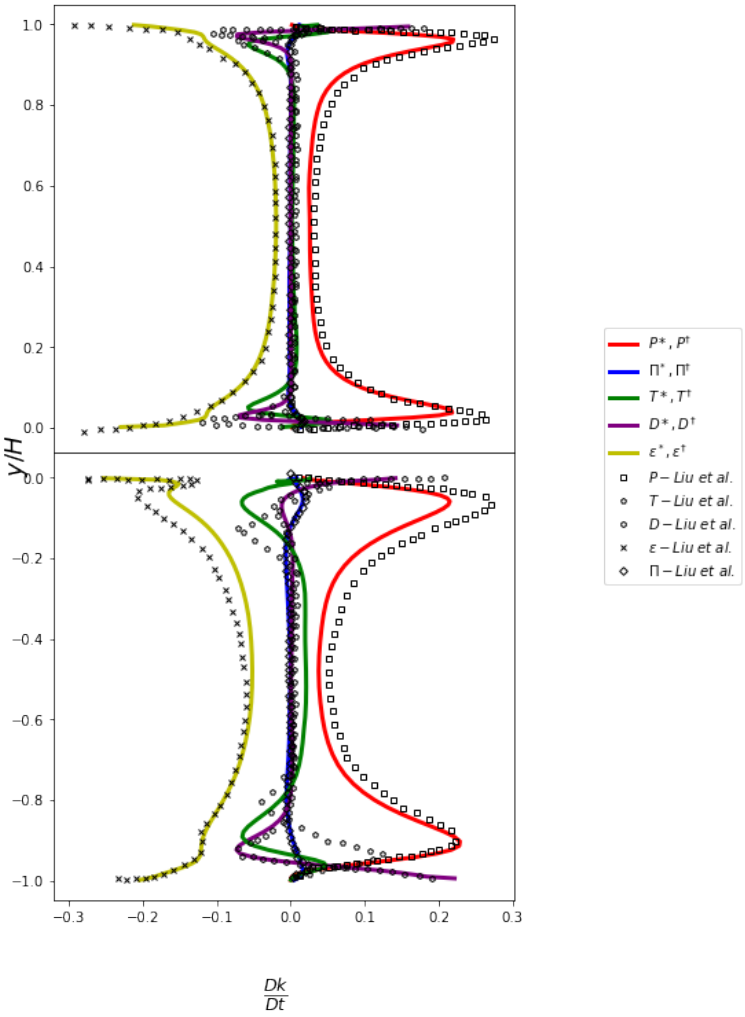

Figure 5.17: Turbulence kinetic energy budget in air-phase (top) and water-phase (bottom).

become more important near the walls and near-interface of these individual channels. Due to a non-zero shear stress throughout, there is turbulence generation at the center line in both of the channels. We mainly notice that the budgets in the air side resemble the budgets in a wall bounded turbulent flow, whereas in the near-interface region of water phase, the budgets show similarity to an open channel flow. Although there is a high shear stress 'at' the interface, the water phase perceives the air-phase as a open surface which is sheared notably lesser. As a result, the air-phase perceives water to be a wall whereas water perceives air like a free surface. From the transport and viscous diffusion, we see that the kinetic energy which is produced in the bulk (also top wall) is transported near the interface and then further from the interface into the near-interface

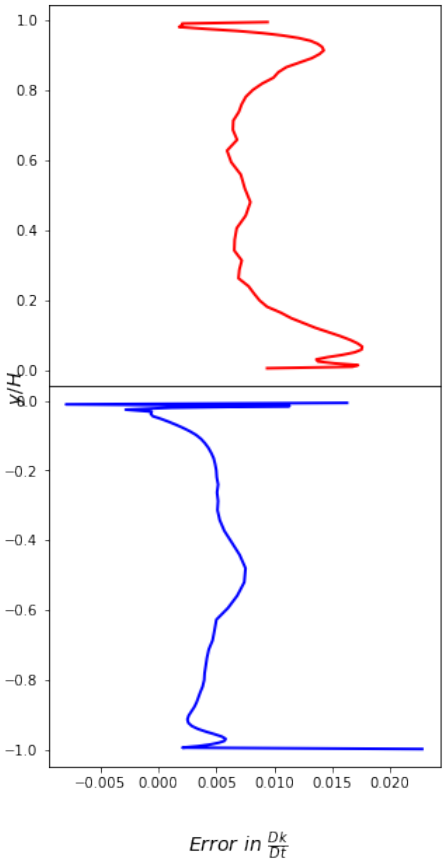

Figure 5.18: Error in the prediction of the budgets in TKE

region of water. This makes sense because of the primary fact that motions of water is purely driven by the shear of air. The most distinguishing budget term is the dissipation near the interface in water. Due to the "shear-free-like" surface, the lighter phase experiences high dissipation rates. Moreover, dissipation is seemed to be balanced by different terms in different parts of the flow in the water phase. At the interface, the dissipation is almost balanced by viscous diffusion. Just away from the interface, in the viscous sub-layer, dissipation is balanced by production. But as we move away from these regions and towards the bulk, we see that interestingly, dissipation is balanced by production and a small positive value of turbulent transport. In a nutshell, we see that the kinetic energy in the water side is affected due the kinetic energy in the air side. Thus, the air-water interactions, say in a more coarse models such as RANS and LES should be modelled more carefully.

Finally, we talk about the error in predicting the budget terms. As mentioned earlier,

as we average through a statistically steady state, the LHS of the TKE budget equations 5.35 and 5.34 should be zero. But upon trying to study the balance, in Figure 5.18, we see there is a small error in the order of magnitude in $1e-3$. While this could be mostly due to the approximation errors and and inadequate grids (up to Taylor micro-scales) as discussed in the previous chapter, it could also be due to the fact that, we need more higher order methods such as spectral methods to solve such two-phase problems. Another possibility is that with the general behaviour of the air-water stratified case, there might be a small imbalance in the TKE budgets due to the diffusion and dissipation mechanisms, as we also see that the kinetic energy at the interface is not only non-zero, but attains a maximum value compared to the other parts of the flow (see Figure 5.15).

5.4.5. STRUCTURES IN AIR-WATER COUPLING

The coupling of air and water is explained with vortical structures which identified from post processing the simulations in paraview, which also have the potential to support the inferences of TKE budgets [31]. Coherent structures are vortices correlated over a spatial extent [16]. By studying the coherent structures, we can except to get a qualitative understanding of vortices and thus the vortical structures. The vortical structures in Figure 5.19 are visualised by the Q-criterion. 'Q' here is:

$$Q = -\frac{1}{2} tr(\mathbf{S}^2 + \Omega^2) \tag{5.36}$$

where $\mathbf{S}$ and Ω are the strain rate and the vorticity tensors and represents the average balance between the unsteady straining and rotation [16]. Looking at Figure 5.19, an immediate observation is the difference in the cohesion of both the phases. We see that the structures in the air phase is more incoherent than the structures in water. This is because the air side has a high Re and high speed motions and lower inertia, contrasting to the water phase. The water side motions are more coherent, elongated a more persistent in space. The structures just above the interface in the air side seem to have a bigger spatial extent when compared to the structures in the mean flow. Thus, a high shear stress exists near the interface in the water-side. Since the stresses are continuous at the interface, the same high shear stress is also 'felt' in the near-interface region of air side, causing it to have similar structures (spatially extended more than the structures in the bulk flow of air) as the water side confirming that there is a 'coupling' existing between air and the water side. Another interesting observation is that, the vortices in the water side have an apparent upward motion, i.e, towards the interface. Although not shown here, these vortices tend to 'dissipate' at the interface comparable to the vortices at the free surface [31]. This is in accordance with the high dissipation rate also seen at the interface.

The presence of these vortical structures can also be confirmed by qualitatively examining the streamwise fluctuations.

Figures 5.20, 5.21,5.22 and 5.23 show the fluctuating component of the of the streamwise velocities. These components form low and high speed regions called the *streaks*. As these streaks can lead to creating vorticity in the flow, a good indication of the presence of vortical structures can be studied by examining the streaks [4]. The streaks in

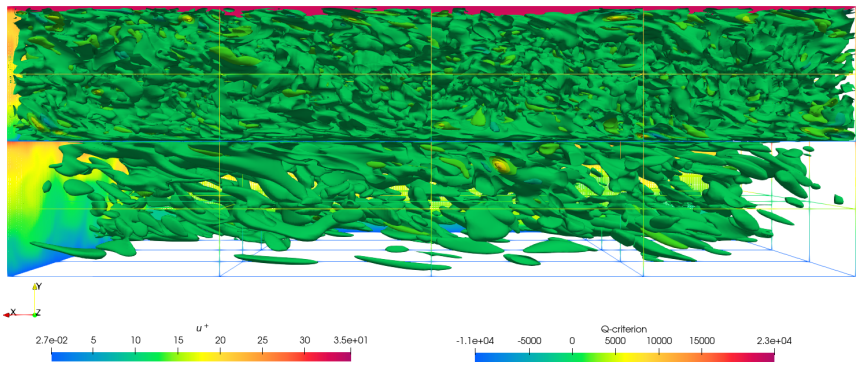

Figure 5.19: Iso-contours of vortices visualised by the Q-criterion. Direction of the flow is from right to left.

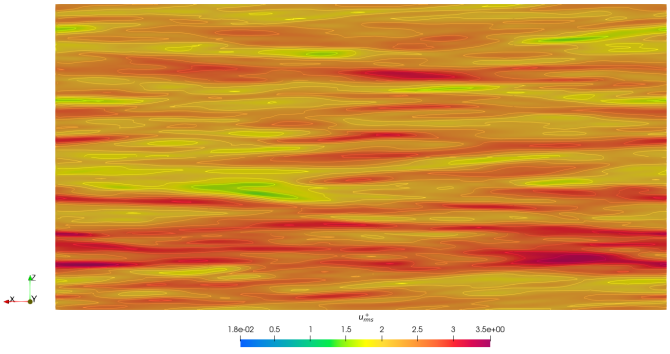

Figure 5.20: Streamwise fluctuations represented in a plane at $y^+ = 6.96$

the air side seem to be predominantly of high speed regions (see Figure 5.20), whereas the streaks in the water side seem to be of low speed (see Figure 5.23). Especially in the air-phase, streaks are shown for two different locations, close to the interface. Figure 5.21 shows the air side streaks closest to the interface. It seen that there are equally low speed regions with the extent of these streaks being more than what is seen in Figure 5.20. These two visualisations are located inside and just outside the viscous sub-layer. Within the viscous sub layer, the streaks show similarity to the streaks observed in the water side (see Figure 5.23). The water side also has low speed regions with the extent of cover of these vortices being high. This confirms the presence of similar vortical structures in the water-side and just above the interface in air-side. But as we move outside the viscous sub-layer, the vortices seem to have more high speed regions (see Figure 5.20) with the structures being small as what is also seen in wall boundary layers. Looking at the interface (see Figure 5.22), the streaks present closely resemble the water-side. The

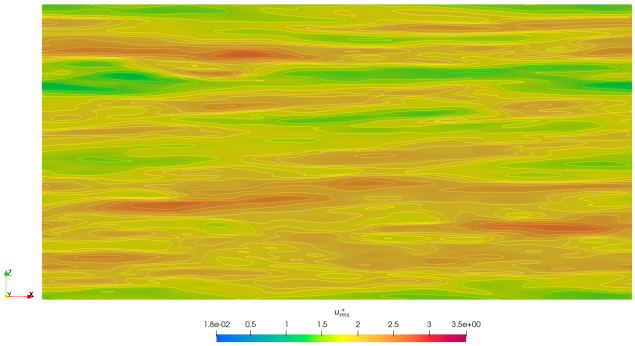

Figure 5.21: Streamwise fluctuations represented in a plane at $y^+ = 1.52$

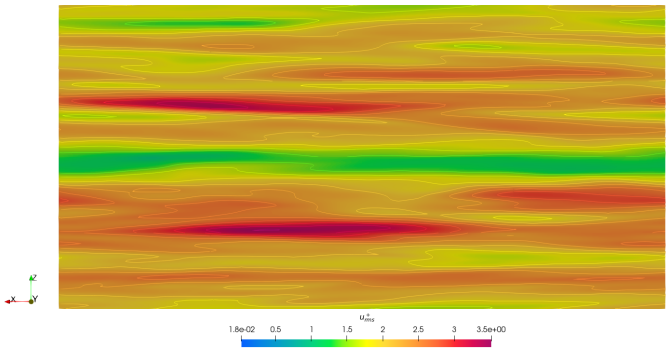

Figure 5.22: Streamwise fluctuations at the interface

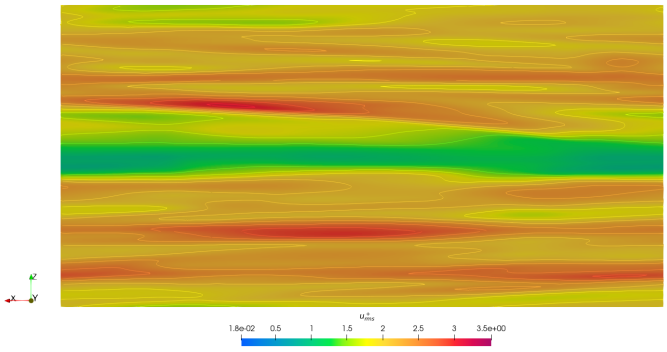

Figure 5.23: Streamwise fluctuations represented in a plane at $y^+ = -1.52$

streaks are of low speeds and cover more extent. This means that the interface motions are controlled by the water-phase [31]. With this study it could be confirmed that due to the air-water coupling, the low speed streaks cause the vortices to behave as if it were near a free surface, causing high dissipation at the interface which is also seen in the budgets of turbulent kinetic energy.

6

COUNTER CURRENT FLOW

Another interesting configuration of stratified flows is where both the flows move in an opposite direction, termed as counter-current flows. We intend to test the implemented model for a counter current situation and infer a few contrasting results (if any). This chapter starts out with some initial literature survey of single phase and open channel turbulent flows. Briefly the numerical scheme is discussed. Then a few interesting results are showed.

We are primarily interested to perform DNS for a two phase pressure driven counter-current stratified flow with a flat interface. Upon performing an extensive literature research, no DNS reference cases for aforementioned test case were found. Hence, a brief survey of single phase channel flow is given since the close resemblance of the air-phase to wall bounded pressure driven channels, hoping to gain some insights about turbulent channel flow simulations. Traditionally, DNS performed to study internal turbulent flows were on pipes and channels. Few of the recognised works in these topics are from [1][17][36]. [1] performed a DNS for a range of frictional Reynolds number to study their dependence on the overall turbulent behaviour. The numerical scheme adopted was a higher order finite differences for spatial discretization and time advancement was done using Crank-Nicholson and Adam-Bashforth on a fractional iteration scheme. Since the choice of the domain plays an important role in determining Large Scale Structures (LSS), two-point correlations were studied to choose adequate domain dimensions. The Turbulent Kinetic Energy (TKE) equation was solved and the Reynolds stresses were studied and the difference in the isotropic nature of turbulence in different parts of the domain was highlighted. Moreover, it was concluded that as Re_τ is increased, the RMS fluctuations of the streamwise and the normal components are enhanced whereas the streamwise remained unaffected for small changes.

A counter-current air-water flow having a flat interface resembling a domain with infinite depth was solved by the group of [32]. Pseudospectral method along with Adams-Bashforth and Crank-Nicholson schemes were the numerical methods that used to solve

the equations of motion. The interface is coupled via the continuity of velocity and continuity of tangential and normal stress balance. A pressure gradient is used to drive the flow in opposite directions. The group simulate air and water flow with both the phases having same Re_τ.

The group of [17] solved the unsteady NSE by a DNS for a Re of 3300. Statistical correlations were studied to choose the required dimensions of the computational domain, confirming that all the essential scales of turbulent structures are resolved. Unlike [1] the group of [17] solved the equations using a spectral element method which solves the equations on a Fourier space, although the same time iteration scheme was used. Upon validating with experimental data, the statistics were agreeable. Although some of them (Reynolds, normal and shear stresses) remained under-predicted and attributed to the fact that a smaller frictional velocity u_τ was imposed. [36] used the data from the simulations of [17] to particularly study the individual components of the budgets of Reynolds stresses which contribute to the total TKE budget in the channel. An important inference was that the turbulent budgets become more important in the near-wall region than in the bulk, where they are almost constant. This is due to the well-known fact of the enhanced turbulence action in the near-wall region. By studying each of the budget terms in detail, an interesting conclusion was drawn that the dissipation rate is almost balanced by the production near-wall Moreover, the rate of dissipation was highly dependent on the Reynolds number. Usually, the pressure term in the budget can be split into a strain and a correlation term, but upon using an inhomogeneous boundary condition, they found that this pressure term could then be decomposed into an additional third term which reveals significant conclusions.

One of the inferences from the previous chapter is that the water phase perceives air like a free surface and how the structures aligned to resemble open channel flows. To get some idea about the trends in OCH (open channel flows), a brief summary is provided, as we wish to compare the simulations in the water side with OCH data. The group of [51] performed DNS of open channel turbulent flow to examine the Froude number effect. Equations were solved by finite differences. The study characterizes the domain in 3 regions where the stress distributions are contrasting. They also discuss that the vorticity at the free surface is substantially different. A small Froude number dependence on the pressure strain correlation budget was seen. The group of [62] also studied the effects in the turbulent flow due to a high Froude number. Interestingly, they simulate for a setting where the upper fluid is freely sheared which moves in the opposite direction, closely resembling the setting we want to simulate. Unfortunately, the budgets are not discussed making it a bit difficult to compare the budgets. They observed large scale motions near the free surface causing some streaky structures, which confirmed actions of vorticity.

Another group ([21]) conducted a DNS for an open channel flow with zero mean shear at the free surface. They use a higher order finite difference method to solve the equations. A Re_τ of 160 was chosen and the flow was driven by a non-dimensional pressure gradient. The turbulent streamwise and spanwise intensities were higher near the

free surface Upon examining the budgets they see that the pressure strain re-distributes the TKE from the normal direction to the streamwise and spanwise directions. They compared the results with an experimental data and showed that the implemented model had a good agreement.

This chapter aims to study the turbulent statistics and budgets for a counter current pressure driven stratified flow with a flat interface. Due to the lack of simulation data and qualitative research for this setting, it is quite hard and not straightforward to validate the implementation. Based on the conclusions drawn from the previous we wish to compare the data accordingly. Instead of studying shear driven channels, for this setting, we study pressure driven channels. Hence, the air side data is compared with single phase turbulent channel data from [1]. The water side having similarity with open channels, the data is compared to [21]. Of course due to the coupling present at the interface, these cases cannot be validated. But they are only be compared with the respective cases and the differences are highlighted (if any).

6.1. NUMERICAL METHODOLOGY

This section provides a description and the numerical methods implemented to solve the counter current setting. The similarities in the methodologies with the previous chapter is highlighted. Additional efforts required in order solve the problem is discussed and the following modelling is elaborated with a derivation.

The last two chapters dealt with fluid flows driven by shear. In this chapter, we take a different step and solve a pressure driven two phase channel. As the name of the chapter suggests, the stratified flow is chosen to have a counter current setting. A stretched channel separated by wall distanced at $2H$ (where H is the half height) is chosen. x, y and z are chosen as the reference axis having velocity components u, v and w. u is in streamwise direction whereas v and w are in the normal and spanwise direction respectively. We choose air to move in $+x$ direction (from left to right) and water to move in $-x$ (from right to left) direction, as seen in figure 6.1. Similar to the previous chapter, air is stratified on top of water due to the difference in density and the interface remains flat and stationary throughout the simulation. The governing equations for the system having this setting of multiphase flow is same as equations 5.1, with the density and viscosity fractions.

Although not proven (in this thesis), a few advantages of disregarding the VoF method was briefed fairly in the previous chapter. Considering this we do not wish to solve the VoF equation in this chapter as well, but follow the same methodology taken in the last chapter to solve the multiphase system. Hence, to close the system, the continuity of shear and velocity (equations 5.3, 5.2) are imposed as the interfacial conditions. Although the performance and comparison of VoF method and the approach taken in this thesis would be definitely interesting to see in future works. This chapter also aims to highlight the differences in the co-current and the counter-current setting (if there are any). Hence, fluids with the same properties as listed in 5.1 are used for the simulating the counter-current flow as well.

Periodic boundary conditions are applied in the streamwise and the spanwise direction. The boundary conditions at the walls in the normal directions are constrained to have a no-slip condition similar to the co-current flow. But the wall velocities are set to zero. Hence, $U = 0$ at both top and bottom walls. The length of the computational domain in each direction was $L_x \times L_y \times Lz = 2 \times 2H \times$. Equations of mass and momentum as solved with the FVM framework. The convection term was discretized with a central difference operator. A 3 stage (RK-3) Runge-Kutta method was used to integrate the equations in time. To ensure convergence, a CFL = 0.4 was used.

The mesh is constructed in the same way as illustrated in the previous chapter. The same algorithm is used to construct a geometrically graded mesh which has refined cells near walls and near the interface. The mesh statistics for this test case is already presented in Table 5.2. Only a limited amount of time was available to test out the counter-current setting. M8 has approximately 16.7M cells and took quite an amount of CPU time (not shown here) for the the co-current case. Assuming that the counter-current case would roughly take the same amount of time on a M8 mesh, simulations for a M8 was disregarded due to the lack of time. Thus the simulations were performed on a M7 mesh, for which the results are presented in the next chapter.

Since we wish to use the same solver, physical conditions and different scalings the constraints posed by the solver (as discussed in the section 5.1) forces us to additionally model the few terms of NSE at the interface as elaborated in section 5.2). Each of the phase is again solved in it's own scaling. The frictional Reynolds numbers belonging to each of the scaling are then $Re_\tau^a = 360$ and $Re_\tau^w = 160$. The convective flux at the interface is set to zero. The pressure across the interface is set to have a homogeneous Neumann condition. The diffusive fluxes are computed by re-scaling the gradients to have the units of the phase which it belongs to.

Apart from these efforts, since we choose a pressure driven channel, the respective pressure gradients that drive the flow should be derived. The group of [32] and [1] use a non-dimensional pressure gradient $\Pi = -\frac{1}{\rho}\frac{\partial \overline{p}}{\partial x} = 1$ to drive the flow. The former research group chooses to solve with the fractional time step iteration method and the latter solves a single phase problem as such. Both of the groups use an identical pressure gradient, but neither of them show the computations behind it. Considering the approach that we take, i.e to solve the system together, the pressure gradient computation would not be straight forward since it would have different definitions across these two phases. The upcoming section considers the different scalings, makes use of the NSE to arrive at relations that form a system of equations and finally solves for two pressure gradients of different scales which are then used to drive the air and water phase in respective directions.

6.1.1. MATHEMATICAL MODELLING AND SETUP

As it is a well known fact that turbulence is dissipative, it is necessary to drive the channel with a pressure gradient in the direction of the mean flow through a periodic boundary

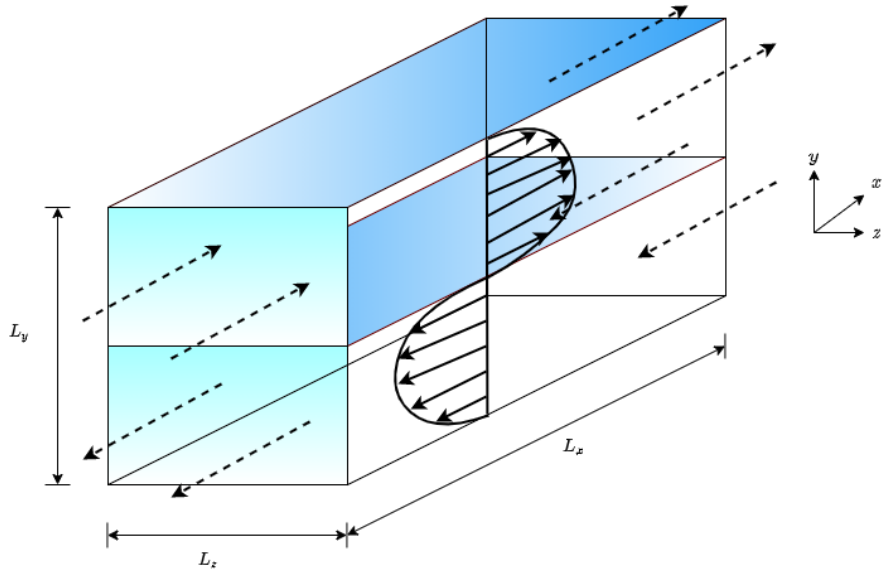

Figure 6.1: The computational domain and the physical problem to be solved

so that the flow and the turbulent nature does not completely dissipate. As discussed previously, the pressure gradient appears 'naturally' from the NSE. Hence, a good starting point to derive the required pressure gradient would be the NSE itself. Since we need to drive the flow in the streamwise direction, we look at the x-momentum equation.

$$\partial_t u^* + (u^* \cdot \tilde{\nabla}) u^* = -\tilde{\nabla}_x \tilde{p^*} + \mu^* \frac{\partial^2 u^*}{\partial x^2}$$
$$\tilde{\nabla} \cdot u^* = 0$$
$$\partial_t u^\dagger + (u^\dagger \cdot \tilde{\nabla}) u^\dagger = -\tilde{\nabla}_x \tilde{p^\dagger} + \mu^\dagger \frac{\partial^2 u^\dagger}{\partial x^2}$$
$$\tilde{\nabla} \cdot u^\dagger = 0$$

Due to the reasons discussed in Section 5.2.2, in the derivation of pressure gradients, considering the boundary conditions, we see that the pressure gradients are exactly balanced by the viscous forces. We have,

$$\frac{\partial p^*}{\partial x} = \mu^* \frac{\partial^2 u^*}{\partial y^2}$$

and

$$\frac{\partial p^\dagger}{\partial x} = \mu^\dagger \frac{\partial^2 u^\dagger}{\partial y^2}$$

Since the pressure gradient is to be driven throughout the channel, we integrate it over the domain, $\Omega_a \in [0,1]$ for air and $\Omega_w \in [-1,0]$ for water. We get,

$$\int_0^1 \frac{\partial p^*}{\partial x} = \mu^* \int_0^1 \frac{\partial^2 u^*}{\partial y^2} \tag{6.1}$$

$$(1)\frac{\partial p^*}{\partial x} - (0)\frac{\partial p^*}{\partial x} = \mu^* \left.\frac{\partial u^*}{\partial y}\right|_{top} - \mu^* \left.\frac{\partial u^*}{\partial y}\right|_{int} \tag{6.2}$$

$$\frac{\partial p^*}{\partial x} + \mu^* \left.\frac{\partial u^*}{\partial y}\right|_{int} = \mu^* \left.\frac{\partial u^*}{\partial y}\right|_{top} \tag{6.3}$$

Similarly for water phase, we have:

$$\int_{-1}^0 \frac{\partial p^\dagger}{\partial x} = \mu^\dagger \int_{-1}^0 \frac{\partial^2 u^\dagger}{\partial y^2} \tag{6.4}$$

$$(0)\frac{\partial p^\dagger}{\partial x} - (-1)\frac{\partial p^\dagger}{\partial x} = \mu^\dagger \left.\frac{\partial u^\dagger}{\partial y}\right|_{int} - \mu^\dagger \left.\frac{\partial u^\dagger}{\partial y}\right|_{bot} \tag{6.5}$$

$$\frac{\partial p^\dagger}{\partial x} - \mu^\dagger \left.\frac{\partial u^\dagger}{\partial y}\right|_{int} = -\mu^\dagger \left.\frac{\partial u^\dagger}{\partial y}\right|_{bot} \tag{6.6}$$

6

With this, we already have four unknowns, $\frac{\partial p^*}{\partial x}$, $\frac{\partial p^\dagger}{\partial x}$, $\left.\frac{\partial u^\dagger}{\partial y}\right|_{int}$ and $\left.\frac{\partial u^*}{\partial y}\right|_{int}$. Hence we require 2 more equations to close the system and solve the equations. Hence we look at other relations which could possibly help to solve the system. Next, we also know that the shear stresses are continuous,

$$\mu_a \frac{\partial u}{\partial y} = \mu_w \frac{\partial u}{\partial y} \tag{6.7}$$

Hence the non-dimensional stress continuity reads

$$\mu_a u_\tau^a \frac{\partial u_j^*}{\partial y} = \mu_w u_\tau^w \frac{\partial u_j^\dagger}{\partial y} \tag{6.8}$$

Which gives,

$$\mu_a u_\tau^a \frac{\partial u^*}{\partial y} - \mu_w u_\tau^w \frac{\partial u^\dagger}{\partial y} = 0 \tag{6.9}$$

Pressure gradients added to the system will bring out distinct features to the statistics studied. There might be number of factors upon the dependency of the pressure gradients. But for simplicity, it is assumed that the pressure gradient chosen should be uniform throughout the channel. But it is important to ensure that the uniform pressure gradient chosen should be equal in magnitude, but have different signs to drive the flow in opposite directions. Hence,

$$\frac{\partial p^*}{\partial x} = -\frac{\partial p^\dagger}{\partial x} \tag{6.10}$$

With this, equations 6.3, 6.6, 6.9, 6.10 forms a system of linear equations, which could be easily solved to find the respective unknowns. But before moving onto solving the system, simplifying some of the known quantities would be helpful to strongly represent the matrix formed from the linear system.

From equation 6.3, we can approximate $\mu^* \frac{\partial u^*}{\partial y}\Big|_{top}$, which basically is the wall shear stress at the top wall. Starting from the dimensional wall shear stress,

$$\mu_a u_\tau^a \frac{\partial u^*}{\partial y} = \mu_a \frac{\partial u}{\partial y} \tag{6.11}$$

$$= \tau_w \tag{6.12}$$

$$= u_{\tau,a}^2 \rho_a \tag{6.13}$$

Hence,

$$\frac{\partial u^*}{\partial y} = \frac{u_\tau^a \rho_a}{\mu_a} \tag{6.14}$$

$$= \frac{\rho_a}{\mu_a} \frac{\mu_a Re_\tau^a H}{\rho_a} \tag{6.15}$$

$$\frac{\partial u^*}{\partial y} = Re_\tau^a \tag{6.16}$$

$$\mu^* \frac{\partial u^*}{\partial y} = \mu^* Re_\tau^a \tag{6.17}$$

$$= 1 \tag{6.18}$$

Hence, re-writing equation 6.3, gives

$$\frac{\partial p^*}{\partial x} + \mu^* \frac{\partial u^*}{\partial y}\Big|_{int} = 1 \tag{6.19}$$

$$\tag{6.20}$$

In the same way, we can approximate the bottom wall shear stress,

$$-\mu^\dagger \frac{\partial u^\dagger}{\partial y} = -1$$

We can now re-write equation6.6 as

$$\frac{\partial p^\dagger}{\partial x} - \mu^\dagger \frac{\partial u^\dagger}{\partial y}\Big|_{int} = -1 \tag{6.21}$$

We can also try to re-arrange equation6.9 by inspecting the coefficients

$$\mu_a u_\tau^a = \mu_a \frac{\mu_a Re_\tau^a H}{\rho_a} \tag{6.22}$$

$$= \frac{\mu_a^2 Re_\tau^a}{\rho_a H} \tag{6.23}$$

Similarly,

$$\mu_w u_\tau^w = \mu_w \frac{\mu_w Re_\tau^w H}{\rho_w} \tag{6.24}$$

$$= \frac{\mu_w^2 Re_\tau^w}{\rho_w H} \tag{6.25}$$

$$\tag{6.26}$$

Putting equations 6.216.206.10 and 6.9, we can write a linear system of a format, $Ax = b$ with,

$$\begin{bmatrix} 1 & 0 & \mu^* & 0 \\ 0 & 1 & 0 & -\mu^\dagger \\ 0 & 0 & \frac{\mu_a^2 Re_\tau^a}{\rho_a H} & -\frac{\mu_w^2 Re_\tau^w}{\rho_w H} \\ 1 & 1 & 0 & 0 \end{bmatrix} \begin{bmatrix} \frac{\partial p^*}{\partial x} \\ \frac{\partial p^\dagger}{\partial x} \\ \frac{\partial u^*}{\partial y}\Big|_{int} \\ \frac{\partial u^\dagger}{\partial y}\Big|_{int} \end{bmatrix} = \begin{bmatrix} 1 \\ -1 \\ 0 \\ 0 \end{bmatrix} \tag{6.27}$$

which gives the required pressure gradients in each phase to be

$$\begin{bmatrix} \frac{\partial p^*}{\partial x} \\ \frac{\partial p^\dagger}{\partial x} \end{bmatrix} = \begin{bmatrix} 1 \\ -1 \end{bmatrix} \tag{6.28}$$

Hence, a non-dimensional pressure gradients (ref 6.28) is added as a source term in the NSE, that drives the flow with the respective derived values either in the $+x$ or $-x$ direction.

6.2. RESULTS

This section discusses the results of simulations performed for the counter-current flow modelled in the previous section. The structure of discussions is similar to previous chapters. The characteristics of the averaged flow is explained, followed by r.m.s values due to fluctuations. Then the Reynolds stresses in each of the phase is shown. Finally, the budgets and the flow structures are elaborated. This chapter is not a straight-forward extension from the previous chapters since the mechanism of driving the flow, the boundary conditions, the direction of the flow in each phase are significantly different. This may bring out contrasting inferences on the flow, which are briefly explained, if there are any. The statistics presented are also compared along with a single phase channel results of [1] for the air side and [21] for the water side, with each phase having the same Re_τ as the reference case(s).

The same averaging procedure is followed as in the previous section. With two scalings involved, the gradient computed during the local time averaging is also re-scaled to have respective units of the phases as illustrated in the section 5.4.1. The snapshots stored are then ensemble averaged and the results are presented in the upcoming sections

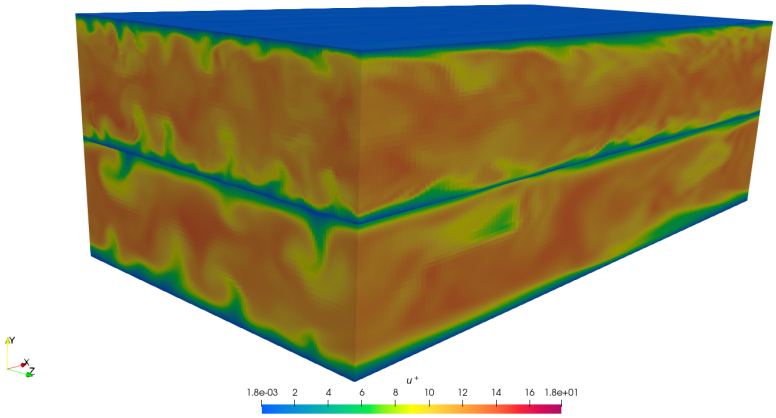

Figure 6.2: Instantaneous velocity at $t^+ = 75$. Air which is on the top moves in the $+x$ direction and water moves in the $-x$ direction.

6.2.1. MEAN FLOW AND FLUCTUATIONS

Visualisation of the instantaneous velocity field is shown in Figures 6.2. The snapshot is shown for a M7 mesh. Air flows in the $+x$ direction and water in $-x$ direction. The flow in air phase seems to be a bit more turbulent with an incoherent flow pattern when compared to the water side motion. The interface is kept flat, and seems to closely have a zero valued no-slip condition. From the colour map/legend, we can see that different regions in the flow are uniform (in magnitude). Near the top wall, bottom wall and the interface, the velocities are comparable and either have a zero velocity or have a velocity close to zero. But away from these regions, for most of the flow, the velocity is comparable and uniform in magnitude. This is typically observed in single phase turbulent channel flows due to a uniformly varying shear stress at wall and in the bulk.

Figure 6.3 shows the mean velocity profiles for air side on top axis and water on the bottom axis. Both the phases represent the dimensionless velocities, non-dimensionalised by their frictional velocities. The same physical parameters are used, which means that the scaling factor $\mathscr{S}$, holds the same definition. The air side clearly reproduces a symmetric parabolic velocity profile of a turbulent channel flow. Due to the friction at top and bottom walls, the velocity is zero, also satisfying the boundary condition. The flow attains a maximum speed of $\langle u^* \rangle = 17.8$ at the center line where the planar shear stress is expected to be at the minimum. The velocity profile is compared against the channel data of [1] of $Re_\tau = 360$ and seems to have a similar behaviour as a single phase channel flow. The water side is not compared with the reference data due to unavailability of data. The water side also reproduces the parabolic velocity profile as seen in a channel flow at high Re_τ. A maximum velocity of $\langle u^\dagger \rangle = 17.5$ occurs at the center line of the channel. Interestingly, unlike the air phase the interface velocity of water is non-zero. This non-zero velocity at the interface hints that the friction at the interface is not as high as the friction at the bottom wall for the water side. When moving to the air side,

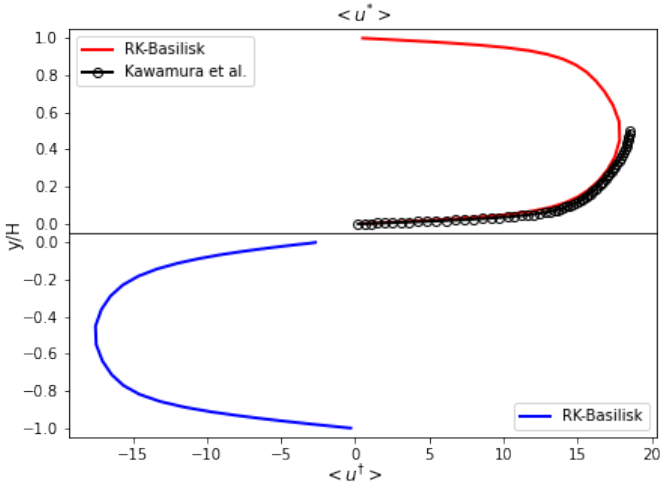

Figure 6.3: Mean velocity profiles for air(top) and water(bottom) phase. Air side data is compared against the single phase results from [1]

friction at the interface and the top wall seem to be comparably same, but higher than what is seen in the water side, since the velocities typically go to zero.

From the visualisation and discussions of the instantaneous field and the mean velocity profile, we see that the near wall region has a high shear rate, thus the flow around walls are subjected to high gradients. These gradients are shown for the mean streamwise velocity across the channel in the wall normal direction in Figure 6.4.

As shown in the previous chapter, the non-dimensional shear continuity holds (refer equation 5.28). Consequently gradients in the air side are higher than the gradients in water. In the regions $-1 < y/H < 0.9$ and $0.1 < y < 0$, the gradients are typically higher, than in the bulk flow $0.9 < y/H < 0.1$. Unlike stratified Couette flows, these flows don't always have a positive gradient. In pressure driven channels, due to distribution of shear stress, the gradient across the center line of the channel also takes different signs. The gradients seen in the water phase are not as sharp as the gradients in air side. which might cause the flow in the water side to less turbulent than in the air side.

The mean velocity profile in the logarithmic scales are presented in Figure 6.5 for the near interface region in the air side and are compared with the single phase turbulent flow simulation of [1]. We see a similarity in the logarithmic behaviour of the velocity profile simulated for this test case, highlighting the similarity with a boundary layer associated to a wall. The velocity profile has a small deviation from the reference case. The velocity at the interface in our test case, does not necessarily start from 0. One reason that there is a small deviation in this logarithmic plot could be that the boundary layer is

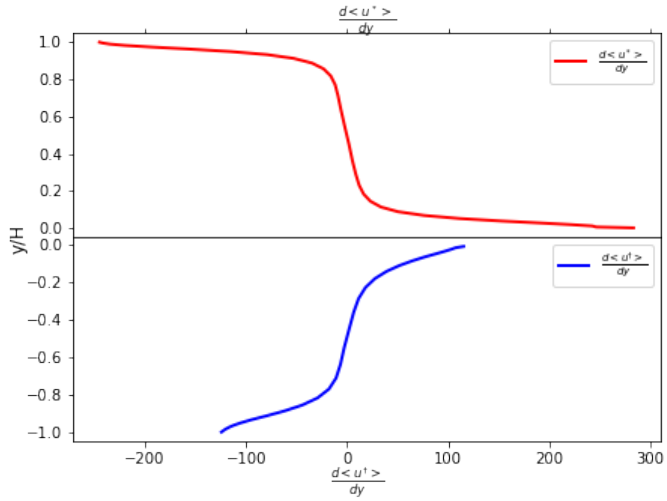

Figure 6.4: Two phase mean streamwise gradient for the air phase shown at the top and water on the bottom

not resolved well enough. We saw that a M7 mesh already was a coarse mesh for simulating a two phase flow from the previous chapter. A M8 mesh still needed a smaller Δy^+ to resolve the layers up to the smallest level. Since the statistics for this case is presented on a M7 mesh, the inadequacy of the mesh to resolve the boundary layer for this two phase problem is evident from Figure 6.5.

The r.m.s fluctuations, $u_{i,rms} = \sqrt{\langle u_i u_j \rangle}$ for all 3 components of velocity is shown for both the phases. The air side fluctuations reach a maximum value in the near wall region whereas the fluctuations are smaller at the center line. This indicates that the turbulent shear stress and hence the budgets would typically have lower values in the bulk. This is contrasting to what was seen in the co-current Couette flow simulation. Again, reference data is shown only for half of the domain due to the symmetricity. For the streamwise fluctuations, the test case has similarities with the reference. But the presence of an interface and the shear caused by it reduces the spanwise and the normal fluctuations. The streamwise and the spanwise fluctuations at the interface in the water side do not die out due to a "shear-free-like" surface. This was also one of the common observations in the co-current Couette flow. The fluctuations of the normal velocity component has a zero value at the interface due to the numerical method adopted previously. For the same Re_τ used in an open channel flow, the fluctuations in the spanwise and the normal direction seem to be smaller for the test case. This points out that the shear felt by water in two phase flow is not as low as shear felt by water in an actual open channel flow. Hence, in both the domains, the spanwise and the normal fluctuations are smaller when compared to their respective reference cases who simulate for the same Re_τ as the test case.

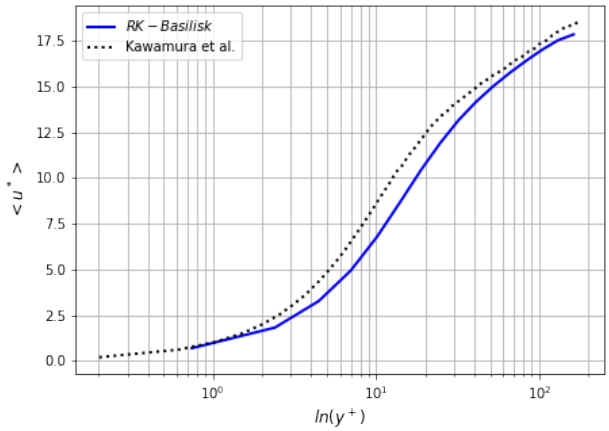

Figure 6.5: Mean velocities in the logarithmic scales for the near-interface in the air side

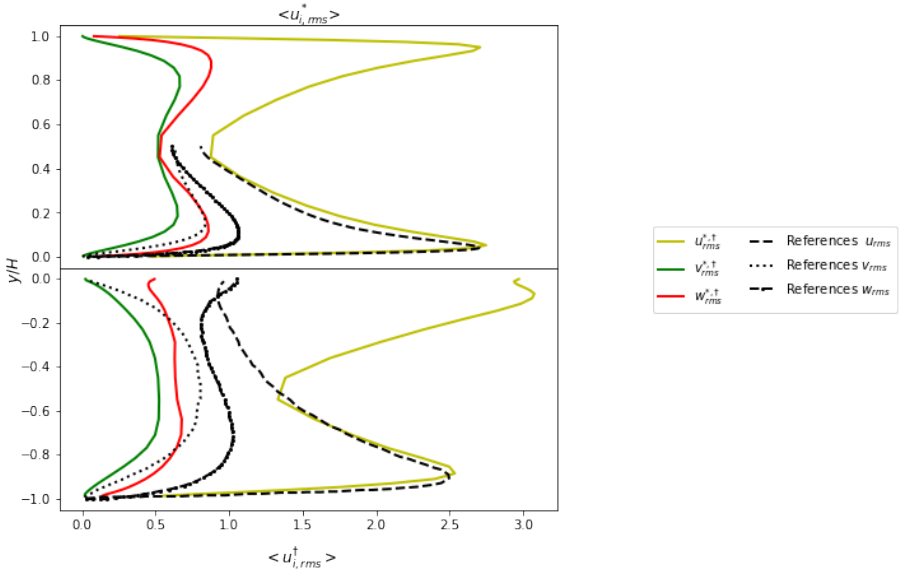

Figure 6.6: R.m.s velocity fluctuations shown for both air and water phase. The values are compared against the single phase channel data for the air side and open channel flow for the water side

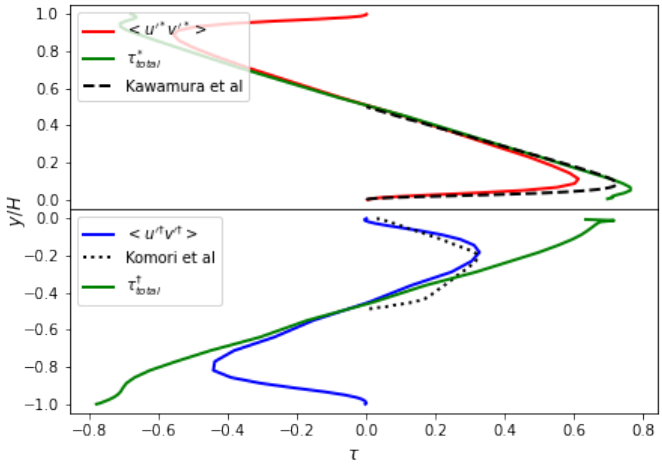

Figure 6.7: Reynolds and total shear stress for air and water phase. The Reynolds stresses are compared with the reference data set

Apart from these observations, an overall similarity with the co-current Couette flow case can be noticed. The fluctuations in the air side have profiles close to a single phase turbulent channel. The wall at the top side forces the fluctuations to die out to zero. At the other side, i.e at the interface, the fluctuations also die out. This confirms that a high shear is imposed by the water side on the air side which makes the interface feel like a 'immobile' wall for the air side. Additional shear effects come into the play since water moves in a direction opposite to air. Due to this configuration, the friction at the interface is even higher when compared to two fluids moving in the same direction. The additional friction/shear felt in the air imposed by the water side, certainly affects the turbulent velocity fluctuating components in the air phase and the water phase. But we see that for this choice of Re_τ^a and Re_τ^w, water still feels air like a shear free surface.

6.2.2. REYNOLDS STRESSES

The Reynolds stresses and the total planar shear stress is shown in Figure 6.7.Naturally, the Reynolds stresses naturally show a higher value near walls and near the interface than at the center of the channel. The turbulent shear stresses on the air side are proportionally higher than the water side. This purely seems to be a Reynolds number effect. [1] ran simulations for different Re_τ and saw that the turbulent shear stress grows in proportion with the frictional Reynolds number used. Hence, the stresses in the air side higher than what is observed in the water side.

They Reynolds stresses attain a maximum value of 0.6 at $y^+ = 22.7$ and seem to be symmetric across the center line of the air side channel. The stress at the center line however is 0. The values are compared against a wall bounded simulation from [1]. With the presence of an interface, the shear imposed on the air-side seems to be different from

the wall and hence the turbulent shear stresses are slightly lower when compared to this reference case. The Reynolds stresses for the water side peak at $y^+ = 17$ (from the bottom wall) with a value of approximately 0.45. Unlike the air side, the stress is not symmetric. The stress near the interface peaks with a value of 0.25, almost half of the stress at the bottom wall.

The total shear stress in each of the phases are also shown in the same figure. Unlike Couette flows that have a constant shear stress of unity, the stress in the turbulent pressure driven channel flow is not constant, but varies linearly across the center line. It could be summed up as the contributions of Reynolds stresses and viscous stresses, as in equation 5.31. From the profiles obtained, we see that a maximum planar shear stress is at the walls and at the interface. The contribution of Reynolds stress and the viscous stress add up to a value of 0.8 in non-dimensional units for both the phases, whereas at the center line, the stress is zero. The deviation of the Reynolds stresses from the total shear stress is compensated by the the viscous shear stress and vice versa. This brings out the balance in the equation 5.31. Thus, this is also a good indicator that the flow is statistically steady [1].

6.2.3. TKE BUDGETS

The turbulent kinetic energy and the individual terms which form the budgets of TKE are discussed in this section. Initially the kinetic energy in the channel is shown. Next, the individual terms comprising the budget of TKE are discussed to compare the air and water phase and also highlight differences with the reference case. Following this, the budgets are altogether represented in one scale to explain about the TKE balance between different terms and redistribution of TKE.

Figure 6.8 shows the turbulent kinetic energy, $k = \frac{1}{2}(\langle u'u' \rangle + \langle v'v' \rangle + \langle w'w' \rangle)$ in both the phases. The peaks of the turbulent kinetic energy is explained by the peaks in the fluctuating velocity components localised near the interface and the near wall region. The TKE in the air side is symmetric across the center line where it is at the lowest. The TKE seems to be re-distributed from the center line of the channel towards the interface and towards the wall. This symmetric distribution of TKE is not observed in the water phase. The TKE is different at different regions of the flow. In the vicinity of the bottom wall, TKE reaches a maximum of 3.4 in non-dimensional units. At the center line of the channel, the TKE a low value. But the value of TKE at the center line of the water phase is higher than the air phase. But as we move towards the interface, the TKE has the maximum value in the entire channel. Thus, the turbulent kinetic energy progressively increases more towards a "shear-free-like" surface and certainly has a non-zero value at that surface, and thus for this test case is the interface itself.

The individual terms that make up the budgets of TKE are shown in Figure 6.9. Figure 6.9(a) shows the production in both the phases. Production in the air phase is observed to be higher than the production in the water phase. This as discussed earlier, is purely a Re_τ effect. The production term is a product of the turbulent shear stress and the mean velocity gradient. The turbulent shear stress is known to scale up with increase in Re_τ in pressure driven channel flows [1]. With $Re_\tau^a > Re_\tau^w$, the production in the air phase is

significantly higher. This is something which is not observed in sheared Couette flows, as the maximum value of production stays at 0.25 as $Re_\tau \to \infty$. Upon comparing these production values with their respective reference cases, with the presence of an interface separating a counter-current flow, the production terms seem to be lesser in each phase.

Next, the pressure diffusion values are shown in Figure 6.9(b). The pressure diffusion values have very high gradients near the interface. The magnitude of velocity fluctuations which primarily forms the terms of the TKE budgets, cannot be associated with such high magnitudes in the values of pressure diffusion which makes it conclusive that the terms in the budget are computed incorrectly. Moreover, the pressure diffusion values are the lowest among the other budget terms. Upon close examination, the pressure diffusion values are also higher near the top and bottom walls. The boundary condition for the gradient computation for this budget term might be incorrect due to which they show high values at the walls. Similarly, an incorrect rescaling across the interface might have led to this unphysical gradient near the interface. The aforementioned reasons were neither quantified nor confirmed and remain uncertain. As mentioned earlier, due to insufficient time, this problem was not debugged and thus opens a way for an improvement for this counter-current model.

Figure 6.9(c) shows the diffusion in the two phase flow due to transport of velocity fluctuations. With the theory established about transfer of TKE with respect to positive and negative peaks from the previous chapter, we see that, in air-phase only a small amount of kinetic energy is transported from the near interface region towards the bulk in the water phase.

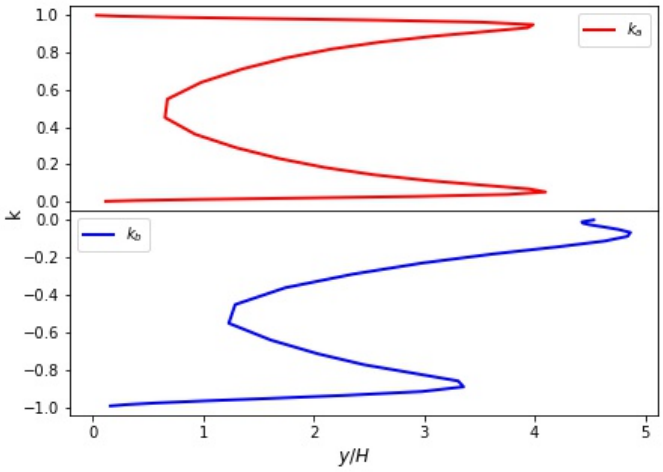

Figure 6.8: Turbulent kinetic energy in both the phases. Upper axis represents the air phase and the bottom axis represents the water phase

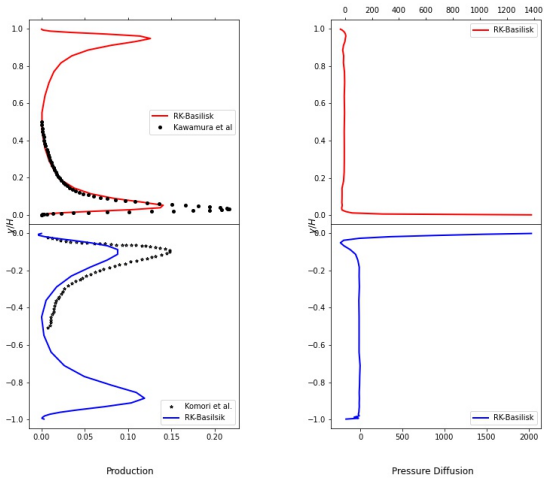

(a) **(b)**

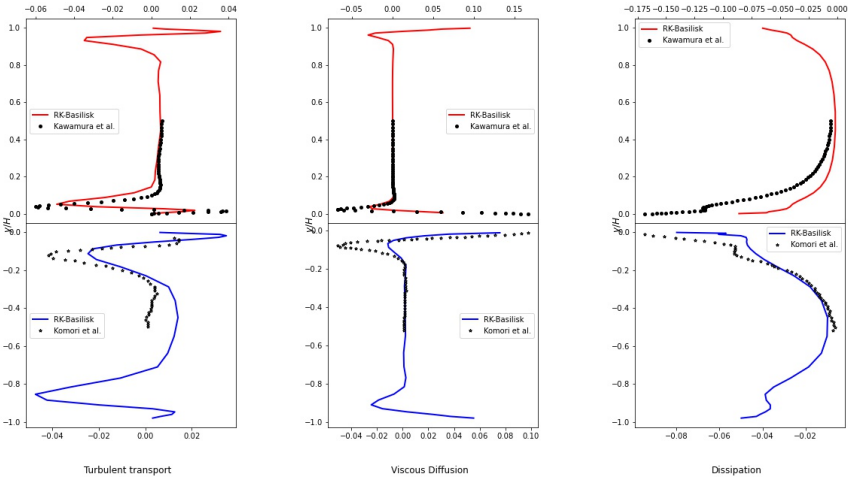

(c) **(d)** **(e)**

Figure 6.9: Individual terms in the budget equation 4.20 for both the phases of **(a)** Production **(b)** Pressure diffusion **(c)** Turbulent transport **(d)** Viscous diffusion **(e)** Dissipation. Solid blue lines represent the water phase, compared against [21] and red lines represent the air phase compared against [1] .

Figure 6.9(d) show diffusion due to viscous effects. The air side has similarities with the classical wall bounded turbulent flow. But in the water side, as seen in the Couette flow situation, high viscous diffusion is observed. Comparing the diffusion terms, kinetic energy seems to be transported more due to viscosity effects than velocity fluctuations.

The dissipation budget of TKE is presented in Figure 6.9(e). Upon comparing the test case with the reference case in the air-side, the dissipation is comparatively higher. The near interface dissipation in the air side is comparable to the dissipation at the top wall and hence does not behave differently near the interface. But in the water phase, dissipation gradually increases towards the interface and has a 'dip' in the near interface region. Thus, the dissipation near the interface is higher, similar to what is observed in an open channel flow. [21].

The terms in the TKE budget are altogether represented in one scale in Figure 6.10. The top axis represents the air phase, which is compared with its reference case of [1] and the bottom axis shows the budgets of the water phase compared with its reference case of [21]. Since the pressure diffusion values present unphysical gradients as a result of incorrect computations, it is not shown here. The budgets in both the phases seem to be localised in the near wall and the near interface region. i.e, $y^+ < 20$ from the walls and from the interface. The budgets in the air phase are comparable to a wall flow in the interface region although the magnitude of budgets in the reference case near an actual wall having the same Re_τ are higher. This fact is also highlighted in [14] who compared the air side motions with a wall bounded flow. This says that the turbulent fluctuations are damped in this near interface region in the gas phase, due to a high shear present at the interface imposed by water moving in the opposite direction. Generally, a good balance is seen between the terms in the budgets in the air side. The production almost balances dissipation near the interface and also in the core flow. The kinetic energy is extracted from the mean flow and redistributed by the diffusion terms towards the wall and the interface. In the water phase, the terms in the budget near the interface do not resemble the wall behaviour. Turbulent dissipation is much higher. Smaller values in the diffusion terms show that there is more diffusion from the interface towards the mean flow. Dissipation in the bulk is seemed to be balanced by the transport term and balanced by viscous diffusion just at the interface. But near the interface, with production being small (for this particular choice of Re_τ^w) and dissipation being of the same magnitude, there is a balance between production and dissipation. [14] and [32] report that there is a general imbalance in the budgets, but this is because they simulate both the phases with the same Re_τ. In this case, the production in both the phases will be of the same magnitude, but still having a high dissipation (due to a "shear-free-like" surface) near the interface of water. This leads to the dissipation not being balanced by the production in the near wall region, which is what was reported. But in our case, we do not see this, as we simulate two different Re_τ, therefore modelling up to a more realistic scenario. The kinetic energy which is redistributed from the bulk towards the interface, has a non-zero value exactly at the interface, causing few of the budget terms with viscous mechanisms to having similarities with a shear free surface.

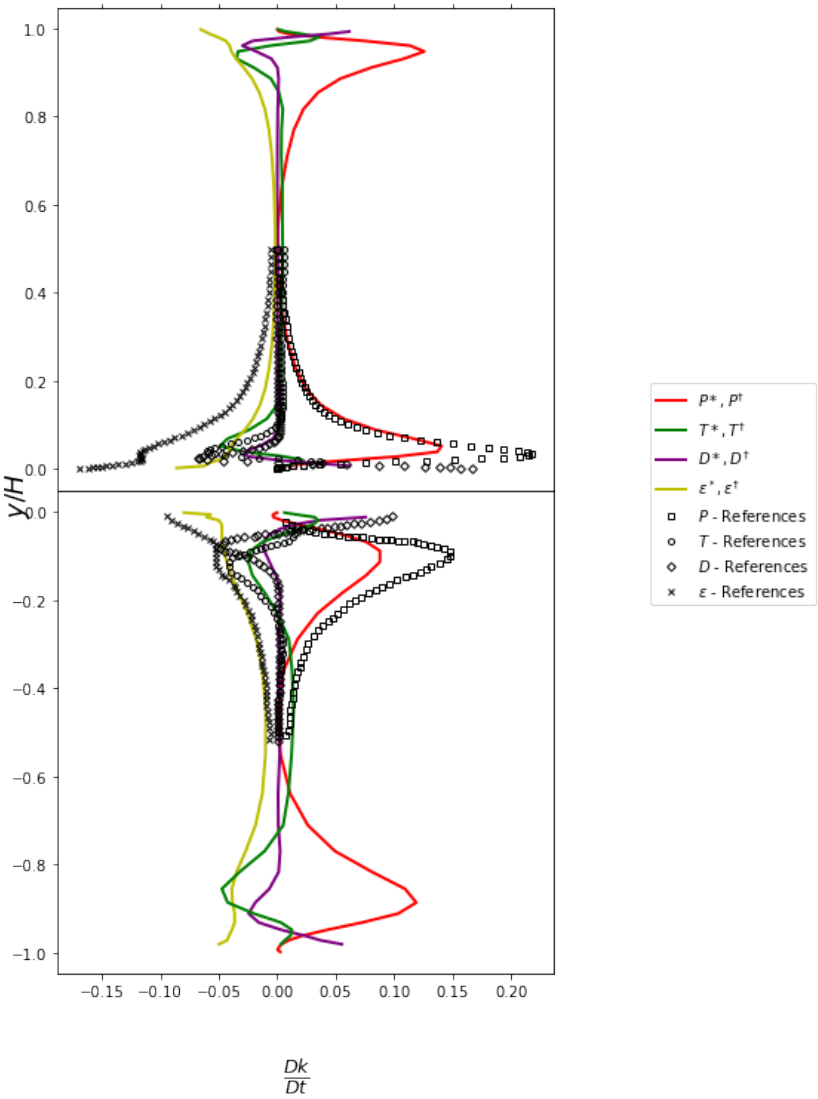

Figure 6.10: Turbulence kinetic energy budget in air-phase (top) and water-phase (bottom)

7

CONCLUSIONS

The work presented in this thesis illustrates a systematic approach towards developing a Direct Numerical Simulation for a stratified turbulent two-phase flow configuration. The developed simulation tool was primarily based on NRG's solver RK-Basilisk. Three different test cases were studied, each of which are explained in different chapters of this thesis, were compared and validated against literature.

Initially, a turbulent single phase flow was studied in order to have a good understanding and to form a solid basis while modelling turbulent two phase flows. A shear driven Couette flow configuration was chosen and modelled in RK-Basilisk. To have multiple resolutions through the grid, the geometric grading strategy used for meshing was discussed. Upon performing a mesh independence study, an adequate grid which resolved the boundary layers fairly well was identified. The computed lower order and higher order statistics which were compared against the data from [56], were shown to have a good agreement. The various analyses provided the necessary theoretical background for the interpretation of results for the two phase problem. We also observe that RK-Basilisk which uses lower order FVM, captures the turbulent activities near the wall very well and thus performs as good as the simulations of [56] who use higher order schemes like spectral methods.

Next, a DNS is performed for a stratified two phase turbulent co-current Couette flow configuration and the model implemented in RK-Basilisk is validated against simulations of [31]. True air-water ratios are chosen which leads to the frictional Reynolds being 'coupled' which then give rise to different spatial and temporal scales, and thus opens the problem to a more realistic situation. We see that there are a few constraints posed by the solver due to its inflexible nature to solve with fractional iteration method, thus forcing us to solve the air-water flow 'together'. When true air-water ratios are used, solving the problem 'together' poses another constraint, i.e, gradients just across the interface involves variables of different scales. Thus these constraints are overcome by developing a general mathematical framework which involves some reformulation in the terms of

the Navier-Stokes at the interface so that it "treats" interface as a boundary to replicate as if two single phase problems are solved together,coupled at the interface. The meshing strategy from the single phase simulation was extended to the two phase problem such that, the two phase grid has cells clustered near interface and near walls. Upon basing the grid on the higher Re_τ, the cells belonging to the bulk region become coarse as the cell width scales with Re_τ. Due to this reason, even the mesh M8 had cells which were found to be coarse in the bulk region. Unfortunately due to the computational budgets, analyses were limited to M8 mesh. Good agreement for the lower order statistics were obtained. However, few of the computed higher order statistics had a small under prediction, which is one of the limitations in this work. Upon studying the budgets, we see that due to the strong shear at the interface, air phase perceives the water phase as a wall, whereas, the water phase sees air more like a free surface, bringing out the differences in the interfacial boundary layers. As a result, budgets of TKE in the air side resemble that of a wall and the water side resembles a free-slip layer. An overall redistribution of turbulent kinetic energy from the air phase into the water phase was observed. Finally the coherent structures in the flow were studied and the structure of the vortices revealed the high shear rate imposed at the interface. Moreover, contours of streamwise fluctuations identified regions of high and low speeds. Similarities in the contours of streaks between the interface and the water side boundary layer concludes that the interface motions were controlled by water.

Since this model of co-current flow was validated, the goal was extended to perform simulations of counter current flow as well. Simulations were performed for a pressure driven flow instead of shear driven flow. Due to the unavailability of literature for the flow configuration that is desired, each of the phases were compared with different data. With the general inference compiled from the simulation of co-current flow, air phase is 'compared' against single phase channel flow simulations of [1] and the water phase with open channel flow simulation data of [21]. The general mathematical framework developed for the co-current flow simulation was extended to this test case as well. In addition to this, pressure gradients that drive the flow in each direction was derived considering the interfacial conditions responsible for this configuration. Lower order statistics showed similarity with the respective reference cases. Moving to the higher order statistics, showed some differences with the references who simulated it for the same Re_τ. As seen in the co-current flow, due to the presence of the interface the budgets of TKE in the water side have a behaviour similar to a free surface, where the interface motions are less constrained. Regarding the gas phase, as expected, the interface budgets show the 'wall-like' similarity thereby confirming the qualitative behaviour. But there are quantitative differences in the wall similarity when compared to simulation of [1] for the same Re_τ. It is observed that the budgets of TKE were lower than what is seen in the reference case, showing that, turbulence in the air side is damped more by the presence of an interface due to high shear imposed by the water phase moving in the opposite direction.

In a nutshell, this work started with identifying a test case that would open the problem to a more realistic scenarios. The choice of simulating a co-current configuration

with true air-water ratios in their respective scaling justifies the objective. As turbulence is dissipative, there needs to be a choice of how the flow needs to be driven. Generally, fluids are driven purely by shear or by pressure. In this thesis, both the driving mechanisms for two different flow configurations were explored. Although comparing both would be naive, since the mechanism by which they are driven are different, a common conclusion about the air-water interfacial flow was seen that, the lighter phase sees the heavier phase as a wall and the heavier phase feels the lighter phase as a free surface. As to study the the near interface and near wall characteristics better, an efficient mesh was constructed by geometrically stretching and deforming the domain. Finally, after addressing the constraints in the choice of our problem, two robust benchmark DNS tools were made to simulate co-current shear driven and counter-current pressure driven flows. The simulations performed using these tools were validated using post processing and studying the budgets. Although, there were a few limitations in the cases which were addressed, this work was able to answer the research objectives formulated in the literature review phase of this thesis. In the future, this tool can be used to simulate co-current and counter-current turbulent stratified flow simulations to produce (DNS) data sets in order to support,train, or develop more coarse models such as RANS, or provide validations for such models.

BIBLIOGRAPHY

[1] Hiroyuki Abe, Hiroshi Kawamura, and Yuichi Matsuo. "Direct numerical simulation of a fully developed turbulent channel flow with respect to the Reynolds number dependence". In: *J. Fluids Eng.* 123.2 (2001), pp. 382–393.

[2] "Basilisk". In: URL: http://basilisk.fr/.

[3] Friedrich H Busse. "Bounds for turbulent shear flow". In: *Journal of Fluid Mechanics* 41.1 (1970), pp. 219–240.

[4] SI Chernyshenko and MF Baig. "Streaks and vortices in near-wall turbulence". In: *Philosophical Transactions of the Royal Society A: Mathematical, Physical and Engineering Sciences* 363.1830 (2005), pp. 1097–1107.

[5] Yun Kyung Choi, Jae Hwa Lee, and Jinyul Hwang. "Direct numerical simulation of a turbulent plane Couette-Poiseuille flow with zero-mean shear". In: *International Journal of Heat and Fluid Flow* 90 (2021), p. 108836.

[6] Milad Darzi and Chanwoo Park. "Experimental visualization and numerical simulation of liquid-gas two-phase flows in a horizontal pipe". In: *ASME International Mechanical Engineering Congress and Exposition*. Vol. 58424. American Society of Mechanical Engineers. 2017, V007T09A011.

[7] Valerio De Angelis. "Numerical investigation and modeling of mass transfer processes at sheared gas-liquid interfaces." In: (2000).

[8] JGM Eggels et al. "Direct numerical simulation of turbulent pipe flow". In: *Advances in Turbulence IV*. Springer, 1993, pp. 319–324.

[9] Yury Egorov et al. "Validation of CFD codes with PTS-relevant test cases". In: *5th Euratom Framework Programme ECORA project* (2004), pp. 91–116.

[10] Jun Fang et al. "Direct numerical simulation of reactor two-phase flows enabled by high-performance computing". In: *Nuclear Engineering and Design* 330 (2018), pp. 409–419.

[11] M Fernandino and T Ytrehus. "Effect of interfacial waves on turbulence structure in stratified duct flows". In: *Journal of fluids engineering* 130.6 (2008).

[12] EMA Frederix et al. "Reynolds-averaged modeling of turbulence damping near a large-scale interface in two-phase flow". In: *Nuclear Engineering and Design* 333 (2018), pp. 122–130.

[13] M Fulgosi et al. "Direct Numerical Simulation of Turbulence and Interfacial Dynamics in Counter—Current Air—Water Flows". In: *Direct and Large-Eddy Simulation IV*. Springer, 2001, pp. 443–452.

[14] M Fulgosi et al. “Direct numerical simulation of turbulence in a sheared air–water flow with a deformable interface”. In: *Journal of fluid mechanics* 482 (2003), pp. 319–345.

[15] Yosuke Hasegawa, Nobuhide Kasagi, and Hideshi Hanazaki. “Direct numerical simulation of passive scalar transfer across a turbulent gas-liquid interface”. In: *Proceedings, First International Symposium on Advanced fluid Information, October 2001*. 2001, pp. 696–701.

[16] Jinhee Jeong and Fazle Hussain. “On the identification of a vortex”. In: *Journal of fluid mechanics* 285 (1995), pp. 69–94.

[17] John Kim, Parviz Moin, and Robert Moser. “Turbulence statistics in fully developed channel flow at low Reynolds number”. In: *Journal of fluid mechanics* 177 (1987), pp. 133–166.

[18] Jung Hoon Kim and Jae Hwa Lee. “Direct numerical simulation of a turbulent Couette–Poiseuille flow: Turbulent statistics”. In: *International Journal of Heat and Fluid Flow* 72 (2018), pp. 288–303.

[19] Jung Hoon Kim et al. “Direct numerical simulation of a turbulent Couette-Poiseuille flow, part 2: Large-and very-large-scale motions”. In: *International Journal of Heat and Fluid Flow* 86 (2020), p. 108687.

[20] Jukka Komminaho, Anders Lundbladh, and Arne V Johansson. “Very large structures in plane turbulent Couette flow”. In: *Journal of Fluid Mechanics* 320 (1996), pp. 259–285.

[21] Satoru Komori et al. “Direct numerical simulation of three-dimensional open-channel flow with zero-shear gas–liquid interface”. In: *Physics of Fluids A: Fluid Dynamics* 5.1 (1993), pp. 115–125.

[22] Satoru Komori et al. “Direct numerical simulation of wind-driven turbulence and scalar transfer at sheared gas–liquid interfaces”. In: *Journal of Turbulence* 11 (2010), N32.

[23] Saketh Kopparthy et al. “Numerical investigations of turbulent single-phase and two-phase flows in a diffuser”. In: *International Journal of Multiphase Flow* 130 (2020), p. 103333.

[24] Pijush K Kundu, Ira M Cohen, and D Dowling. *Fluid Mechanics 4th*. 2008.

[25] Ryoichi Kurose et al. “Direct numerical simulation of turbulent heat transfer across a sheared wind-driven gas-liquid interface”. In: *Journal of Fluid Mechanics* 804 (2016), p. 646.

[26] Richard T Lahey Jr. “On the direct numerical simulation of two-phase flows”. In: *Nuclear engineering and design* 239.5 (2009), pp. 867–879.

[27] Djamel Lakehal, Sylvain Reboux, and Petar Liovic. “Sub-grid scale modelling for the LES of interfacial gas-liquid flows”. In: *Houille Blanche* 6.05 (2005), p. 1.

[28] K Lam and S Banerjee. “On the condition of streak formation in a bounded turbulent flow”. In: *Physics of Fluids A: Fluid Dynamics* 4.2 (1992), pp. 306–320.

[29] Kang-Kun Lee and Darrell I Leap. "Application of boundary-fitted coordinate transformations to groundwater flow modeling". In: *Transport in porous media* 17.2 (1994), pp. 145–169.

[30] Mei-Ying Lin et al. "Direct numerical simulation of wind-wave generation processes". In: *Journal of Fluid Mechanics* 616 (2008), pp. 1–30.

[31] Song Liu et al. "Investigation of coupled air-water turbulent boundary layers using direct numerical simulations". In: *Physics of Fluids* 21.6 (2009), p. 062108.

[32] Paolo Lombardi, Valerio De Angelis, and Sanjoy Banerjee. "Direct numerical simulation of near-interface turbulence in coupled gas-liquid flow". In: *Physics of Fluids* 8.6 (1996), pp. 1643–1665.

[33] Imperial College London. "Streaks in Turbulence". In: 2014. URL: https://www.imperial.ac.uk/aeronautics/fluiddynamics/ChernyshenkoResearch/TwoParadigmsForStreaks.php#:~:text=Streaks.

[34] C Lorencez et al. "Liquid turbulence structure at a sheared and wavy gas-liquid interface". In: *International journal of multiphase flow* 23.2 (1997), pp. 205–226.

[35] Kurt O Lund and William B Bush. "Asymptotic analysis of plane turbulent Couette-Poiseuille flows". In: *Journal of Fluid Mechanics* 96.1 (1980), pp. 81–104.

[36] N Nd Mansour, John Kim, and Parviz Moin. "Reynolds-stress and dissipation-rate budgets in a turbulent channel flow". In: *Journal of Fluid Mechanics* 194 (1988), pp. 15–44.

[37] SM Mitran. "Adaptive Mesh Refinement Computation of Turbulent Flows–Pitfalls and Escapes". In: *Numerical Modeling of Space Plasma Flows: ASTRONUM-2008*. Vol. 406. 2009, p. 249.

[38] Parviz Moin and Krishnan Mahesh. "Direct numerical simulation: a tool in turbulence research". In: *Annual review of fluid mechanics* 30.1 (1998), pp. 539–578.

[39] Evgeny V Mortikov, Andrey V Glazunov, and Vasily N Lykosov. "Numerical study of plane Couette flow: turbulence statistics and the structure of pressure–strain correlations". In: *Russian Journal of Numerical Analysis and Mathematical Modelling* 34.2 (2019), pp. 119–132.

[40] Robert D Moser, John Kim, and Nagi N Mansour. "Direct numerical simulation of turbulent channel flow up to Re τ= 590". In: *Physics of fluids* 11.4 (1999), pp. 943–945.

[41] Frans TM Nieuwstadt, Jerry Westerweel, and Bendiks J Boersma. *Turbulence: introduction to theory and applications of turbulent flows*. Springer, 2016.

[42] "OpenFOAM". In: URL: http://https://www.openfoam.com/.

[43] Stephen B Pope and Stephen B Pope. *Turbulent flows*. Cambridge university press, 2000.

[44] Stéphane Popinet. "Gerris: a tree-based adaptive solver for the incompressible Euler equations in complex geometries". In: *Journal of computational physics* 190.2 (2003), pp. 572–600.

7

[45] James J Riley, Ralph W Metcalfe, and Michael A Weissman. "Direct numerical simulations of homogeneous turbulence in density-stratified fluids". In: *AIP Conference Proceedings*. Vol. 76. 1. American Institute of Physics. 1981, pp. 79–112.

[46] JJ Riley et al. "DNS of homogeneous turbulence in density-stratified fluids". In: *Proc. of AIP Conference on Nonlinear Properties of Internal Waves, New York*. 1981, pp. 79–112.

[47] Wolfgang Rodi. "Examples of calculation methods for flow and mixing in stratified fluids". In: *Journal of Geophysical Research: Oceans* 92.C5 (1987), pp. 5305–5328.

[48] Paulo AB de Sampaio, José LH Faccini, and Jian Su. "Modelling of stratified gas–liquid two-phase flow in horizontal circular pipes". In: *International Journal of Heat and Mass Transfer* 51.11-12 (2008), pp. 2752–2761.

[49] Hermann Schlichting and Klaus Gersten. *Boundary-layer theory*. Springer, 2016.

[50] Kaustav Sengupta, Farzad Mashayek, and Gustaaf Jacobs. "Direct numerical simulation of turbulent flows using spectral method". In: *46th AIAA Aerospace Sciences Meeting and Exhibit*. 2008, p. 1450.

[51] Lian Shen et al. "The surface layer for free-surface turbulent flows". In: *Journal of Fluid Mechanics* 386 (1999), pp. 167–212.

[52] R.Shankar Subramaniam. *Boundary Conditions in Fluid Mechanics*. https://web2.clarkson.edu/projects/subramanian/ch560/notes/Boundary%20Conditions%20in%20Fluid%20Mechanics.pdf. n.d.

[53] HS Tang et al. "Fluid driven by tangential velocity and shear stress: Mathematical analysis, numerical experiment, and implication to surface flow". In: *Mathematical Problems in Engineering* 2013 (2013).

[54] Hendrik Tennekes and John L Lumley. *A first course in turbulence*. MIT press, 2018.

[55] Pierre Trontin et al. "Detailed comparisons of front-capturing methods for turbulent two-phase flow simulations". In: *International journal for numerical methods in fluids* 56.8 (2008), pp. 1543–1549.

[56] Takahiro Tsukahara, Hiroshi Kawamura, and Kenji Shingai. "DNS of turbulent Couette flow with emphasis on the large-scale structure in the core region". In: *Journal of Turbulence* 7 (2006), N19.

[57] Henk Kaarle Versteeg and Weeratunge Malalasekera. *An introduction to computational fluid dynamics: the finite volume method*. Pearson education, 2007.

[58] Stéphane Vincent and Jean-Luc Estivalezes. "Direct numerical simulation of turbulent two-phase flows: application to liquid sheet atomization". In: *Proceedings of CHT-15. 6 th International Symposium on ADVANCES IN COMPUTATIONAL HEAT TRANSFER*. Begel House Inc. 2015.

[59] Pieter Wesseling. *Principles of computational fluid dynamics*. Vol. 29. Springer Science & Business Media, 2009.

[60] Wikipedia. "Direct Numerical Simulation". In: 2020. URL: https://en.wikipedia.org/wiki/Direct_numerical_simulation.

[61] George Yadigaroglu and Geoffrey F Hewitt. *Introduction to multiphase flow: basic concepts, applications and modelling*. Springer, 2017.

[62] Yoshinobu Yamamoto and Tomoaki Kunugi. “Direct numerical simulation of a high-Froude-number turbulent open-channel flow”. In: *Physics of Fluids* 23.12 (2011), p. 125108.

[63] S Yoon and D Kwak. “Implicit methods for the Navier-Stokes equations”. In: *Computing Systems in Engineering* 1.2-4 (1990), pp. 535–547.

[64] Francesco Zonta, Alfredo Soldati, and Miguel Onorato. “Growth and spectra of gravity-capillary waves in countercurrent air/water turbulent flow”. In: *Journal of Fluid Mechanics* 777 (2015), p. 245.